Development of microRNA Triggered Therapeutic Oligonucleotides and Gold Nanoparticle Conjugates to Improve Specificity of RNA Therapeutics

A Dissertation
Presented to
The Academic Faculty

by

Jiahui Zhang

In Partial Fulfillment
of the Requirements for the Degree
Doctor of Philosophy in the
Wallace H. Coulter Department of Biomedical Engineering

Georgia Institute of Technology and Emory University
December 2020

Development of microRNA Triggered Therapeutic Oligonucleotides and Gold Nanoparticle Conjugates to Improve Specificity of RNA Therapeutics

Approved by:

Dr. Khalid Salaita, Advisor
Department of Biomedical Engineering
Emory University

Dr. Hanjoong Jo, Advisor
Department of Biomedical Engineering
Emory University

Dr. Gabe Kwong
Department of Biomedical Engineering
Georgia Institute of Technology

Dr. Krishnendu Roy
Department of Biomedical Engineering
Georgia Institute of Technology

Dr. Younan Xia
Department of Biomedical Engineering
Georgia Institute of Technology

Dr. Cherry Wongtrakool
Department of Medicine
Emory University

Date Approved: Oct. 14th, 2020

ACKNOWLEDGEMENTS

Foremost, I would like to express my deepest appreciation to my advisors Dr. Hanjoong Jo and Dr. Khalid Salaita for their continuous guidance and support for my Ph.D. study and research. Their profound belief in my ability provides me with motivation to be consistently persistent in tackling difficulties in my research. I would also like to thank them for their support and suggestions to help me conquer hardships in my life besides research.

I would like to extend my sincere thanks to the rest of my committee members, Dr. Krishnendu Roy, Dr. Gabe Kwong, Dr. Cherry Wongtrakool, and Dr. Younan Xia, for their insightful advice in my research and help throughout my journey during the pursuit of my degree.

I wish to thank all my labmates and collaborators, who I had great pleasure of working with. They offered tremendous help with my experiments, as well as treasurable friendship and emotional support.

Lastly, I would like to thank my families and friends. I would like to thank my parents for their unconditional care and belief. I am also extremely grateful to my friends in Georgia Tech and Emory University, who provide a good support system for me to survive and thrive in grad school.

TABLE OF CONTENTS

LIST OF TABLES

LIST OF FIGURES

LIST OF SYMBOLS AND ABBREVIATIONS

ABCA	Adenosine triphosphate-binding cassette transporter
AGO	Argonaute
ASO	Antisense oligonucleotide
DNAzyme	Deoxyribozyme
FLIM	Fluorescence lifetime imaging
gRNA	Guide RNA
HIF1α	Hypoxia-inducible factor 1 α
LNA	Locked nucleic acid
LNP	Lipid nanoparticle
miRNA	microRNA
NAT	Nucleic acid therapeutics
ORF	Open reading frame
PS	Phosphorothioate
RISC	RNA-induced silencing complex
SET	Surface energy transfer
siRNA	Small interference RNA
SNA	Spherical nucleic acid
SSO	Splicing-switching oligonucleotide
TCSTC	Time Correlated Single Photon Counting
TLR	Toll-like receptor
TNFα	Tumor necrosis factor α
UTR	Untranslated region

SUMMARY

RNA-targeting oligonucleotide therapeutics and their nanoparticle conjugates hold great promise in treating intractable diseases, but their clinical applications are still limited by significant barriers including the lack of tissue or cell type specificity. Current strategy to improve tissue or cell type specificity of oligonucleotides therapeutics mainly involves conjugation with ligands. However, this strategy encounters bottleneck in diseased conditions where a specific surface marker is absent. In addition to protein markers, transcriptomic techniques have revealed complex and diverse alterations of coding and non-coding transcripts in different tissues, cell types or disease conditions, which opens up opportunities to control the activity of oligonucleotide therapeutics utilizing these endogenous transcripts to improve their specificity. The overall hypothesis of the dissertation is that using specific transcripts as triggering stimulus, oligonucleotides and their nanoparticle conjugates can be activated via toehold-mediated strand displacement reaction to conditionally regulate gene expression. As a proof-of-concept, we chose miRNA as the transcript trigger, hoping to provide a foundation for future design of smart therapeutics sensing more complicated transcript inputs. In this dissertation, we demonstrated the idea of miRNA-inducible conditional gene regulation agents with two models: (1) miR-33 triggered activation of DNAzyme-gold nanoparticle (AuNP) conjugates to down regulate tumor necrosis factor α (TNFα) in pro-inflammatory macrophages; and (2) miR-122-indicible antisense to down regulate hypoxia inducible factor 1α (HIF1α) in liver cells. In addition, to gain insights on the intracellular fate of oligonucleotide-AuNP conjugates for better design of conditional gene regulatory agents,

we leveraged a powerful imaging modality, fluorescence lifetime imaging (FLIM), to monitor the intracellular integrity of oligonucleotide-AuNP conjugates. Programmable therapeutics with controllability of location, timing and intensity of their activity can lead to precise medicine with minimal side effects. We envision that the design principles for conditional oligonucleotides and their AuNP conjugates discovered from this dissertation could be adopted to a variety of translatable clinical applications and improve the controllability and safety of oligonucleotide therapeutics and nanoparticle conjugates.

CHAPTER 1. INTRODUCTION

1.1 Opportunities and challenges for RNA therapeutics

The majority of human diseases are directly related to deregulation or mutation of proteins caused by transcriptional and translational misregulation or mutations in the genome. Conventional therapeutics to target these disease-related proteins are small-molecule chemical compounds or large-molecule proteins, such as antibodies. However, the majority of disease-related proteins are currently "un-drugged", with only less than 700 human proteins therapeutically targeted by FDA-approved small molecule and biologic drugs, which is encoded by only 0.05% of human genome (Figure 1.1) [1, 2]. In addition to directly targeting these disease-related proteins by conventional therapeutics, gene replacement therapy and genome editing technology aim to fix the disease-related proteins at its source by either delivering new genetic materials (DNA) into cells to replace or compensate abnormal genes and make functional proteins, or editing the genetic defect or mutation to correct the protein product. However, the long-term safety regarding permanently inserting engineered genetic materials, and/or possible off-target editing in the genome still require careful evaluation.

For a long time, the potential of targeting the intermediate between the genome and proteins, that is mRNA transcripts, has been relatively neglected, as well as non-coding RNAs that compose ~70% of human genome but do not translate into proteins. In the past two decades, more classes and functions of non-coding RNA have been discovered, many of which has been found to regulate or influence disease-related proteins and become

validated therapeutic targets. [3, 4] In the meantime, the therapeutic potential of directly targeting RNA, including mRNA and non-coding RNA, have gradually emerged. The therapeutic molecules that target RNA transcripts are termed as "RNA therapeutics". RNA therapeutics can either mimic or antagonize endogenous RNAs, and thus indirectly act on downstream disease-related proteins, including those that are conventionally "undruggable". Therefore, RNA therapeutics hold great promise to address the unmet medical needs by functioning on their own or by being combined with existing therapeutics. In addition, RNA therapeutics are highly predictable, easy to design, and less costly, allowing short development time and large-scale production. Hence, RNA therapeutics has attracted substantial amount of interest from both academia and pharmaceutical industries and have become the third class of high-impact medicines alongside small molecules and antibodies. Despite these advantages, the clinical application of RNA therapeutics must overcome of their poor pharmacological properties, including susceptibility to nucleases and difficulty in delivery to the target tissues.

In Section 1.1.1, categories and mechanism of RNA therapeutics, as well as their current status in clinical applications will be reviewed. In Section 1.1.2, the challenges that RNA therapeutics are facing, and advancement in solving these challenges will be discussed.

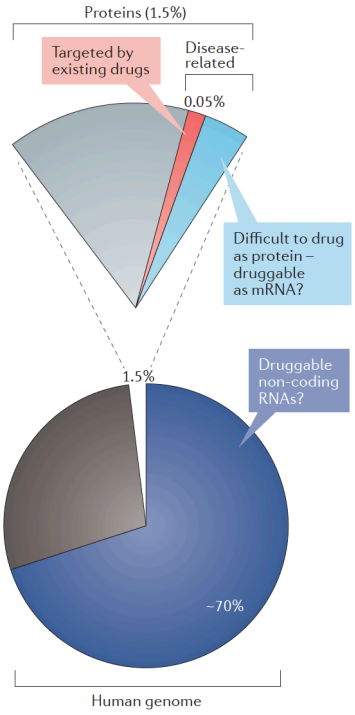

Figure 1.1 The potential RNA-targeted druggable genome. [2]

1.1.1 Categories of RNA therapeutics, their mechanisms of action and current status in clinical applications

The world of RNA therapeutics includes RNA-targeting small molecules, mRNA therapeutics, antisense oligonucleotides (ASOs), splicing-switching oligonucleotides (SSOs), RNA interference therapeutics (siRNA), deoxyribozymes (DNAzymes), and microRNA (miRNA) therapeutics. These RNA therapeutics have diverse mechanisms of actions on the target RNA, including modulating RNA stability, abundance, splicing, and protein binding. In section 1.1.1, each category of RNA therapeutics and their mechanism of action is described, and their current status in clinical application is summarized.

1.1.1.1 RNA-targeting small molecules

Unlike the typical helix structure adopted by double-stranded DNA, single-stranded RNA can fold itself into diverse structures to minimize its energy. These structures provide unique binding pockets for selective recognition by small molecules.

The most successful RNA-targeting small molecules are antibiotics binding to ribosomal RNA, resulting in perturbation of protein synthesis. Because ribosomal RNA is highly abundant in the cells, small molecules targeting the ribosome only require modest binding affinity. [5, 6] Small molecules could also be used to treat viral infection through binding specifically to viral RNA structures required for replication, such as inhibiting trans-activator of transcription (Tat)-trans-activating response element (TAR) interaction, which is required for HIV replication. [7]

One category of disease-related human RNA that can be targeted by small molecules is mRNAs with nucleotide repeat expansions. Diseases such as Fragile X Syndrome, myotonic dystrophy, and Huntington's disease can result from expanded nucleotide repeats located in different regions of transcripts. [8] For example, in the case of myotonic dystrophy, expanded nucleotide repeats in the 3' untranslated region (UTR) of the dystrophia myotonica protein kinase (*DMPK*) (type 1) [9] or intron 1 of zinc finger 9 protein (*ZNF9*) transcript (type 2) [10] fold into hairpins displaying regularly repeating internal loops that bind to the splicing regulator, muscleblind-like 1 protein (MBNL1), with high affinity, resulting in its sequestration and thus dysregulation of alternative splicing of various pre-mRNAs [11]. Small molecule compounds that displace the MBNL1 from the

expanded repeats and restore its function have been identified via screening and show partial rescue of mis-splicing in a mice model. [12] It has also been shown by Disney and co-workers that assembly of expanded repeats-targeting compounds into dimers or trimers with appropriate spacing could enhance their binding affinity and selectivity. [13]

Another class of disease-related RNA that provide ideal binding sites of small molecules is miRNA precursors. Pri-miRNAs possess Drosha and Dicer processing sites, which allow their processing into pre-miRNAs and further mature miRNAs. As an example, compound Targapremir-210 selectively inhibits oncogenic miR-210 biogenesis by binding to the C/C internal loop displayed in its Dicer processing site. [14]

1.1.1.2 mRNA therapeutics

mRNA therapeutics encoding beneficial proteins have become an attractive gene therapy strategy, because they are safer than plasmid DNA and viral vectors due to transient production of proteins and less chance of containing foreign genes and bacterial components. [15]

mRNA therapeutics are synthesized via *in vitro* transcription (IVT) from a linearized plasmid or a PCR template that contains a bacteriophage promoter, a 5'-UTR, an open reading frame (ORF), a 3'-UTR and optionally a poly(A) sequence. 5' end cap is incorporated to the mRNA by either co-transcriptional capping during IVT or enzymatic capping post IVT (Figure 1.2). [15] One subtype of mRNA therapeutics is self-amplifying mRNAs, which additionally encode a viral replicase and enable self-amplification of RNAs

encoding the protein-of-interest in the cytoplasm. [16] IVT mRNA therapeutics often utilize modified nucleosides for mitigating immune activation and optimized codon usage to improve translational efficiency. [17]

So far, there are no approved mRNA therapeutics. mRNA therapeutics in clinical trials are applied to cancer immunotherapy, infectious diseases vaccines and protein replacement therapy. [18] mRNA therapeutics encoding tumor antigens are used as cancer immunotherapy by transfection into immune cells, mostly dendritic cells, *ex vivo* and re-administration into patients or *in situ*. [19] mRNAs encoding viral antigens are used to treat infectious diseases, including influenza, cytomegalovirus, Zika, and SARS-Cov-2. [20, 21] mRNAs as protein replacement therapy usually encode therapeutic antibodies and functional proteins, such as cystic fibrosis transmembrane conductance regulator (CFTR) for treating cystic fibrosis and vascular endothelial growth factor A (VEGFA) for treating diabetes and heart failure. [22, 23]

Other promising directions of mRNA therapy undergoing preclinical investigation includes modulating induced pluripotent stem cells (iPSCs) differentiation by encoding cell reprogramming factors [24] and gene-editing by encoding zinc-finger nucleases (ZFNs), transcription activator like effector nuclease (TALENs), and CRISPR/Cas endonucleases [25]. For cancer vaccine applications, in addition to dendritic cells, other immune cells are recently transfected to generate cancer vaccines, such as T cells and NK cells transfected with mRNAs encoding chimeric antigen receptor (CAR). [26, 27]

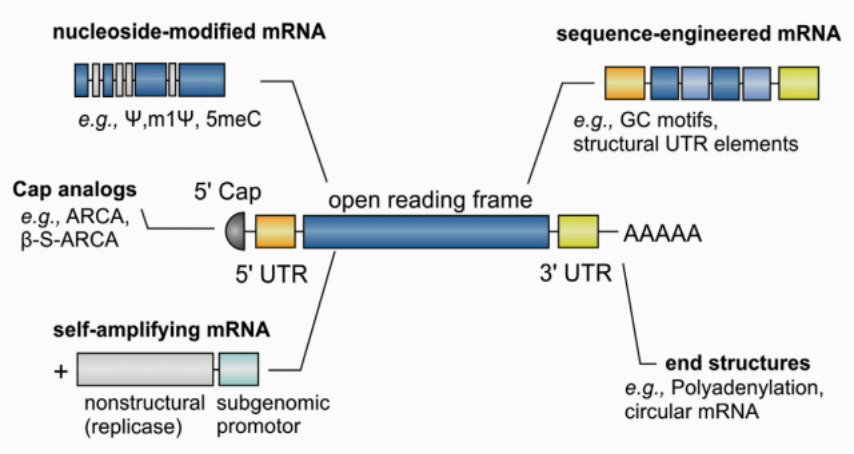

Figure 1.2 Structure of IVT mRNA. [28]

1.1.1.3 Antisense Oligonucleotides (ASOs)

ASOs can be divided into two categories based on their mechanisms of action: RNase H competent ASOs and steric blocking ASOs.

RNase H competent ASOs are short single-stranded synthetic DNAs (16-20 nt) that selectively bind via complementary base-pairing to mRNA and modulate mRNA expression by recruiting ribonuclease H (RNase H) to cleave the mRNA upon binding (Figure 1.3a). The first generation of ASOs are with phosphorothioate (PS) modified backbone, such as the first FDA-approved ASO in 1998, Fomivirsen, to treat cytomegalovirus (CMV) retinitis [29], which was later withdrawn due to low potency. To improve potency, second generation of ASOs were developed, which consist of PS backbone and several modified nucleotides at each terminus to protect the ASO from exonuclease and enhance overall binding kinetics. This design is termed as "gapmer", with the central gap sequence allowing cleavage of target mRNA by RNase H. One example of

a gapmer is the second FDA-approved ASO in 2013, Mipomersen, for treating hypercholesterolemia. [30] To date, two other ASOs have been approved to treat human diseases, which are Inotersen (2018) to reduce transthyretin for the treatment of hereditary transthyretin amyloidosis polyneuropathy (hTAAR) [31], and Volanesorsen (2019) to reduce apolipoprotein C-III and further triglycerides for the treatment of familial chylomicronemia syndrome and familial partial lipodystrophy [32]. All three approved second generation ASOs are 2'-O-methyoxyethyl (2'-MOE) and PS modified gapmers.

Steric blocking ASOs are designed to bind to mRNA with high affinity and inhibit translation of mRNA by steric blocking of the translational machinery (Figure 1.3b). [33] Recent studies also showed that ASOs can be designed to upregulate protein expression by binding to and sterically inhibiting the 5'-UTR regulatory elements [34] or upstream open reading frames (uOPF) [35], which selectively increase the protein translated from a downstream primary ORF (pORF) (Figure 1.3c). These findings could potentially broaden the utility of ASO for modulating protein expression.

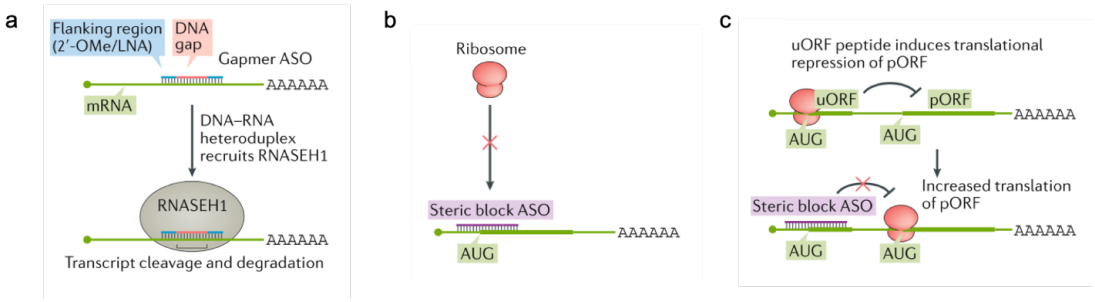

Figure 1.3 Mechanism of ASOs. (Adapted from [36])

1.1.1.4 Splicing-Switching Oligonucleotides (SSOs)

In addition to ASOs that modulate mRNA stability and translation, oligonucleotides can also bind to pre-mRNA and modulate its splicing. These oligonucleotides are called splicing-switching oligonucleotides (SSOs), which block essential sequences for splicing and prevent the interaction of splicing factors with the pre-mRNA (Figure 1.4). [37] Chemical modifications that are compatible with SSOs include alternating locked nucleic acids (LNAs), fully modified 2'-substitution and phosphorodiamidate morpholino oligomers (PMO). [38]

One example of SSO targeted disease is Duchenne Muscular Dystrophy (DMD), which is caused by deletions that disrupt the translational reading frame and abrogating expression of the dystrophin protein that is essential for maintaining muscle fibers integration. SSOs that induce out-of-frame exon restores the reading frame and result in truncated dystrophin that is partially active. [38-40] Other indications that SSOs could address include spinal muscular atrophy (SMA) [41], β-thalassemia [42] and rheumatoid arthritis [43].

To date, there are three SSOs approved for treating human diseases, including Eteplisen (2016) [44], Golodirsen (2019) [45] for treating DMD, and Nusinersen (2016) for treating SMA [46]. In an exceptional case, an SSO called Milasen, was designed and approved for the treatment of a single patient, Mila, with Batten's disease, by targeting a unique mutation of MFSD8 gene in her genome. [47] Milasen was injected into the patient within 10 months after the mutation was identified. This example provides a strong proof

for the rapid development time of oligonucleotide therapeutics and the potential of SSOs as personalized medicine to address diseases caused by rare and unique mutations.

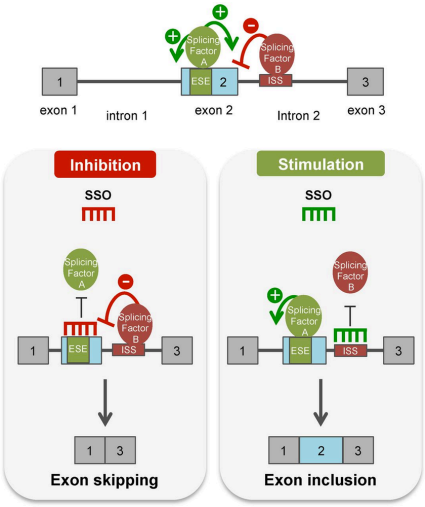

Figure 1.4 Mechanism of SSOs. [37]

1.1.1.5 siRNA

Small interfering RNAs (siRNAs) are double-stranded RNAs (dsRNAs) that induce RNA interference (RNAi) in cells. Synthetic siRNAs are generally base-paired dsRNA or short hairpin RNAs (shRNAs) as precursors. The length of siRNA is around ~21 bp, with a failure to engage RNAi machinery shorter than 15 bp and nonspecific toxicity longer than 30 bp. [48] siRNA precursors, including longer dsRNAs (>21bp) and shRNAs, are cleaved by Dicer and then loaded into RNA-induced silencing complex (RISC). Shorter siRNAs enter the RISC directly without Dicer processing. siRNA is comprised of the guide strand (antisense strand) and the passenger strand (sense strand). The bias in guide strand selection

is achieved by the asymmetric structure of siRNA. Usually, guide strand selection is biased to the strand with a 2 nt 3' overhang or chemical modified 3' blunted end. The strand with weaker base pairing at its 5' terminus will be preferentially selected for incorporation into RISC. [49] Once loaded into RISC, the guide strand binds to the target mRNA to initiate cleavage by Argonaute (Ago2) (Figure 1.5). [50]

Synthetic siRNAs are chemically modified. Chemical modification improves potency of siRNA by enhancing resistance to endogenous endonucleases and exonucleases, and improves safety by reducing endogenous immune response to unmodified dsRNA. In addition, chemical modification can also enhance guide strand selectivity, and improve sequence selectivity. Fully modified dsRNAs with 2'-O-methyl and 2'-F modifications and PS backbone were found to reduce immune activation and improve serum stability. [51]

To date, two siRNA has been approved by FDA: Patisiran (2018) for treating hTAAR [52], and Givosiran (2019) for treating acute hepatic porphyria [53].

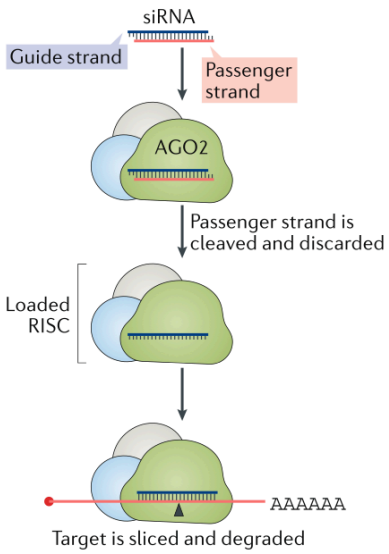

Figure 1.5 Mechanism of siRNA mediated cleavage of mRNA. [36]

1.1.1.6 Deoxyribozymes (DNAzymes)

DNAzymes are catalytic oligonucleotides that bind to and cleave RNAs in a sequence specific manner. DNAzymes are obtained through *in vitro* selection using a method called selection of ligands by exponential enrichment (SELEX). [54] A most widely used RNA-cleaving DNAzyme is named the 10-23 DNAzyme, because it was identified from clone 23 after ten rounds of amplification. The 10-23 DNAzyme is composed of a 15 nt catalytic core and two recognition arms, which can selectively bind to and degrade target mRNA. [54] It hydrolyzes RNA between an unpaired purine and paired pyrimidine (Figure 1.6). Intracellular activity of DNAzymes could possibly be the results of both catalytic cleavage activity and antisense effect mediated by RNase H. [55]

DNAzyme activity relies on di-cation cofactors, such as Mg^{2+}, Ca^{2+} and Mn^{2+}. DNAzymes are more sensitive to mismatches than antisense possibly because of the destabilization caused by the catalytic core.

Thus far, three DNAzymes have been undergoing clinical trials: Dz1 targeting oncovirus Epstein-Barr virus (EBV)-encoded latent membrane protein 1 (LMP1) to treat nasopharyngeal carcinomas caused by EBV [56]; Dz13 targeting c-jun mRNA for treating basal carcinoma by blocking angiogenesis [57]; and hgd40 targeting GATA-3 for treating allergic bronchial asthma [58].

Chemical modifications are compatible to the binding arms and terminus of the DNAzymes. For example, Dz13 and hgd40 have inverted thymidine residue at their 3'-end, and Dz1 was modified by only two phosphorothioate linkage at both termini. The catalytic core of Dz has been found to be tolerant of certain modifications at specific positions. [59-61]

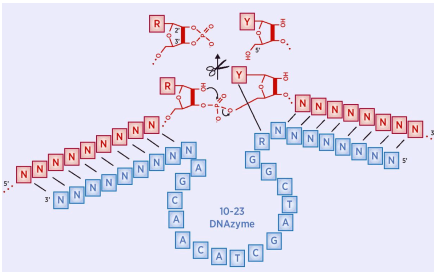

Figure 1.6 Structure and sequence of 10-23 DNAzyme. [62]

1.1.1.7 microRNA therapeutics

Endogenous microRNAs (miRNAs) are a class of non-coding RNAs that regulate mRNA degradation or translation by binding to their target sites on the 3'-UTR of mRNA. Because miRNA levels are often dysregulated in disease conditions and regulate disease-related proteins, they are considered as important and useful targets for therapeutics. [63] miRNA therapeutics consist of miRNA mimics, anti-miRNAs and block-miRs.

miRNA mimics are synthetic oligonucleotides that mimics endogenous miRNA. They are often perfect base-paired, chemically modified siRNAs, whose guide strand has the same sequence as endogenous miRNA. [64, 65] Anti-miRNAs, or antogomirs, are chemically modified single strand ASOs for endogenous miRNAs, which is complementary to the miRNA (Figure 1.7). [66, 67] Target site blockers, or block-miRs, are ASOs that bind to the miRNA binding site on the 3'-UTR of a specific mRNA with perfect complementarity (Figure 1.7). [68]

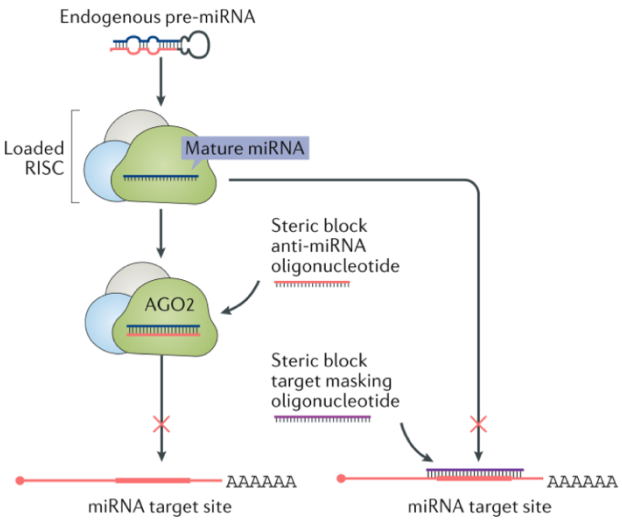

Figure 1.7 Mechanism of anti-miRNA and block-miR. [36]

1.1.2 Challenges of RNA therapeutics and potential solutions

Despite the tremendous potential of RNA therapeutics, early attempts to use unmodified or minimally modified oligonucleotides without conjugates or delivery vehicles show limited efficacy. Obstacles that oligonucleotides must overcome include susceptibility to nucleases, immunogenicity, limited cell entry and lack of tissue or cell type specificity, which render poor pharmacokinetics. In Section 1.1.2, advances in chemical modification and delivery materials to improve oligonucleotide pharmacokinetics are summarized and discussed.

1.1.2.1 Chemical modifications of oligonucleotides

Unmodified oligonucleotides have limited stability and undergo rapid degradation mediated by nucleases. They also have poor pharmacokinetic properties, as they are excreted rapidly through renal clearance after administration. [69] In addition, unmodified siRNAs induce innate immune responses and cause toxicity through Toll-like receptor (TLRs) dependent and independent mechanisms. [70-72] Thus, chemical modification is necessary for oligonucleotides for clinical utility.

There are several positions on an oligonucleotide that are amenable for chemical modifications, including base modification, sugar modification, backbone modification and terminal conjugation, shown in Figure 1.8. In this section, examples of commonly used chemical modifications and their effect on oligonucleotide properties are described.

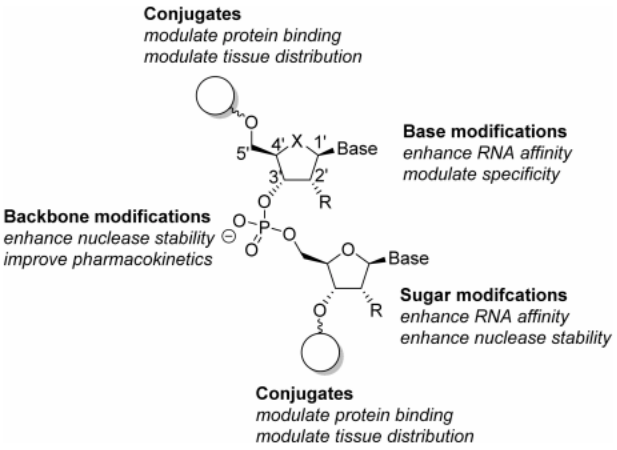

Figure 1.8 Sites for modification on a dinucleotide subunit. [73]

1.2.1.1.1. Nucleobase modification

Nucleobase modifications can affect the binding affinity and/or specificity to target mRNA, but is not commonly used. One naturally occurring nucleobase modification that is used in synthetic oligonucleotides is C-5 methyl modification on cytosine (Figure 1.9) to mitigate immunostimulation of CpG. It also enhances the thermal stability of oligonucleotide duplex by 0.5 °C per incorporation. [73]

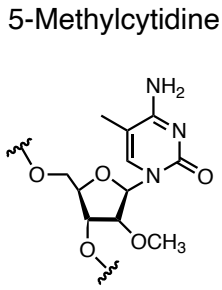

Figure 1.9 Structure of 5-Methylcytidine.

1.2.1.1.2. Backbone modification

The phosphodiester backbone of oligonucleotides is rapidly hydrolyzed by nucleases, therefore, alternative backbones with enhanced stability have been developed. One of the earliest and most widely used backbone modification is PS modification, which is the replacement of a nonbridging oxygen atom of the phosphodiester (PO) linkage with sulfur. PS modification greatly enhance stability of oligonucleotides and PS-modified oligonucleotides can be synthesized using similar conditions as the PO oligonucleotides. PS modifications reduce affinity for complementary nucleic acid by ~0.5 °C per incorporation. [74] PS modifications can increase nonspecific binding of oligonucleotides

to proteins [75, 76], which facilitates their uptake into cells [77] and prevents rapid renal excretion but can also result in increased toxicity [78, 79]. PS modifications introduce a chiral center; therefore, a PS-modified oligonucleotide is composed of a series of stereoisomers (Figure 1.10).

Other commonly used backbone modifications are mopholino and peptide nucleic acid (PNA) (Figure 1.10). These modifications are extremely resistant to nucleases, but they do not support RNase H activity. Therefore, they are mainly used in steric blocking ASOs or SSOs.

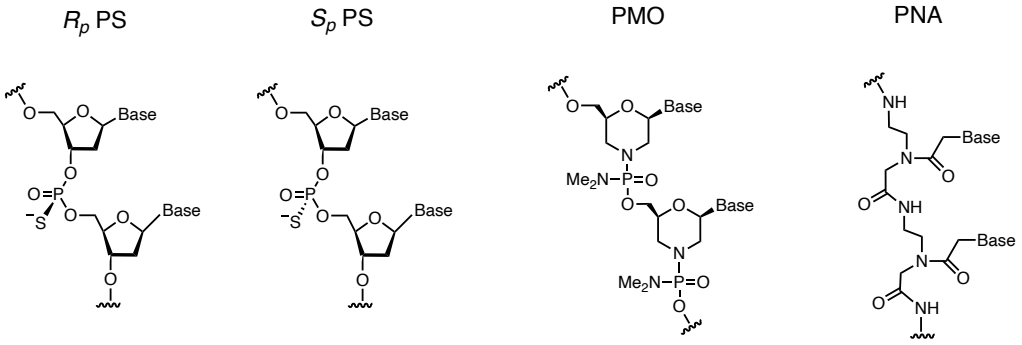

Figure 1.10 Common backbone modifications in oligonucleotide therapeutics.

1.2.1.1.3. Sugar modification

2'-modified RNA represents one of the most widely used sugar modifications. 2'-O-methyl (2'-O-Me), 2'-O-Methxyethyl (2'-O-MOE), and 2'-Fluoro (2'-F) modification (Figure 1.11) have been used in ASO, SSOs, and siRNA, and entered clinical development.

Another class of sugar modification enhances binding affinity by restricting the ribose ring into the C3'-endo sugar pucker by tethering 2'- and 4'-positions, such as locked nucleic acid (LNA) [80], constrained ethyl (cEt) and bridged nucleic acid (BNA) [81] (Figure 1.11). These modifications enhance thermal stability of oligonucleotide to complementary RNA remarkably with ~5 °C per incorporation. [81]

The five-membered sugar ring can also be replaced with six-membered ring, such as hexitol nucleic acid (HNA) (Figure 1.11) to render nuclease resistance [82]. Unlocked nucleic acid (UNA) (Figure 1.11), which is highly flexible due to the lack of the C2'-C3'-bond of the ribose ring, can be used in siRNAs to modulate duplex stability [83] and introduce chemical asymmetry of the duplex and promote RISC loading of the guide strand [84].

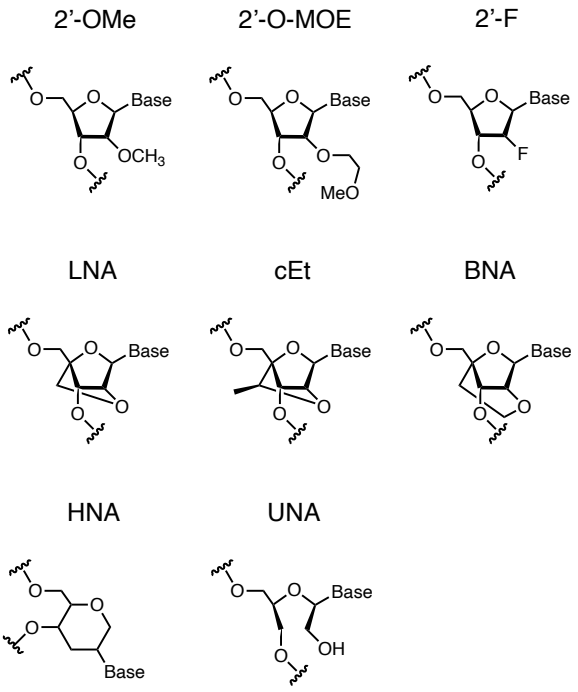

Figure 1.11 Common sugar modifications in oligonucleotide therapeutics.

1.2.1.1.4. Terminal modification

3'-inverted thymidine can be incorporated in oligonucleotide to improve nuclease resistance (Figure 1.12). [85] Lipid conjugation, such as cholesterol (Figure 1.13), enhances oligonucleotide activity by facilitating their cell entry due to increased hydrophobicity. [86] Conjugation of trivalent N-acetyl galactosamine (GalNAc) (Figure 1.13) to siRNA or ASO improve their potency in hepatocytes by targeting the asialoglycoprotein receptor (ASGPR) exclusively on hepatocytes. [87]

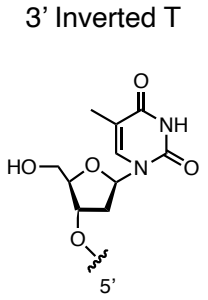

Figure 1.12 Structure of 3'-inverted thymidine.

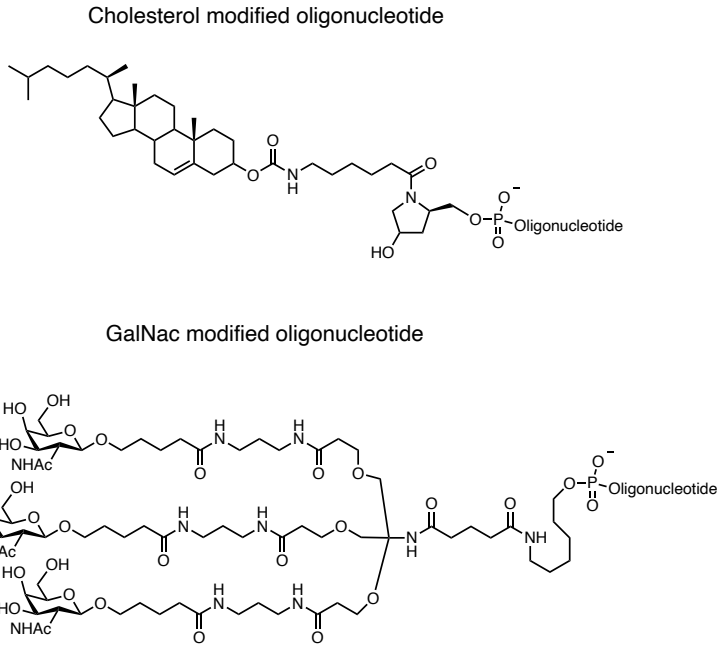

Figure 1.13 Structure of cholesterol- and GalNAc-modified oligonucleotides.

1.1.2.2 Delivery materials of RNA therapeutics

Oligonucleotides are large hydrophilic polyanions, which do not readily pass through the plasma membrane. Therefore, self-transfecting nanomaterials are developed to facilitate delivery of oligonucleotide RNA therapeutics.

Formulation with lipid is the most commonly used approach to enhance nucleic acid delivery. Lipoplex is the complex of cationic lipid and polyanionic oligonucleotides formed through electrostatic interaction. Liposomes comprise a lipid bilayer encapsulating the oligonucleotides (Figure 1.14a). The most widely adopted lipid nanoparticles (LNPs) are liposomes consisting of cationic lipid, phospholipid, cholesterol, and polyethylene glycol (PEG)-lipid conjugated in defined ratios. [88] LNPs associate with apolipoprotein E (ApoE), which facilitates liver uptake via low-density lipoprotein receptor (LDLR)-mediated endocytosis. [89]

Exosomes are another class of delivery vehicle of oligonucleotides (Figure 1.14b). Exosomes are natural extracellular vehicles released by cells and are naturally present in the blood. They are capable of traversing biological membranes, including the blood-brain barrier (BBB) [90], have increased circulation time [91], and can be engineered to display specific surface ligands for targeting purpose [92]. The major challenge of exosomes are the loading efficiency of oligonucleotide cargos and scale-up manufacturing issues.

Spherical nucleic acids consist of a hydrophobic core decorated with hydrophilic oligonucleotides (Figure 1.14c). The core materials can be gold nanoparticles (AuNPs), silica particles or other materials. [93] Although the oligonucleotides are exposed instead of being encapsulated, they are protected to some degree by steric hindrance due to the high loading density. [94] A detailed summary and discussion on spherical nucleic acids, more specifically oligonucleotide-AuNP conjugates are presented in Section 1.2.

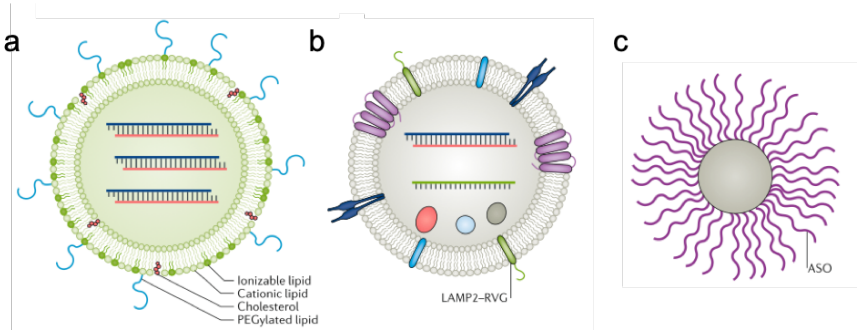

Figure 1.14 Delivery materials of oligonucleotide therapeutics. (a) Lipid nanoparticle, (b) exosome, and (c) spherical nucleic acid. [36]

1.1.2.3 Tissue and cell type specificity

To date, the majority of oligonucleotides are given to patients by local delivery or systemic delivery to the liver. In order to broaden the clinical indications that oligonucleotide therapeutics can address, investigators developed many approaches to improve the tissue or cell type specificity of RNA therapeutics and their delivery vehicles. The most commonly adopted strategy is ligand-receptor interaction-mediated recognition and endocytosis, as discussed in Section 1.2.1.3.1. Two relatively new strategies involve the development of delivery vehicles with inherent tissue tropism and the design of conditional oligonucleotides that are activated by stimulus. The former is summarized in Section 1.2.1.3.2, and the latter is discussed in Section 1.3 respectively.

1.1.2.3.1 Specific cell surface marker-mediated cellular uptake

Targeted delivery systems can improve the efficiency and specificity of oligonucleotide therapeutics. Targeted delivery of oligonucleotides is usually achieved by

two strategies: (1) direct conjugation of oligonucleotides with a ligand; (2) delivery of oligonucleotide with ligand-modified nanocarriers.

A variety of ligands, including small molecules, antibodies, peptides, and aptamers, have been conjugated to oligonucleotides or their nanocarriers for targeted delivery to specific cell types expressing corresponding receptors. [95] The most successful ligand is GalNAc, which binds to ASGPR expressed on hepatocytes (Figure 1.15). [96] Conjugation of GalNAc resulted in 10-fold increase of siRNA potency in hepatocytes. [97] Folate receptor and transferrin receptor are overexpressed in many cancer cells, therefore folate and transferrin have been used as a ligand for tumor targeted delivery of oligonucleotide or nanoparticles. Antibodies and peptide ligands have also been used to direct oligonucleotide delivery. Sugo *et al*. conjugated siRNA with anti-CD71 Fab' fragment to target muscle and heart leveraging the abundancy of CD71 on the surface of skeletal and cardiac myocytes. [98] Zhang *et al*. conjugated the HER2 antibody on SNAs and demonstrated enhanced uptake in HER2 overexpressing cells. [99] Kheirolomoom *et al*. developed liposomes with the VHPK peptide, a ligand for VCAM-1, to deliver anti-miRNA to inflamed endothelial cells to prevent atherosclerosis. [100] Aptamers specific for cell surface markers is another approach for targeted delivery. [101, 102] McNamara *et al*. developed an aptamer-siRNA chimera to inhibit tumor growth, with the aptamer binding to prostate specific membrane antigen (PSMA), a cell-surface receptor overexpressing in prostate cancer cells, and the siRNA targeting survival genes. [103] Rajagopalan *et al*. conjugated 4-1BB-aptamer to siRNA against CD25 to attenuate IL-2 signaling in 4-1BB expressing $CD8^+$ T cells. [104] Wang *et al*. developed nucleolin-

targeted extracellular vesicles to deliver siRNA to breast cancer cells via modifying the extracellular vesicles with aptamer AS1411. [105]

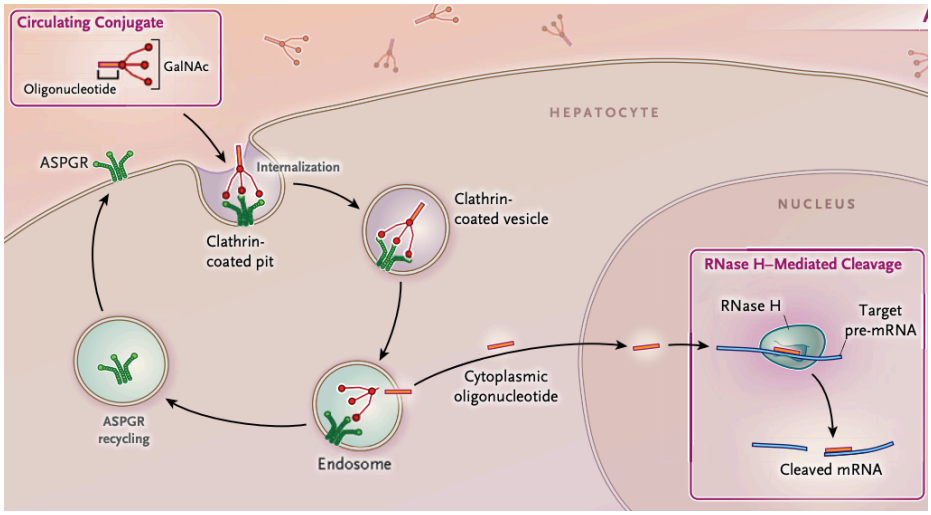

Figure 1.15 ASGPR mediated uptake of GalNAc conjugated oligonucleotide therapeutics. [106]

1.1.2.3.2 Nanomaterials with tissue tropism

In addition to decorating nanomaterials with the targeting ligand, it has been found that certain chemical composition could potentially provide tissue tropism of nanomaterials. As an example, Siegwart *et al*. reported that with an increased molar percentage of a positively charged lipid, 1,2-dioleoyl-3-trimethylammonium-propane (DOTAP), in LNP formulation encapsulating luciferase encoding mRNA, luciferase expression showed a shift of tissue specificity from the liver to the spleen and further to the lung; whereas incorporation of a negatively charged lipid 1,2-dioleoyl-sn-glycero-3-

phosphate (18PA) enabled excusive delivery to the spleen with no luciferase expression in other organs. [107]

A high-throughput method to screen for tissue-specific nanocarriers for nucleic acid therapeutics is to apply a high-throughput DNA barcoding system and measure delivery efficacy of individual nanoparticle formulation in different tissues or cell types after administration of hundreds of nanoparticles with distinct composition in mice. [108-110] Utilizing this approach, nanoparticles targeting endothelial cells [109, 111], T cells [112], and liver Kupffer cells [113] have been discovered.

1.2 Delivery of RNA therapeutics using oligonucleotide-AuNP conjugates

As mentioned in Section 1.1.2.2, SNAs with AuNP core have been used to deliver oligonucleotide RNA therapeutics. SNAs are self-transfecting, resistant to nucleases and capable of high loading density, which allows for wide applications in RNA targeting therapy. In this section, preparation methods (Section 1.2.1) and gene regulation application (Section 1.2.2) of SNAs are summarized, and current understanding of cellular uptake mechanism (Section 1.2.3) and intracellular fate (Section 1.2.4) of SNAs are discussed.

1.2.1 Preparation methods of oligonucleotide-AuNP conjugates

The most commonly used method for preparation of AuNPs is solution-phase reduction of chloroauric acid to form citrate-capped AuNPs with a diameter from 5 to 150 nm. [114, 115] AuNPs with larger size can be prepared by reduction of ionic gold onto the surface of a gold nanoparticle seed. [116]

To construct oligonucleotide-AuNP conjugates, thiolated oligonucleotides displace citrate ions from the gold surface and make a stable gold-thiol linkage. Sodium chloride is added to the solution to screen the negatively charged phosphate backbone of the oligonucleotides, which leads to more closely packed oligonucleotides, resulting in increased density of the oligonucleotide on the gold surface. [117] This method requires gradual salting of the mixture over many hours to avoid aggregation of AuNPs. To construct dsDNA nanoparticles, the ssDNA nanoparticles after purification by centrifugation are incubated with excess complementary oligonucleotide (~10 fold) at 65 ºC followed by immediate refrigeration at 4 ºC to allow hybridization. [118]

A more time-effective approach to construct oligonucleotide-AuNP conjugates reported recently utilizes freezing and thawing of thiolated oligonucleotide and AuNPs. [119, 120] The freezing method provides higher density of oligonucleotides on each NP compared to the salt-aging method and can also be used to conjugate double stranded DNA by simply freezing the thiolated strand, its complementary strand and AuNPs together, and adding salt before thawing. The mechanism for the freezing method is the enhanced conjugation kinetics due to high local concentration of AuNPs, DNA and salt caused by the repulsion as the water crystallizes. Besides the freezing method, adjusting the mixture of AuNPs and thiolated DNA to pH 3.0 in citrate buffer could also enable rapid attachment of DNA on AuNPs. [121]

Recently, a salt-aging free and thiol-free method based on the intrinsic affinity of poly(A) for AuNPs was also reported. [122] In this study, a linker of 10 adenine (A) bases was shown to be sufficient for the freezing-mediated attachment of oligonucleotides to AuNPs for sequences that does not form secondary structures, and addition of extra A bases for sequences with blocked A based by secondary structures improved the attachment.

1.2.2 Oligonucleotide-AuNP conjugates for gene regulation

Oligonucleotide-AuNP conjugates provide easy cellular uptake and nuclease resistance of the oligonucleotide therapeutics, thus are capable of acting as gene regulation agents. In 2006, Rosi *et al*. reported that phosphorothioate modified ASO-AuNPs knocked down EGFP in C166, a mouse endothelial cell line. [123] In 2009, Giljohann *et al*. reported siRNA-AuNP conjugates, which knocked down luciferase expression for over 4 days in HeLa cells. [124] In 2013, Jensen *et al*. reported that siRNA-AuNP conjugates targeting oncoprotein Bcl2Like12 (Bcl2L12) overexpressed in glioblastoma multiform (GBM) were able to penetrate the blood-brain barrier and blood-tumor barrier to knock down Bcl2L12 and reduce tumor burden in U87MG-derived xenogeneic mice after intravenous injection of the NPs. [125] In 2015, reported by Randeria *et al*., topical delivery of siRNA-AuNPs targeting ganglioside-monosialic acid 3 synthase (GM3S), a mediator of impaired wound healing, in type 2 diabetic mice reduced GM3S expression at the wound edge and accelerated wound healing. [126]

Besides ASO and siRNA, DNAzymes were also conjugated on AuNPs for gene regulation purposes. In 2012, Yehl *et al*. reported that DzNPs down-regulated transforming

growth factor β (TGFβ) related growth differentiation factor 15 (GDF15) in HCC1954 cells after 48h incubation period. [94] In 2016, Somasuntharam *et al*. reported that local injection of TNFα DzNPs in the rat myocardium following myocardial infarction resulted in anti-inflammatory effects and improvement in acute cardiac function. [127]

1.2.3 Cellular uptake of oligonucleotide-AuNP conjugates

Oligonucleotide-AuNP conjugates readily enter a wide variety of cell types without any transfection agents, despite its high negative charge. However, the amount of AuNPs internalized differs by cell type and may vary by as much as a factor of 20. The uptake of NPs depends on their initial concentration *in vitro*, which is linearly proportionate at low concentrations and reaches saturation at high concentrations. The density of oligonucleotides on AuNPs plays a significant role in their cellular uptake, as studied with AuNPs tethered to a varied density of oligonucleotides using oligoethylene glycol (OEG) as a diluent. [128]

To determine the pathway of endocytosis of SNAs, Choi *et al*. [129] examined how inhibiting specific pathways of endocytosis affects their cellular uptake. A minor reduction of uptake was observed in C166 cells treated with chlorpromazine, a pharmacological inhibitor that disrupts the formation of clathrin-coated pits, and in clathrin deficient C166 cells, which excludes clathrin-mediated endocytosis. Treatment of C166 cells with methyl-β-cyclodextrin and filipin, which removes or sequesters cholesterol, significantly reduced the cellular uptake of SNAs. Furthermore, caveolin-1 deficient C166 cells exhibited reduction in endocytosis of SNAs. Therefore, the authors concluded that caveolae mediated

the endocytosis of SNAs. Pretreatment with fucoidan and polyinosinic acid, ligands of scavenger receptors, resulted in reduction of SNA uptake. [130] Using ELISA assay, class A scavenger receptor (SR-A) was demonstrated to show high affinity toward SNAs. SR-A deficient C166 cells showed ~80% decrease of SNA uptake. In addition, the uptake of SNAs correlate positively with the expression level of SR-A and caveolin-1 in different cell types. [129] Together, these studies indicated an endocytosis model, where SNAs bind to cell surface SR-A, and enter cells via the caveolae-mediated pathway. It is also reported by Narayan *et al*. that SNAs containing high G content showed the highest cellular uptake, because linear poly G is a natural ligand for SR-A presumably due to G-quadruplex formation. [131]

1.2.4 Intracellular fate of oligonucleotide-AuNP conjugates

A colocalization study done by Wu *et al*. [132] showed that SNAs traffic through the endocytic pathway into the late endosome and reside in the late endosomes 24 h after incubation. By replacing the AuNP core with a fluorescent quantum dot (QD), they observed a separation of the fluorescence signals from QD and fluorophore-labeled on oligonucleotides, indicating disassembly of the SNAs, which is likely due to degradation of DNA by DNase II.

Although oligonucleotide-AuNP conjugates have been show to effectively down regulate their target gene, their mechanism as in whether the conjugates work as a single entity or just a delivery vehicle is not well understood. A recent study published by Yamankurt *et al*. [133] showed that siRNA attached on the AuNP surface can be cleaved

by Dicer and released to enter the canonical RNAi pathway. Therefore, they designed siRNA-AuNP conjugates with both passenger strand and guide strand attached to the AuNP, in order to achieve higher loading density of siRNA.

1.3 Smart nucleic acids therapeutics to enhance specificity

As everyone knows, the primary role of nucleic acids *in vivo* is to encode and transduce genetic information. Interestingly, nucleic acids are also promising therapeutics that can modulate the expression of specific genes, and offer an alternate class of drugs to small molecules and protein-based therapeutics. Due to their functional versatility, NATs can be designed to target each level of the central dogma. At the genome level, guide RNA (gRNA) in CRISPR-Cas systems and triplex forming nucleic acids mediate genome editing. At the transcript level, messenger RNA (mRNA) and oligonucleotide RNA therapeutics (eg. antisense oligonucleotide (ASO), siRNA, miRNA, anti-miRNA, DNAzyme, and splicing-switching oligonucleotides) modulate stability, abundance or splicing of transcripts. At the protein level, aptamers, DNA decoys or immune-stimulating oligonucleotides inhibit or stimulate protein activities. In addition, DNA nanostructures have also been developed as vehicles to deliver therapeutic payloads [134].

The discovery and development process of NATs is simple, fast and cost effective due to high predictability of nucleic acid binding and structure. Over the past two decades, advances in chemical modification of the phosphodiester backbone, nucleobases and the ribose sugars [51] along with innovations in delivery formulations such as lipid nanoparticles [135] have resulted in NATs with high potency, low immunogenicity and

easy cell entry. Together this has led to tremendous progress toward clinical translation. Indeed, over the past 7 years, six ASOs and three siRNAs were approved by the FDA to address unmet medical needs by treating diseases lacking adequate treatment options, such as spinal muscular atrophy [41] and familial hypercholesterolemia [30]. Another clinical application of NATs pertains to the rapid development of vaccines. For example, Pfizer (https://clinicaltrials.gov/ct2/show/NCT04368728) and Moderna (https://clinicaltrials.gov/ct2/show/NCT04283461) are leading efforts using *in vitro* transcribed (IVT) mRNA to generate vaccines for SARS-CoV-2, the virus responsible for the Covid-19 pandemic [21, 136]. The advantage of IVT mRNA is that it bears no risk of insertional mutagenesis in contrast to plasmid-borne mRNA therapeutics. Another exciting frontier for NATs is in genome editing, and early stage clinical trials of CRISPR-Cas9 editing are showing evidence of safety and efficacy for *ex vivo* editing [137], with the first *in vivo* trial for treating Leber ongenital amaurosis by EDIT-101 [138] just launched.

Despite the milestones that NATs have made toward clinical translation, getting the therapeutics into the right cell type within the right tissue has been considered as a major roadblock for NATs to treat a wider range of clinical indications. Thus far, most NATs that have been approved or that are under clinical testing are either directed to the liver by systemic delivery leveraging passive accumulation (lipid nanoparticles (LNPs) encapsulated siRNA, such as Patisiran) [139] or ligand-mediated accumulation (GalNAc-siRNA, such as Givosiran) [140], or delivered locally (intrathecal injection for Nusinersen, subretinal injection for EDIT-101). The development of innovative delivery technologies that enable efficient targeting of additional tissues and cell types is highly desirable and is

the subject of multiple investigations that are nascent or in the preclinical front, such as LNPs that enable lung-targeted delivery [109].

An alternate strategy to enhance the specificity of NATs is through incorporating on/off switches in NATs, aiming to activate or deactivate NATs with specific exogenous or endogenous triggers. Creating these smart NATs involves combining programmable modalities within functional NATs. The triggers molecules are the "input"; the programmable modalities are signal "transducers"; and the output NAT functions are the "effector" (Figure 1.16a). Smart NATs can be categorized based on the source of the input, the transducer and the function of the effector (Figure 1.16b).

Section 1.3 focuses on recent progress in controlling NAT activity to achieve precise and specific therapeutics. We classify smart NATs broadly based on the mode of action of the transducer (programmable modality), including photochemical reactions, ribodevices, strand hybridization and displacement reactions, and protein-ligand binding.

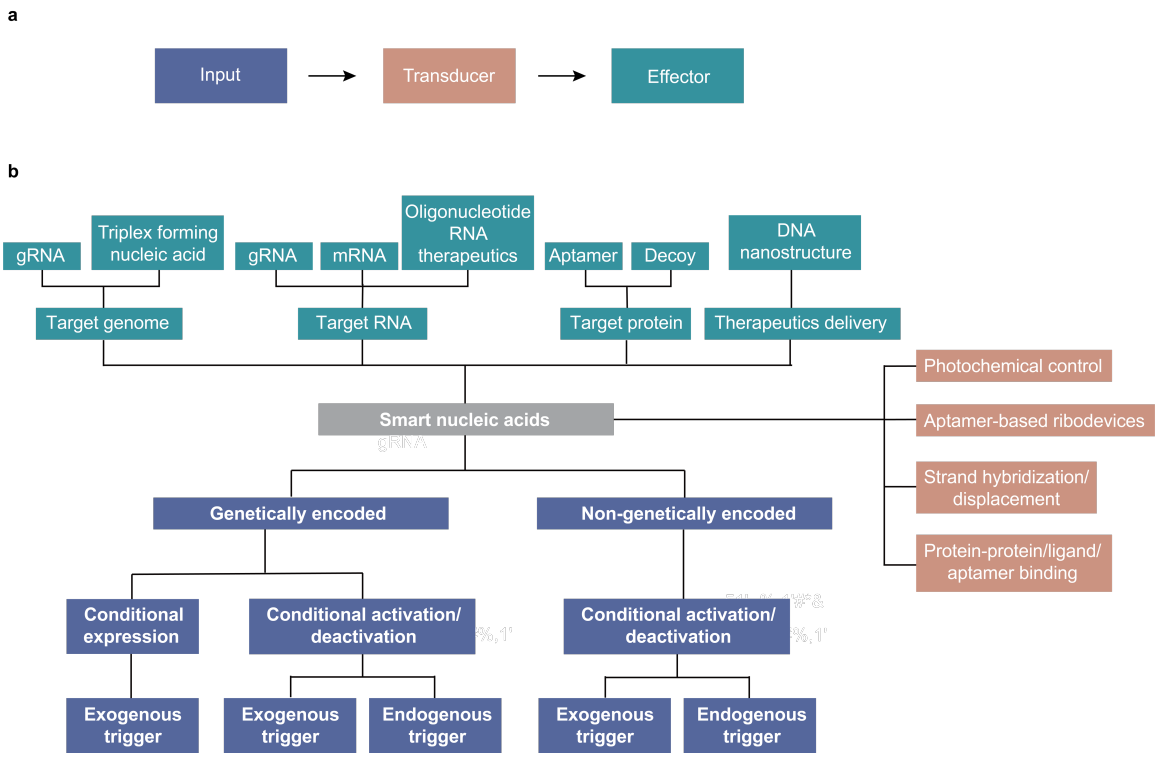

Figure 1.16 Schematic showing the general components and different types of smart nucleic acid therapeutics (NATs).
(a) Smart NATs are made of three main components: the trigger molecule is the "input" (blue); the "transducer" is typically a programmable conformational or structural change (brown); the output function is the "effector" (turquoise). (b) Smart NATs can be categorized based on the source of the input (genetically encoded, non-genetically encoded), the transducer (photochemical control, ribodevices, hybridization/strand displacement, protein-protein/ligand/aptamer binding) and the function of the effector (genome editing, RNA regulation, protein binding, therapeutics delivery).

1.3.1 Photochemical control provides spatiotemporal precision

As a bio-orthogonal trigger, light-induced regulation of NAT activity represents a very precise means of achieving high-resolution control in both a spatial and temporal fashion. Typically, photochemical control of oligonucleotide therapeutics activity is achieved through the introduction of photo-caged nucleobases or photolabile linkers.

Activation or deactivation of ASOs [141-143], anti-miRNA [144], DNAzymes [142, 145], transcription factor DNA decoys [146, 147], triplex forming oligonucleotides [148] and gRNAs [149, 150] by light irradiation in mammalian cells or living model organisms have been achieved via incorporating photo-caged nucleobases or photolabile linkers on either the NATs themselves or their blocker sequences. As an example, Liu *et al*. developed a gRNA caged on the protospacer adjacent motif (PAM)-distal region, which is required for Cas9-mediated cleavage. This gRNA can bind to its target DNA but cannot induce cleave until light stimulation [151]. Another mechanism of light-activated NATs utilizes photochemical (λ=350 nm) depurination of nucleobase mimics, which removes the purine bases and inhibits their binding function. For example, Struntz *et al*. demonstrated the release of NF-κB transcription factor from its DNA decoy after light-induced depurination. [152] These methods rely on cleavage of chemical bonds and are hence irreversible. Reversible photo-regulation of oligonucleotide function typically involves isomerization of a molecular photoswitch, such as azobenzene. Azobenzene can be incorporated in oligonucleotides by insertion into the phosphate backbone as a linker or by tethering on the oligonucleotides as a pendant group. Utilizing azobenzene as a linker, UV light irradiation induces distortion of the phosphate backbone, and can deactivate siRNA. [153] Another application of azobenzene backbone linkers is to control binding to complementary RNA. For example, Wu *et al*. introduced azobenzenes between ASOs and flanking inhibitory oligonucleotides to create light-activated ASOs. [154] Kamiya and colleagues used a similar strategy to generate an inducible DNAzyme by linking a complementary sequence with azobenzene to its catalytic core. [155] When azobenzene is tethered as a pendant group, UV irradiation stabilizes the *cis* conformation, which is nonplanar and causes steric

hindrance and thus dissociation of a duplex. Leveraging this strategy, photo-regulation of RNA cleavage rate of DNAzymes [156] and ASOs [157] was controlled by alternatively applying UV and visible light.

Utilizing photolabile linkers, light sensitive DNA nanostructures were also designed, including a hollow nanocuboid for light-triggered release of cargo protein [158], and an origami sphere that can transform into two tethered hemispheres by light irradiation [159]. Triggered by UV or visible light irradiation, hybridization and dehybridization of two oligonucleotides with azobenezene linkers enables a bipyramidal DNA nanocapsule to open and close reversibly. [160, 161]

Controlling mRNA translation by light can be achieved by a combination of light-triggered uncaging or isomerization of small molecule ligands with riboregulatory devices in the untranslated region of the mRNA, which is called a photo-riboswitch. Examples include aptazymes that are activated to self-cleave by binding to uncaged ligands (eg. guanine, GlcN6P) [162, 163], and a riboswitch that selectively binds to the *trans* isoform of an amino stiff-stilbene [164]. Beside photo-riboswitches, a recent study reported a unique method for photoregulation of mRNA translation mediated by light-triggered protein-protein interaction. In this work, mRNA is tagged with MS2-binding sites, which allows labeling with CRY2 and crosslinking of mRNAs with CIB1-fused multimeric proteins in a blue light-specific manner, resulting in translation repression of the mRNA due to inaccessibility of ribosome binding. [165] Although this platform is not suitable for controlling mRNA therapeutics due to temporary translation inhibition and complexity in engineering fused proteins, it provides a new direction of deactivating and activating translation of mRNA by its clustering and disassembly.

Photochemical control provides spatiotemporal precision, but tissue penetration of light is a major hurdle for activation of NATs in deep tissues. To solve this issue, different groups have worked on designing BODIPY [166] or cyanine [167, 168] derivative linkers or two photon-sensitive linkers [147, 169] that can be cleaved by visible or near infrared light to push the penetration limit.

1.3.2 Aptamer-based ribodevices enable small molecule- or protein-triggered activation

Riboswitches are naturally occurring RNA motifs, which incorporate an aptamer as well as a gene regulation domain. When the aptamer binds its small molecule or protein target, this leads to a conformational switch in the RNA that then triggers or inhibits gene expression kinetically or thermodynamically. Riboswitch are most commonly found in bacteria. The riboswitch concept has generated a number of technologies for gene regulation. This is typically achieved by engineering RNA aptamer-based ribodevices, including riboswitches and aptazymes, into the non-coding regions of mRNA in order to control its splicing, translation and degradation [170]. The most common examples of this approach involve inserting a riboswitch into the 5'-UTR, which undergoes a ligand-binding induced structural change that exposures a blocked ribosome binding site (RBS) (Figure 1.17a). Hence, ligand-aptamer binding enables modulation of translation. Another class of engineered ribodevices involves allosteric self-cleaving ribozymes imbedded within mRNA. Here, ligand-binding triggers self-cleavage of the mRNA and translation repression [171, 172] (Figure 1.17b). More comprehensive discussion of natural and engineered ribodevices can be found in other review articles [173-175].

mRNA stability and translation are also naturally controlled by the expression of miRNA which binds the 3'-UTR of target mRNA, causing translation repression. [176] Ribodevices can be used to tune gene expression by interfering with miRNA functions. For example, Farzan and colleagues created a riboswitch engineered in the 3'-UTR of an mRNA to conceal the miRNA target sequence upon ligand binding and thus rescue protein expression (Figure 1.17c). [177] To the best of our knowledge, these ribodevice-controlled gene regulation systems have only been introduced into mammalian cells using plasmids or viral vectors, and they have yet to be delivered using IVT mRNA. We anticipate that the next generation of *in vivo* ribodevices will be delivered using mRNA akin to the advent of mRNA vaccines and protein replacement therapies.

Riboswitches and aptazymes have also been engineered into gRNAs in its 5' or 3' end to create conditional CRISPR endonuclease activity. Consider, for example, an extended gRNA with an aptamer at its 3' end (Figure 1.17d). [178] In the absence of the ligand molecule, the spacer region of the gRNA is paired with its complementary sequence in the 3' extension of the gRNA and cannot bind to its target DNA; however, when a ligand binds to the aptamer it induces a conformational change that allows the spacer region to interact with the corresponding DNA sequence. By extending gRNA with a variety of aptamers that recognize small molecules (eg. tetracycline, theophylline) or proteins (eg. bacteriophage coat protein MS2, human immunodeficiency virus type 1 Rev protein, Ets-1, NF-κB, β-catenin, p53), deactivation or activation of the transcription of gene of interests in response to these triggers was achieved by co-expression of dCas9 or dCas9-VP64 in mammalian cells. [178] This signal conductor design was further applied to redirect the oncogenic signaling to the antioncogenic pathway. [178] Small molecule-

triggered restoration of gRNA activity was also achieved by inserting an aptazyme that contains a theophylline or guanine-binding aptamer between the spacer region and a 5'-extended blocking sequence, which transduces the presence of a small molecule into ribozyme self-cleavage. The addition of ligands triggers self-cleavage of the aptazyme and removal of the blocking sequence from the gRNA, thus enabling genome editing, base editing and transcription activation (Figure 1.17e). [179] Self-cleavage and degradation of gRNA with an aptazyme inserted in a different region (eg. the stem-loop region) of the gRNA backbone was also designed and implemented by Chen *et al*. [180]

In addition to mRNA and gRNAs, ribodevices have also been integrated into siRNA or miRNA precursors to enable small molecule-triggered/inhibited RNA interference. As an example, incorporating of theophylline aptamer in the loop region or basal segment of a short hairpin RNA (shRNA) (Figure 1.17f) or a pri-miRNA led to dose-dependent inhibition of RNAi by theophylline due to inhibited cleavage by Dicer or Drosha. [181, 182] In another example, a pri-miRNA analogue was extended with a theophylline aptazyme and an inhibition strand that hybridized to the 5' end of the pri-miRNA analogue, and thus preventing its processing by Drosha. Addition of theophylline results in self-cleavage and the generation of a proper Drosha substrate, which can then be processed sequentially by Drosha and Dicer to generate mature siRNA (Figure 1.17g). [183] A good example of using these ribodevices in biomedical application was recently published by Lee *et al*., where the ribozyme detects HCV nonstructural protein 5B (NS5B) and responds by activating the anti-miR-122 function in liver cells, thus providing a triggerable therapeutic for HCV infection. [184]

Riboswitches can also be incorporated in dynamic DNA nanostructures for small molecule-triggered cargo release. For example, Banerjee *et al*. reported an icosahedral nanostructure stabilized with a structure-switching cyclic-di-GMP (cdGMP) aptamer. Upon exposure to cdGMP, the aptamer was remodeled, resulting in the dissociation of the icosahedron and the release of encapsulated cargo. [185]

While ribodevices responding to several ligands have been constructed, extension of this platform to diverse inputs, especially disease-related molecules for autonomous therapy, is still a challenge. This is because of the limited number of ligands recognized by riboswitches with high affinity and specificity within a physiological concentration range and with necessary RNA conformational switching. To apply ribodevices for smart NATs with translational capability, new synthetic riboswitches that respond to endogenous disease markers need to be generated. This is typically time consuming and can be accomplished using Capture-Systematic Evolution of Ligands by Exponential Enrichment (Capture-SELEX) followed by intracellular screening. [186]

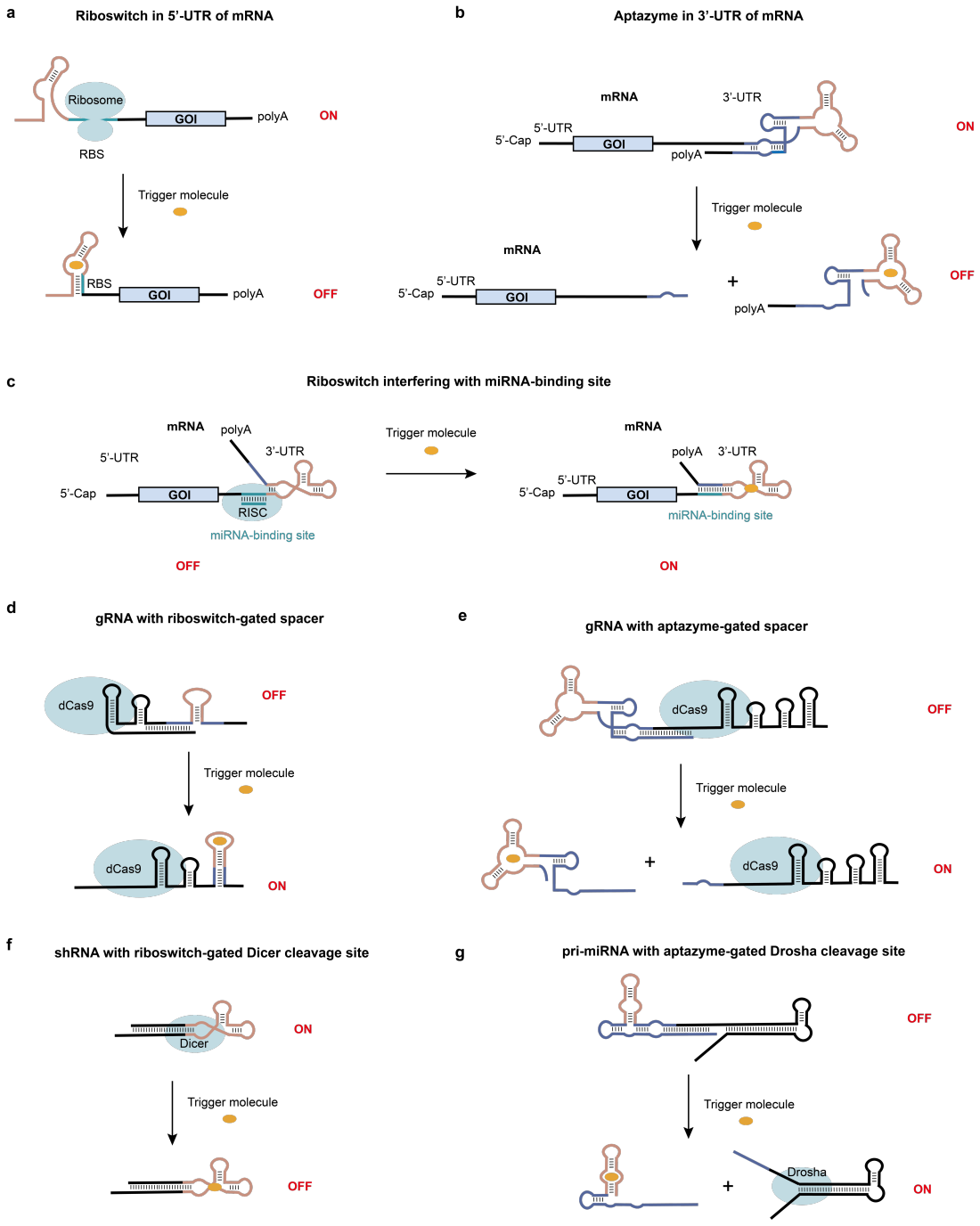

Figure 1.17 Ribodevices enable small molecule- or protein-triggered activation or deactivation of mRNA (a-c), gRNA (d, e), and siRNA or miRNA (f, g).
(a) A riboswitch on the 5'-UTR of mRNA blocks the RBS and represses gene expression upon trigger molecule binding. (b) An aptazyme on the 3'-UTR of the mRNA self-cleaves and causes degradation of the mRNA upon trigger molecule binding. (c) A riboswitch on the 3'-UTR of mRNA conceals a miRNA-binding site upon trigger molecule binding, hence stabilizing the mRNA and switching on gene expression. (d) A gRNA designed with its spacer region hybridized to an extended sequence containing a riboswitch keeps the

Cas9 in an inactive state until the trigger molecule induces a conformational change of the aptamer and the exposure of the spacer domain. (e) A gRNA designed with 5' extension containing an aptazyme and a complementary sequence of the spacer region. Ligand binding induces self-cleavage and removal of the extension and thus exposes the spacer region. (f) A shRNA with its loop domain replaced by a riboswitch. Ligand binding triggers structural change of the aptamer and thus blocks the Dicer binding site and inhibits processing of the shRNA into siRNA. (g) A pri-miRNA is extended with an aptazyme, which blocks the Drosha cleavage site. Upon ligand binding, the aptazyme is cleaved and removed, leading to Drosha processing of the pri-miRNA.

1.3.3 Hybridization and strand displacement enable transcript/synthetic oligonucleotide responsivity

1.3.3.1 Hybridization/strand displacement only

Hybridization to occlude an essential region of a NAT by RNA or DNA is an effective strategy for abrogating its activity. Two good examples of this strategy are anti-miRNA and REVERSIR [187]. Furthermore, loop-mediated hybridization and the toehold-mediated displacement reaction [188] provide two possibilities to unblock nucleic acids, exposing the essential region for target binding and thus recovering activity.

Inspired by innate input/output response of riboswitches, the field has engineered an array of riboregulatory devices that respond to cognate RNAs [189-192] to control translation of mRNA. For example, in an engineered riboregulator developed by Isaacs *et al.*, the RBS of mRNA was concealed by a *cis*-repressing complementary sequence directly upstream of the RBS, which forms a stem-loop structure that interferes with ribosome binding. A small activating RNA unfolds the stem-loop by hybridizing to the loop and the complementary sequence, exposing the RBS and permitting translation (Figure 1.18a) [193]. An improvement to this design was demonstrated by Green *et al.*, where the RBS domain was encoded into the hairpin loop of the toehold switch. Thus the trigger can

employ virtually any sequence and is not limited to incorporating the RBS sequence itself (Figure 1.18b). [194] The use of toehold-mediated displacement reactions, as opposed to loop-mediated hybridization, enables stronger thermodynamics and improved kinetics, resulting in a wider dynamic range for the response function. Because the toehold switch design can accept trigger RNAs with arbitrary sequences, these elements can be activated by endogenous RNAs for autonomous control of gene expression. Toehold switches controlled by endogenous miRNA was demonstrated in mammalian cells by Wang *et al*. [195], indicating the potential application of this strategy in autonomous mRNA therapeutics. Furthermore, Kim *et al*. designed an ultrasensitive toehold switch composed of multiple hairpins sensing the same RNA trigger, resulting in an increased apparent Hill coefficient with decreasing hairpin-to-hairpin spacing or increasing hairpin number. [196] In addition to "off-to-on" toehold switches, recently, translational repressors were designed as variations of "on-to-off" toehold switches. For example, toehold repressors that turn off translation through RNA triggered disruption of a hairpin upstream of an exposed RBS were developed recently (Figure 1.18c). [197] Another type of "on-to-off" toehold switch is a three-way junction repressor, in which an unstable hairpin containing the RBS and start codon allows for translation to proceed. However, when a trigger RNA binds the two domains flanking the hairpin, the hairpin becomes sufficiently stable to block translation (Figure 1.18d). [197] These methods provide a convenient approach to control gene expression by using innate expressed RNA inputs. In the subsequent paragraph, we describe more recent approaches that leverage the Cas9 nuclease system to achieve the same goal of controlling gene expression using RNA inputs.

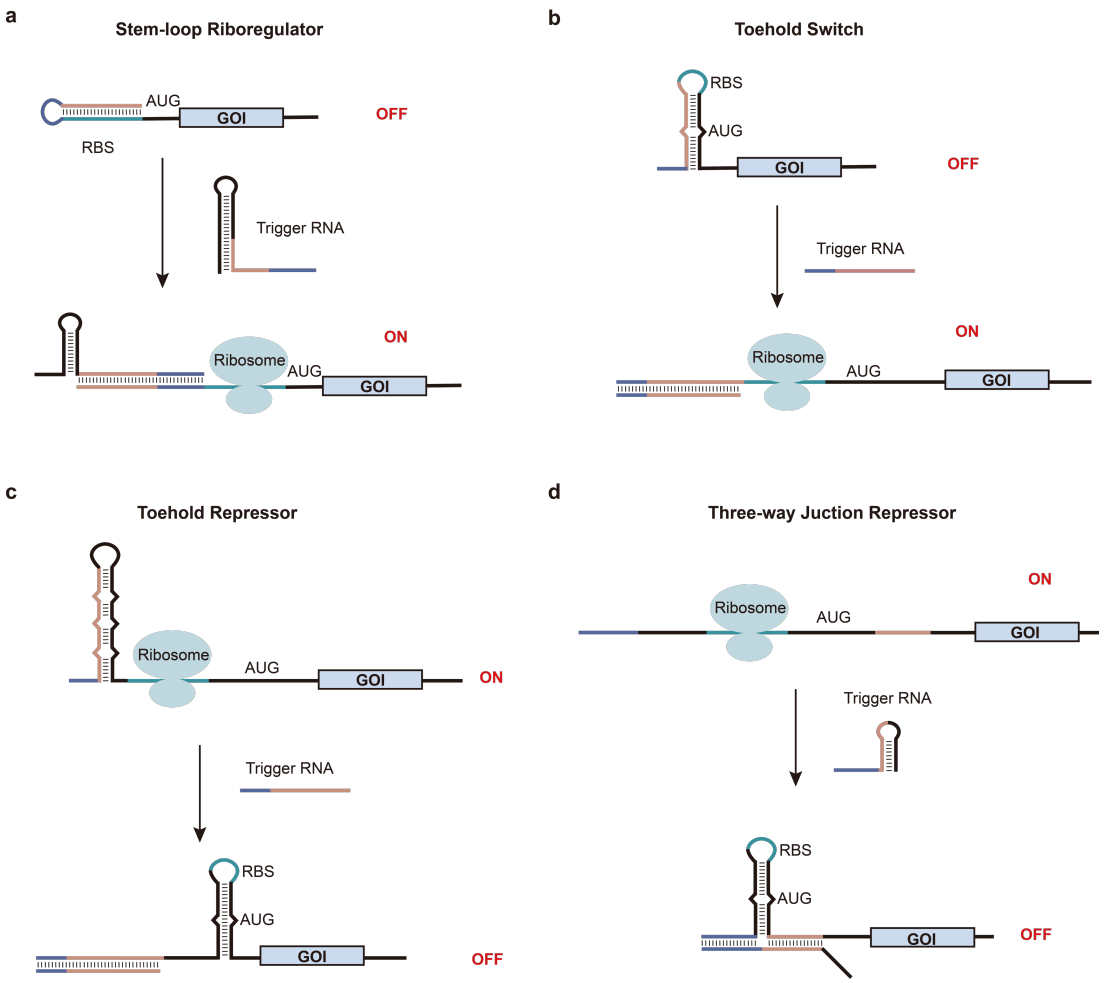

Figure 1.18 Hybridization and strand displacement enable transcript responsivity of mRNA.
(a) A stem-loop riboregulator interferes with ribosome binding and permits translation upon binding the trigger RNA. (b) An engineered toehold switch leverages a toehold-mediated displacement reaction to expose the RBS and trigger translation. (c) A toehold repressor turns off translation upon trigger RNA binding. Here the RNA binds the toehold switch and generates a new stem-loop that blocks the RBS site and inhibits translation. (d) A three-way junction repressor stabilizes an RBS-containing stem-loop in the presence of trigger RNA, and thus switches off translation.

The CRISPR-Cas9 system offers a very potent and effective approach that can leverage hybridization or displacement reactions to control gene expression. Akin to the toehold displacement approaches described above, the gRNA can be deactivated or activated by binding to an input transcript (Figure 1.19 a-c). The general strategy is to tune

the level of repression of gRNA by designing antisense RNAs that conceal different regions of a gRNA. [198] For example, toehold-gated gRNA (thgRNA) is designed with a spacer domain hidden in a hairpin such that Cas9 activity is diminished. Once the thgRNA binds to an RNA trigger strand complementary to the toehold and branch migration domains, it is activated and switch on Cas9 activity (Figure 1.19a). [199] Another approach is to design the gRNA with a 3' extension blocking its scaffold domain which abolishes Cas9 binding; this gRNA recovers its function upon binding a transcript that induces a structural change (Figure 1.19b). [200] One of the few examples employing the more recently discovered Cas12a nuclease rather than Cas9, allows Cas12a binding and activation when the stem-loop of the gRNA is unwound by the trigger RNA. [201] Besides "off-to-on" gRNAs, a terminator switch enables "on-to-off" response in conditional gRNAs by modifying the terminator region of the gRNA. The hybridization of the modified terminator domain to the gRNA triggers a conformational change of the gRNA that inhibits dCas9 function (Figure 1.19c). [202] These above systems were successfully demonstrated in *E. coli* and/or mammalian cells and afford dynamic gRNA tools for potential controlled or specific CRISPR applications. Given the need to better control off-target activity of the Cas9 system, it is likely that more sophisticated trigger mechanisms will be developed in the coming years.

Strand hybridization and displacement reactions can also be incorporated in the design of conditional oligonucleotide therapeutics (siRNA, ASO, shRNA, DNAzymes, etc.) (Figure 1.19d-f). For example, a split DNAzyme was designed for controlled assembly and activation of DNAzyme activity by pulling the split DNAzyme halves together through binding to an input strand (Figure 1.19d). [203] In a recent paper by Zhang

et al., a locked DNAzyme for endogenous miRNA triggered gene regulation was developed (Figure 1.19e) [204]. In this design, the DNAzyme is extended with partial miRNA sequence, and one binding arm of the DNAzyme as well as the extension was sequestered by a lock strand. miRNA triggers dehybridization of the locked DNAzyme through toehold exchange, thus activate the cleavage activity of the DNAzyme to its target mRNA. In addition, inactivation of a triplex forming nucleic acid clamp by toehold-mediated strand displacement reaction was demonstrated by Nguyen *et al*. (Figure 1.19f). [205] A triplex forming nucleic acid clamp binds to the target RNA strand by Hoogsteen base pairing and inhibits ribosomal activity. By extending the clamp with a toehold, it allowed displacement from the target by a releasing strand and thus rescuing mRNA translation activity.

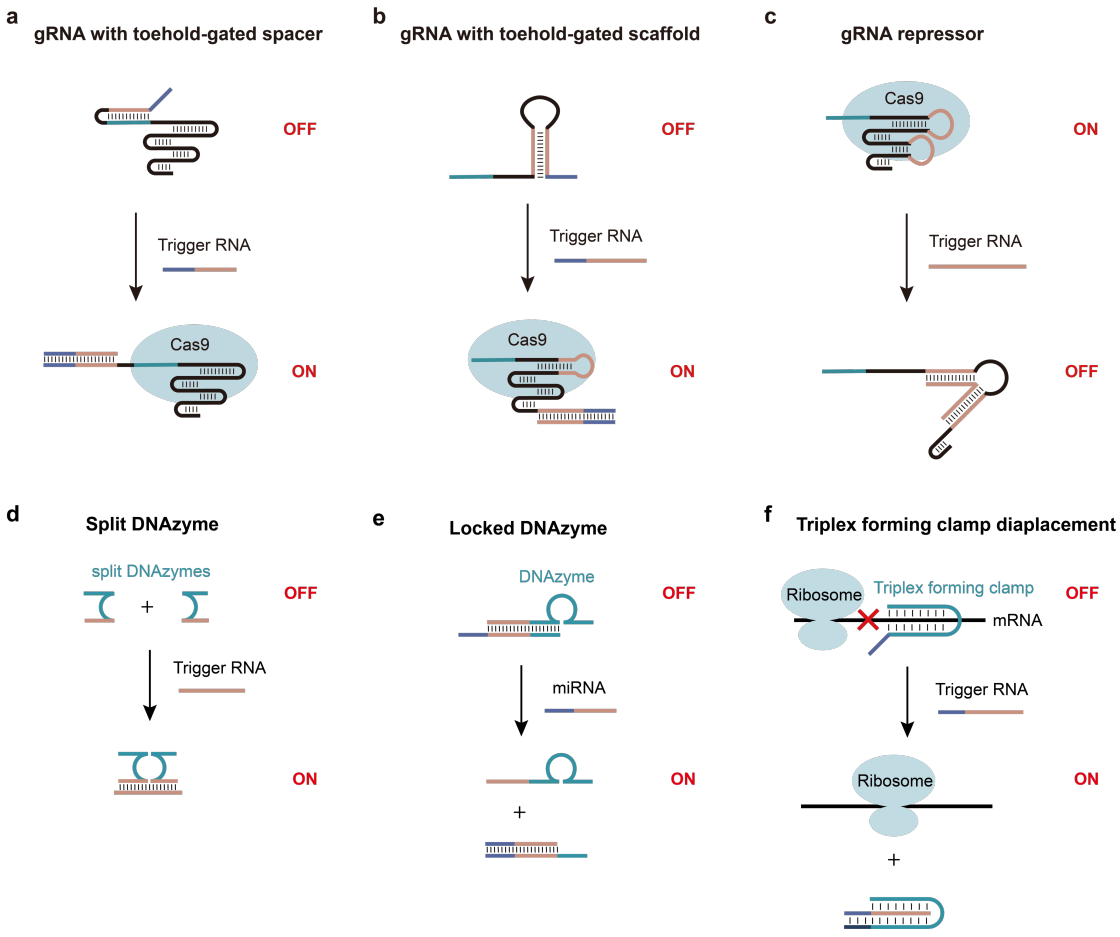

Figure 1.19 Hybridization and strand displacement enable transcript responsivity of gRNA (a-c) and oligonucleotide RNA therapeutics (d-f).
(a) A gRNA with toehold-gated spacer domain is activated by trigger RNA to expose the spacer domain. (b) A gRNA with toehold-gated scaffold domain is activated to enable Cas9 protein binding. (c) A gRNA with modified stem-loop structure alters its shape upon trigger RNA binding to disable Cas9 protein binding. (d) Split DNAzymes are activated upon trigger RNA binding-mediated assembly. (e) A conditional DNAzyme with one binding arm locked is activated by miRNA through toehold exchange. (f) A triplex forming clamp dissociates from the target mRNA as a result of toehold-mediated displacement by trigger RNA.

Dynamic DNA nanostructures for cargo exposure or release were also designed leveraging hybridization or displacement reactions (Figure 1.20). A cylindrical nanorobot with a switchable flap was developed, which opens in response to target hybridization. In

this case, the flap is linked to the chassis of the structure using ssDNA, and once the ssDNA is hybridized it becomes shorter (due to forming the duplex), pulling the flap open (Figure 1.20a). [206] The toehold-mediated strand displacement reaction has been used in multiple examples to achieve DNA triggered release of cargo. For example, the lid of a DNA nanobox was opened with "key" oligonucleotides (Figure 1.20b) [207], and a DNA nanosuitcase that encapsulates siRNA released its cargo upon displacement by the trigger strands [208]. To create a reversible dynamic system, Grossi and colleagues created a DNA vault that opened and closed by the addition of excess opening key and closing key strands (Figure 1.20c). [209] These examples demonstrate the versatility of using toehold displacement reactions to generate input/output functions that control drug release.

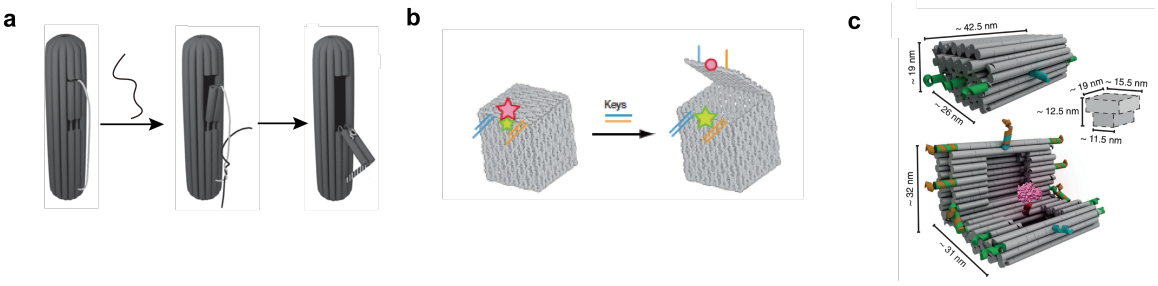

Figure 1.20 Dynamic DNA nanostructures for therapeutics release triggered by hybridization and strand displacement.
(a) A cylindrical nanorobot with a switchable flap is opened upon hybridization of ssDNA thus reducing the length of the linker. [206] (b) A DNA nanobox opens its lid by key oligonucleotides via toehold-mediated displacement with the lock duplex. [207] (c) A DNA vault reversibly opens and closes in the presence of open key and closing key strands. [209]

1.3.3.2 Hybridization and displacement mediated enzyme cleavage

Hybridization and strand displacement can generate enzyme binding sites for NATs, leading to their activation or destabilization. For example, mRNA therapeutics that are controlled by miRNA inputs were created by Jain *et al*. In this case, the mRNA is engineered with miRNA targeting sites in its 3'-UTR, which allows enhanced degradation of the mRNA in cells expressing the specific miRNA (Figure 1.21a). The biomedical implications of this strategy were also demonstrated by expressing a toxic protein in cancer cells while silencing the mRNA in miR-122 expressing liver cells, which enabled more selective destruction of cancer cells with reduced hepatotoxicity. [210] Subsequently, Lee *et al*. leveraged this concept to achieve gene editing in the liver while repressing gene editing in unintended tissues. This was achieved by encoding anti-CRISPR mRNA that was selectively degraded by miR-122 abundantly expressed in the liver. [211]

Mature gRNA can also be generated with a similar mechanism utilizing miRNA-mediated RISC cleavage. A miRNA-mediated gRNA release platform (MICR) was achieved by flanking the gRNA sequence with two miRNA-binding sites (Figure 1.21b). The generation of the mature gRNA and its activity reflect the expression level of the miRNA in specific cell types. MICR can be adapted to be responsive to siRNAs as well. Since many miRNAs and siRNAs are restricted to cells of specific lineages or at different development or disease stages, this platform may be exploited for cell type-specific CRISPR-Cas9 functions (Figure 1.21b). [212]

Besides the RISC, RNase H is another endogenous enzyme that can be leveraged for hybridization-mediated activation of Cas9. For example, Ferry *et al*. designed a gRNA that forms a hairpin blocking the spacer domain. The loop of this hairpin is the target of an

ASO sequence such that Cas9 activity is dependent RNase H-mediated cleavage of the loop (Figure 1.21c) [213].

Another general concept for enzyme-mediated smart NATs employs a nucleic acid input that drives strand hybridization and displacement reactions that create substrates for Dicer or Drosha processing which in turn generates active siRNA. In one example, a Dicer substrate becomes inactive when hybridized to a lock strand. A mRNA trigger removes the lock via toehold-mediated strand displacement allowing for Dicer processing (Figure 1.21d) [214]. In another design, a RNA trigger binds to a hairpin-shaped sense strand, allowing hybridization to the antisense strand, which activates Dicer processing of the duplex (Figure 1.21e) [215]. Similarly, a conditional Drosha substrate can be activated by hybridizing to a trigger oligonucleotide to open a hairpin that blocks Drosha binding (Figure 1.21f) [216]. Although random trigger sequences were used in these studies, these strategies are general and can be adapted to any trigger nucleic acid, including endogenous RNA molecules. These strategies have yet to be demonstrated *in vivo*, likely because of the challenges regards the stability and delivery of the pro-drug RNA, and the choice of endogenous trigger RNA with adequate concentration. To overcome these challenges, Ren *et al*. incorporated a miRNA-triggered cascade reaction with *in situ* RNA assembly [217-219] (Figure 1.21g) and delivered the system using polyethylenimine [220]. The design split the guide and passenger strands of siRNA into two DNA/RNA hybrids (DR and D'R') and brought the two duplexes into spatial proximity by hybridizing these nucleic acids to a DNA scaffold, which increases reaction efficacy for intracellular siRNA generation. One of the hybrids (DR) possesses a miR-21 complementary toehold; miR-21 triggers the dissociation of DR and further allows D-D' hybridization, leading to the release of R' to

form RR' siRNA precursor. The released miRNA can further amplify this siRNA signal by triggering the next strand displacement to continuously generate siRNA [220].

The above summarized smart NATs with hybridization and strand displacement reactions as signal transducers and endogenous transcripts as input are modular due to the predictability of nucleic acid complementarity. As more disease-related transcripts are discovered by transcriptomics, smart NATs controlled by these specific transcripts can potentially enable on-demand and autonomous therapeutics based on *in situ* diagnosis with reduced off-target effect and toxicity.

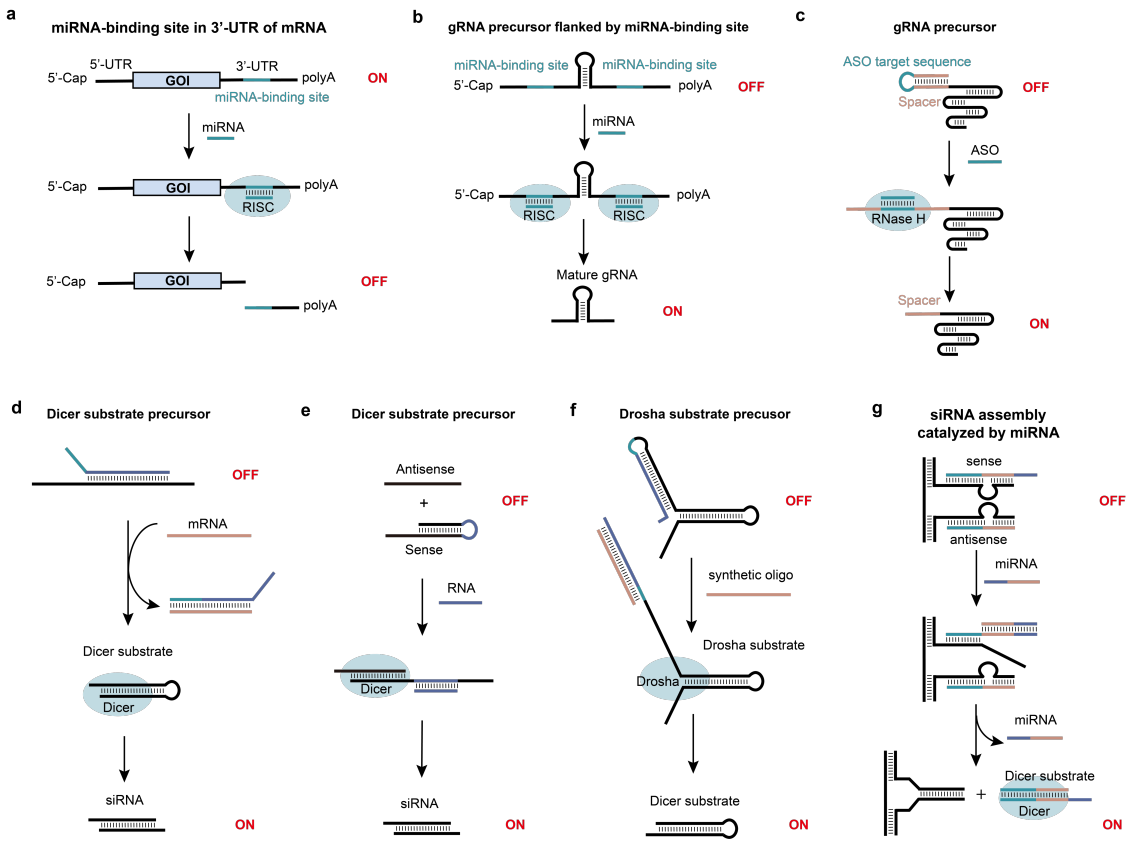

Figure 1.21 Hybridization and strand displacement-mediated enzyme activation allows generation or destabilization of NATs.
(a) Inserting miRNA target sites in 3'-UTR of mRNA enable miRNA and RISC mediated degradation of mRNA. (b) gRNA flanked by miRNA binding sites can be processed by RISC into mature gRNA after miRNA binding. (c) gRNA with the spacer domain blocked by a stem-loop is activated by RNase H mediated cleavage after hybridization of an ASO to the loop domain. (d) A linearized Dicer substrate hybridized to a lock strand is activated by mRNA trigger via toehold-mediated displacement. (e) A hairpin-shaped sense strand is linearized when bound to the trigger RNA, and reacts with the antisense strand, activating Dicer processing. (f) A Drosha substrate precursor is activated by a synthetic oligonucleotide and then processed by Drosha. (g) Split Dicer substrates patterned on a DNA scaffold re-associate and assemble into siRNA precursor induced by miRNA-triggered cascade reaction.

1.3.4 Protein-protein/aptamer interactions induce dissociation of nucleic acid complex for therapeutics release

To this point we have discussed the general concept of using intracellular inputs such as miRNA, mRNA as well as small molecules and proteins to trigger the activation/deactivation of gene regulation response. However, it is also desirable to create drug delivery systems that detect extracellular markers, such as cell surface receptors that are associated with a disease state. To achieve this goal, "spring-loaded" DNA nanostructures, aka "nanorobots" were engineered to release their payload upon encountering a cell surface marker (Figure 1.22 a, b). This approach takes advantage of protein-aptamer binding to mediate duplex dehybridization and therapeutic payload release in proximity to the target cell. In this strategy, the lock is usually a DNA duplex that undergoes target-induced switching between an aptamer-complement duplex and an aptamer-target complex. Douglas *et al*. designed a DNA barrel closed by two aptamer locks for different protein targets, which released fluorescence-labeled antibodies selectively when incubated with cells that express the corresponding key proteins (Figure 1.22a). [221] In another example, Li *et al*. designed a hollow tube-shaped DNA origami structure assembled from a sheet by hybridizing predesigned fastener strands containing DNA aptamers that bind nucleolin. Nucleolin is a protein specifically expressed on tumor-associated endothelial cells. Interestingly, aptamer binding to surface expressed nucleolin leads to both binding of the nanostructure to the cell as well as opening of the origami tube and exposure of thrombin in tumor-associated blood vessels, thereby inducing coagulation and tumor necrosis (Figure 1.22b). [222] These smart DNA nanostructure designs can enable drug delivery in a programmable manner in targeted tissue. To this end, stability of the nanostructure and toxicity of these foreign nucleic acids need to be considered. In addition, protein-aptamer triggered autonomous release of therapeutics from DNA

nanostructures relies on the efficiency and yield of the structure switching element. The response is highly dependent on the tug-of-war between the aptamer-target affinity and the aptamer-complement affinity and their respective concentrations; hence creating and testing new triggered structure-switching aptamers is difficult to optimize without extensive experimental testing. For the purpose of autonomous release triggered by diseased cell surface markers, SELEX or Cell-SELEX [223] should be performed with the specific marker or cell subtype to generate standard aptamers. Furthermore, these aptamers annealed with an antisense sequence should be screened to select aptamers that switch structures upon target binding. [224]

Antibody-antigen binding is another modality that triggers release of cargos, such as antibody-powered nucleic acid release reported by Ranallo *et al*. (Figure 1.22c). [225] The clamp-like structure is conjugated at the two ends with antigens. Antibody binding to the antigens induces disruption of Hoogsteen interaction and opening of the triplex-complex, resulting in the release of the cargo due to the weak Watson-crick interaction. This system was demonstrated in buffer but has not yet demonstrated potential for release of therapeutic oligonucleotides in cell experiments.

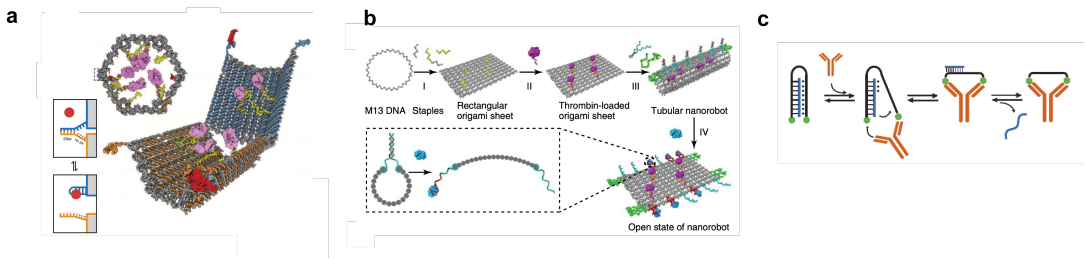

Figure 1.22 Dynamic DNA nanostructures for therapeutics release triggered by protein-aptamer binding (a, b) and protein-protein binding (c).
(a) A DNA nanobarrel is opened after the complementary fastener strand of the aptamer is displaced by protein binding. [221] (b) A DNA nanosheet forms a tube by hybridization of aptamer and its complementary fastener strand. The tube is opened after the trigger protein binds to its aptamer. [222] (c) A triplex-complex is disrupted via antibody-antigen binding to release the cargo strand. [225]

1.3.5 Future Perspectives of smart nucleic acid therapeutics

As summarized above, a wide range of programmable modalities have been adopted to realize controlled activation or deactivation of NATs. Based on the source of the trigger molecule, smart NATs can be controlled by externally added triggers or endogenously expressed triggers. Photochemical control provides spatiotemporal precision, but its clinical translation as smart therapeutics is limited by UV or visible light tissue penetration. Molecular triggering utilizing RNA aptamer-based ribodevices, strand hybridization/displacement and protein-ligand binding is more suitable for building autonomous agents that respond to disease markers and can be programmed to execute therapeutic functions based on *in situ* diagnosis. However, to this end, the discovery of disease- or cell subtype- specific markers (eg. metabolites, proteins, transcripts) and the ever-expanding number of molecular devices that interact with them in physiological conditions are critical for the growth of this field. Molecular triggering leveraging strand

hybridization/displacement is advantageous, as it is modular, and the triggering sequence can be arbitrary. Due to the predictability of nucleic acids, computing-aided design has been used to predict the sequences and structures of these devices, such as NUPACK [226], the toehold switch design web tool [227], and *iSBHfold* algorithm to optimize ASO sensing loops in the gRNA precursor design [213]. In addition, robust reporter cell lines make high-throughput, quantitative screening and characterization of large library of molecular devices possible.

One direction toward autonomous functionality of NATs is the development of "on-demand" therapeutics, which are reversible and controlled in an analog manner by implementing continuous computation in response to changing disease-indicating inputs. This will require increasing the lifetime of the smart NATs by incorporating chemical modifications. Another aspect that needs to be considered for clinical translation of smart NATs is their cellular entry. So far, the most commonly used vehicles for mRNA therapeutics and oligonucleotide therapeutics are LNPs. Inorganic nanoparticles, such as AuNPs have also been demonstrated to deliver smart NATs [204].

Besides the above-mentioned major mechanisms for controlling activity of smart NATs, other mechanisms have also been reported in the literature, such as chemical activation [228] and enzyme (Csy4) activation of gRNA [213]. Some novel mechanisms are also under development, such as mechanical force triggered release of therapeutics [229]. DNA nanostructures have been used to study molecular mechanics on living cell surface leveraging force-induced melting of DNA hairpins, duplexes and nanostructures [230, 231]. Although their applications are focused on probing force by fluorescence-based readout, mechanical force-triggered release of therapeutics, including intercalating

molecules, oligonucleotides and proteins from nucleic acid nanostructures can be foreseen. Utilizing heterogeneity in mechanical forces that cells apply on engineered matrix, such as implantations, therapeutics may be selectively delivered into desired cell subtypes.

1.4 miRNAs as specific transcript triggers for smart nucleic acid therapeutics

1.4.1 Biogenesis and mechanism of miRNAs

miRNAs functions as the guide strand for RNAi through binding to the 3'-UTR of mRNAs. miRNAs are typically 18-22 nt in length, with the domain at the 5' end that spans from position 2 nt to 8 nt (seeding sequence) being important for target recognition. miRNAs with identical seeding sequences belong to the same 'miRNA family'. A single miRNA can target hundreds of mRNA, and one mRNA can be regulated by several miRNAs.

As shown in Figure 1.23, miRNAs are transcribed by RNA polymerase II (pol II) and the primary transcript, or pre-miRNA, has a hairpin structure embedding the miRNA sequence. Pri-miRNA can be derived from individual miRNA genes, from introns of protein coding genes, or from polycistronic transcripts that often encode multiple, closely related miRNA. Pri-miRNAs are processed in the nucleus by the RNase III-type protein Drosha into ~70 nt long, hairpin-shaped precursors, or pre-miRNAs, with 2nt 3'-overhang. Pre-miRNAs are transported to the cytoplasm through the nuclear pore complex via Exportin 5 and processed by RNase III-type endonuclease Dicer into double-stranded miRNAs. The duplex miRNA is loaded into RISC, where one strand of the duplex is

selected as the guide strand (usually the 5p strand) while the passenger strand (miRNA*) is quickly removed by unwinding (AGO1, AGO3 and AGO4, which lacks slicer activity) or cleaved (by slicing-competent AGO2). [128] The resulted RISC-miRNA can mediate multiple turnover cleavage of target mRNA or suppress its translation [170].

Apart from the canonical miRNA biogenesis pathway, a small group of miRNAs can also be generated bypassing the process of Drosha or Dicer (Figure 1.23). For example, Drosha process is bypassed in the cases where pre-RNA precursor is generated through mRNA splicing [221] or directly through transcription [222]. In the case of miR-451, pre-miR451 after Drosha processing is too short to be processed by Dicer, and thus it is directly loaded onto and sliced by AGO2. [223, 224]

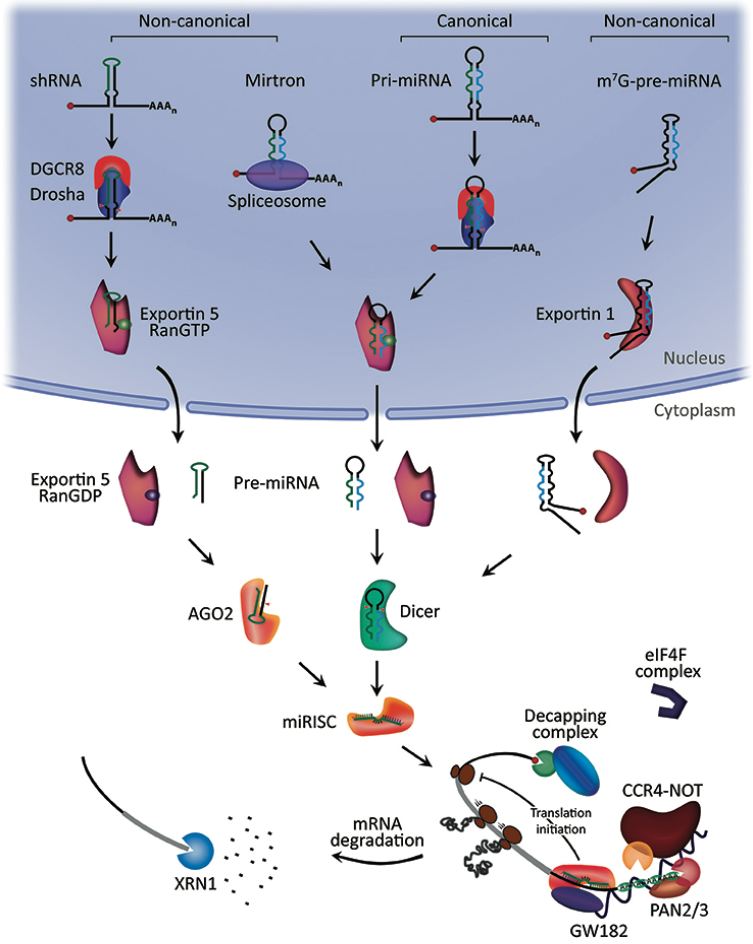

Figure 1.23 Biogenesis and mechanism of action of miRNA. [225]

1.4.2 Spatial expression pattern of miRNAs in different tissues and cell types

The tissue specificity of miRNA was initially investigated by northern blot analysis performed in miRNAs isolated from specific tissue or cell types or cloning of miRNAs from specific tissues followed by northern blot. Published in 2002, Lagos-Quintana *et al*. examined 9 mouse tissues and identified a few tissue specific miRNAs, including miR-1 (45% of all miRNAs in heart), miR-122 (72% in Liver), miR-143 (30% in spleen), miR-142 (30% in colon) and miR-124 (25%-48% in brain). [226] In 2004 and 2006, Chen *et al*.

[227] and Ramkissoon *et al*. [228] identified hematopoietic cell-specificity of several miRNAs (miR-181, miR-142, miR-223) in mouse and human, respectively. Later, *in situ* hybridization technique for detecting ~21nt RNAs utilizing LNA-probes (LNA-ISH) [229] was developed by Wienholds *et al*. With this technique, in 2005, Wienholds *et al*. reported temporal and spatial expression pattern of 115 conserved vertebrate miRNAs in zebrafish embryos by microarrays and *in situ* hybridization with LNA-probes (LNA-ISH). [230] This study not only revealed that 68% of the miRNAs are highly tissue specific, but also provided evidence for roles of miRNAs in differentiation or maintenance of tissue identity. Reported by Nelson *et al*. in 2006, miR-124a, miR-125b and miR-9 were demonstrated to be highly specific in human brain tissue utilizing LNA-ISH. [231] In 2007, Landgraf *et al*. reported miRNA profiling revealed by sequence analysis of small RNA clone library of human and mice, which indicated that a few miRNAs were exclusively expressed in individual tissues or cell types, and a third of the analyzed miRNAs were expressed with a high degree of tissue specificity. [232] Owing to the regulation effect of miRNA to mRNA targets, a correlation was also reported between tissue specific miRNAs and mRNAs that have corresponding seeding sequence in these tissues. [233]

Among all the miRNAs, miR-122 have been demonstrated to be exclusively expressed in the liver and constitutes 72% of the total miRNA pool in mouse liver. [234] Discovered by hybridization with radiolabeled probes and RNase protection analysis, the abundancy of miR-122 is at approximately 66,000 copies per cell in adult liver, which makes it the most abundant miRNA in all tissues. [235] miR-122 plays a role in regulation of cholesterol biosynthesis [236] and systemic iron homeostasis [237]. In addition, miR-122 targets several oncogenes, including a disintegrin and metalloprotease 17 (ADAM17),

which is involved in metastasis. [238] miR-122 levels were also shown to be reduced in hepatocellular carcinoma (HCC) compared to normal liver. [239, 240] Furthermore, miR-122 promotes hepatitis C virus (HCV) replication cycle by binding to the 5'-UTR of HCV RNA, which is a different process to the usual function of miRNA. [241, 242]

1.4.3 Dynamic miRNA expression levels in human disease

miRNA expression is highly dynamic, and they play important roles in various diseases, including cancer and cardiovascular diseases. The deregulation of miRNA expression can originate from either genetic abnormality or epigenetic regulation. [243]

miRNAs de-regulated in human tumors function as either tumor suppressors or oncogenes. Tumor suppressor miRNAs, such as miR-15a-miR-16-1, let7, and miR-29, target oncoproteins in various cancer pathways, including BCL2, RAS, MCL1, and MYC. [244-247] On the contrary, oncomiRNAs target tumor suppressors. For example, miR-21 suppresses apoptosis by targeting the tumor suppressors phosphatase and tensin homologue (PTEN) and programmed cell death 4 (PDCD4). [248, 249]

miRNAs have also been found to control functions in the cardiovascular system. [250] Specifically, many miRNAs are sensitive to different flow types, and play critical roles in endothelial dysfunction, and cause cardiovascular diseases. [251] For example, flow sensitive miR-712/205 family activates endothelial inflammation and permeability by downregulating tissue inhibitor of metaaloproteinase-3 (TIMP3), which activates matrix

metalloproteinases (MMPs) and a disintegrin and metalloproteinases (ADAMS), leading to atherosclerosis and abdominal aortic aneurysm. [252, 253]

Apart from flow sensitive miRNAs in endothelial cells, miRNA dysregulation in macrophages can also contribute to progression of atherosclerosis, such as miR-33. miR-33 is encoded within intron 16 of sterol-regulatory element-binding fator-2 (SREBF-2), a transcription factor regulating cholesterol uptake and synthesis. miR-33 is mostly expressed in macrophages and hepatic cells, and to a lesser extent in endothelial cells. Furthermore, miR-33 is expressed in a variety of mouse tissue, with the highest abundancy in liver and brain. In 2010, Rayner *et al*. reported that miR-33 regulate cholesterol homeostasis by targeting cholesterol efflux transporters, the adenosine triphosphate-binding cassette transporter (ABCA1) in human and mouse, and ABCG1 in mouse. [254] During atherosclerosis development, lipid-laden macrophages, or foam cells, accumulate in the artery wall, where they contribute to chronic inflammation and plaque progression. ABCA1 transports free cholesterol within the cell to lipid-poor apoA1 particles to form nascent high-density lipoprotein (HDL), which removes cholesterols from lipid-laden foam cells and provide anti-atherogenic effect. In 2011, Rayner *et al*. reported that miR-33 inhibition by anti-miR-33 in LDL receptor deficient mice resulted in reduction in plaque size and an increase in circulating HDL levels. [255]

Besides modulation of cholesterol transportation, miR-33 was also found to mediate macrophage polarization. Ouimet *et al*. reported a higher level miR-33 in M1 macrophage than M2 macrophages, and miR-33 regulates macrophage metabolic and inflammatory phenotype by modulating the balance between fatty acid oxidation and glycolysis via targeting AMP-activated protein kinase (AMPK). Furthermore, antagonism

of miR-33 in LDLR$^{-/-}$ mice resulted in enrichment of M2 markers in plaque macrophages and reduced systemic inflammation without altering HDL level. [256] In 2016, Lai *et al*. reported that miR-33 augmented Toll-like Receptor (TLR) signaling in macrophages by increasing cholesterol content in lipid rafts via down regulation of ABCA1, which indicated the role of miR-33 as an indirect regulator of innate immunity and a cross-talk between lipid homeostasis and inflammation. [257]

1.5 TNFα and HIF1α as a therapeutic target and their RNA therapeutics

1.5.1 TNFα as a therapeutic target for RNA therapeutics

1.5.1.1 Function and disease relevance of TNFα

Tumor necrosis factor α (TNFα) is a multifunctional cytokine that plays important roles in acute and chronic inflammation, anti-tumor and anti-infection responses. TNFα can be in both a 26 kDa cell membrane-associated form or a 17 kDa secreted form. Both forms are biologically active and trimerization is required for their activity. [258] The biological response of TNFα is mediated by two receptors, TNFR1 and TNFR2. TNFR1 activates transcription factor NF-ϰB, which induces the expression of other pro-inflammatory cytokines, such as interleukin-1 (IL-1); whereas TNFR2 also involves in protective and anti-inflammatory effects. [259]

TNFα plays important roles in the pathogenesis of many inflammatory and autoimmune diseases, including rheumatoid arthritis (RA) [260], inflammatory bowel disease (IBS) [261], and heart failure [262].

There are currently three protein- or antibody-based anti-TNFα drugs approved by FDA, which are Etanercept (soluble TNFR2 coupled to IgG Fc), infliximab (mouse-human chimeric anti-human TNFα antibody), and Adalimumab (human anti-human TNFα antibody). [258]

1.5.1.2 RNA therapeutics for TNFα

Antisense and DNAzyme strategies have been developed to target TNFα mRNA. ISIS 104838 [263] is a 20mer second-generation antisense with PS and 2'-MOE modification, which completed Phase II clinical trials for RA and Crohn's disease. Liposome SNA of ASO targeting TNFα was also developed by Exicure for topical delivery to treat psoriasis. In 2001, Iversen *et al*. first designed a DNAzyme targeting TNFα and reported that treatment with the DNAzymes improved hemodynamic performance in rates with postinfarction heart failure. [264] In 2016, Somasuntharam *et al*. reported that local injection of TNFα DzNPs in the rat myocardium following myocardial infarction resulted in anti-inflammatory effects and improvement in cute cardiac function. [127]

1.5.2 HIF1 α as a therapeutic target for RNA therapeutics

1.5.2.1 Regulation of HIF1α

Hypoxia-inducible factor 1 (HIF1) is a transcription factor that mediates adaptive response to oxygen level in tissues. HIF1 is a heterodimer consisting of two subunits, a

hypoxia-activated α subunit and a constitutively expressed β subunit. [265] There are 3 isoforms of the α subunit, HIF1α, HIF2α, and HIF3α. Target genes of HIF1α and HIF2α have overlap, although some genes can be preferentially regulated by one or the other. In addition, most HIF2α target genes are not substantially activated by hypoxia [266]. HIF3α functions as an inhibitor of HIF1α-induced transcriptional activation. [267, 268]

The synthesis of HIF1α is independent of O_2 level, whereas the degradation of HIF1α is regulated by O_2 dependent mechanism in three steps: modification of HIF1α with hydroxyl groups by prolyl hydroxylases (PHDs) [269], ubiquitination by E3 ubiquitin-protein ligases, including the von Hipple-Lindau tumor-suppressor protein (pVHL) [270], and degradation by proteasome of ubiquitylated protein. In addition, the factor-inhibiting HIF (FIH) hydroxylate HIF1α at asparagine residues on the C-terminus, resulting in blockage of the coactivators P-300/CBP binding to C-terminal transactivation domain of HIF1α and its inactivation. [271] In hypoxic condition, PHD and FIH activity are suppressed, leading to increased HIF1α activity, and binding of the HIF1α/β heterodimer to the hypoxia response elements (core binding site 5'-RCGTG-3', R=A or G) on target genes [272], such as vascular endothelial growth factor (VEGF).

Besides hypoxia, HIF1α can also be regulated in O_2 independent pathways by hormones and inflammatory cytokines, such as insulin [273] and IL-1β [274]. Additionally, HIF1α can also be regulated by miRNA, such as miR-20b. [275] Mutations in oncogenic genes have also been shown to stabilize HIF1α.

In addition, HIF1α is upregulated by flow conditions in vascular endothelia cells and atherosclerotic conditions. In 2017, Feng *et al*. reported that low shear stress induced

HIF1α in endothelial cells (ECs) in normoxic condition by NFκB-induced HIF1α transcript and induction of deubiquitinating enzyme Cezanne. [276] In 2019, Fernandez-Esmerats *et al*. reported disturbed flow induced HIF1α stabilization mediated by flow sensitive miR-483 and ubiquitin E2 ligase-C (UBE2C). [277]

1.5.2.2 HIF1α in cancer and cardiovascular disease

HIF1α is overexpressed in many cancers and associated with patient mortality and poor prognosis. HIF1α upregulation promotes cancer progression by involving in cell division, angiogenesis, glucose metabolism, fatty acid metabolism, amino acid metabolism, epithelial mesenchymal transition (EMT) and migration. [278, 279]

HIF1α also plays a role in cardiovascular disease by promoting endothelial cell dysfunction. Feng *et al*. reported that upregulated HIF1α by low shear stress induced proliferation and inflammation of ECs. It was also shown that EC-specific deletion of HIF1α in apolipoprotein E-deficient mice showed reduced inflammation and endothelial proliferation in partially ligated arteries. [276] Fernandez-Esmerats *et al*. showed that increased HIF1α level induced by disturbed flow resulted in endothelial inflammation and endothelial mesenchymal transition (EndoMT), leading to aortic valve calcification. [277]

1.5.2.3 HIF1α antisense oligonucleotide

EZN2968 is a 16mer ASO targeting HIF1α mRNA with a PS and LNA modified gapmer structure. It was shown to inhibit HIF1α on both mRNA and protein level in various cancer cell lines, as well as *in vivo* to knock down liver HIF1α expression following intraperitoneal injection. In addition, nude mice xenografted with DU145 cells pre-transfected with EZN2968 showed reduction of tumor compared to control oligonucleotide transfected group, and the mice further treated with EZN2968 showed an increased reduction. [280] A pilot trial of EZN2968 in patients with refractory solid tumors after intravenous infusion provided a preliminary results showing a reduction of HIF1α mRNA and protein expression in tumor biopsies. [281]

CHAPTER 2. SPECIFIC AIMS AND HYPOTHESIS

2.1 Significance and impact

The clinical potential of oligonucleotide RNA-targeting therapeutics to control expression of disease-related genes for disease treatment has been emerging. The advancement of medicinal chemistry with enhanced delivery strategies to get the oligonucleotides into the cells has dramatically increased potential clinical utility of these oligonucleotide therapeutics, opening the opportunity to treat conventionally intractable diseases.

To date, most of the oligonucleotide drug candidates are directed to the liver systemically with the assistant of GalNAc ligand conjugation [282] or lipid nanoparticle formulations [283] to treat liver-mediated diseases. Beyond liver, oligonucleotide drugs targeting the central nervous system can be delivered by intrathecal injection into the spinal canal, such as Nusinersen to treat SMA [284] and Tominersen (in Phase 3 trial) to treat Huntington's disease [285]. In order to broaden the range of diseases that oligonucleotide therapeutics could potentially address, developing delivery technologies that allow efficient and specific targeting of additional tissues is a major area of interest in the oligonucleotide research field. These strategies mainly include conjugation with antibodies and ligands that recognize specific surface receptors and high-throughput screening for nanoparticle formulations with tissue tropism, as discussed in Chapter 1.1.2. Although powerful, these strategies may encounter bottlenecks in diseased conditions where a specific surface marker is absent or unknown, or a subtype of cells within the same tissue

needed to be targeted. Therefore, new strategies to improve specificity of oligonucleotide therapeutics that would allow for more precise targeting capabilities and broader applications is needed.

In the past decade, transcriptomic techniques, such as RNA-seq [286] and single-cell RNA seq [287], has become one of the most powerful tools to investigate human diseases and identify molecular biomarkers and therapeutic targets. [288] Transcriptome profiling revealed that dysregulated or tissue/cell specific transcripts, including mRNA or non-coding RNAs could distinguish diseased cell populations [289], tissues [290, 291] or cell subtype [292] of interest in addition to protein markers. Therefore, utilizing transcript specificity to govern the activity of oligonucleotide therapeutics could potentially enhance specificity of oligonucleotide drugs to target a broader variety of cell subtypes or tissue.

The objective of this dissertation is to examine the possibility and potential to use disease-related or cell type-specific transcripts as a trigger to modulate the activity of oligonucleotide therapeutics and their nanoparticle conjugates, providing a proof-of-concept for the future design strategy of smart therapeutics in clinically translatable models.

2.2 Overall hypothesis

The overall hypothesis is that the specificity of RNA therapeutics could be improved by using transcripts as the triggering stimulus to control the activity of therapeutic oligonucleotides. Specifically, we hypothesize that miRNAs are an effective transcript

trigger, while DNAzyme and ASO are effective oligonucleotide therapeutics to inhibit expression of TNFα and HIF1α, respectively in cells.

2.3 Rationale

We chose TNFα and HIF1α as our targets for model RNA therapeutics. Although these two genes are typically induced in many pathological conditions including cancer and cardiovascular disease as discussed in Chapter 1.5, they also play important roles in a variety of normal cellular homeostasis. Therefore, systemic inhibition of these proteins by either conventional therapeutics or RNA therapeutics could potentially lead to adverse events. For example, TNFα plays an important role in anti-infection and anti-cancer effects, systemic inhibition of TNFα could raise the risk of cancer and infection. [293, 294] HIF1α has been found to be required for repairing acute injury and wound healing. [295, 296] In addition, VEGF, a direct target of HIF1α, is the predominant proangiogenic factor, therefore, its downregulation by systemic HIF1α inhibition could severely impair necessary angiogenetic processes and tissue vascularization. [297]

As miRNA triggers, we selected two representative miRNAs: miR-33 as a dysregulated miRNA in a diseased condition, and miR-122 as a tissue/cell type specific miRNA. miR-33 is a key regulator of cholesterol homeostasis and has been shown to be upregulated in pro-inflammatory M1-like macrophages and foam cells in atherosclerosis, which express pro-inflammatory cytokines, including TNFα. [256] Therefore, leveraging the high level of miR-33 to trigger inhibition of TNFα could limit the action of TNFα

DNAzyme to pro-inflammatory macrophages. Among all miRNAs, miR-122 is the most tissue specific miRNA that is exclusively expressed in the liver (hepatocytes) with high abundancy [234], which makes it an ideal tissue/cell type specific miRNA for optimizing the design of conditional RNA therapeutics.

The triggering mechanism adopted by the design of conditional therapeutics is toehold-mediated strand displacement/exchange, which is a reaction to exchange one strand (output) of nucleic acid with another strand (input) [298]. This reaction allows interactions between the inactivated therapeutics and the trigger miRNA with tunable thermodynamics and kinetics.

If our design principle proves to be successful, one can engineer conditional RNA therapeutics against a wide variety of targets that are activated using different transcriptional inputs.

To facilitate the cellular internalization of the conditional therapeutics, we also sought to conjugate the conditional therapeutics on AuNPs to form conditional DNA-AuNP conjugates. The intracellular disassembly process could potentially affect the potency and triggering mechanism of the conditional therapeutics and may provide insight on improving the design of conditional therapeutics by chemical modifications or anchoring chemistry to the AuNP surface. Therefore, information regarding the investigation of the intracellular fate of DNA-AuNP conjugates was also included in this dissertation.

2.4 Specific aims

2.4.1 Specific aim 1: Design and optimize miR-33 inducible TNFα DNAzyme NPs

DNA-NP conjugates have been used to knockdown gene expression transiently and effectively, making them desirable tools for gene regulation therapy. DNA-NPs are constitutively active and are rapidly taken up by most cell types, and thus offer limited control in terms of tissue- or cell type- specificity. In this specific aim, we take a step toward solving this issue by incorporating toehold-mediated strand exchange to switch the DNA-NPs from an inactive state to an active state in the presence of a specific RNA input. As a proof-of-concept, we designed conditional DNAzyme-nanoparticles (conditional DzNPs) that knockdown the mRNA transcripts of TNFα upon miR-33 triggering. Firstly, we screened for and optimized a DNAzyme that knockdown TNFα in mouse macrophages. We then demonstrated toehold-mediated strand exchange and restoration of TNFα DNAzyme activity in the presence of the miR-33 trigger, with optimization of the preparation, configuration and toehold length of conditional DzNPs. Our results indicated specific and strong ON/OFF response of conditional DzNPs to the miR-33 trigger in buffer. Furthermore, we demonstrated endogenous miR-33 triggered knockdown of TNFα mRNA in mouse macrophages, implying the potential of conditional gene regulation applications using these DzNPs.

2.4.2 Specific aim 2: Investigate the fate of DNA-AuNP conjugates within cells using fluorescence lifetime imaging

The precise mechanism of DzNP activation is unclear and it is possible for the triggering step to occur on the AuNP surface or alternatively, the triggering could occur after the locked duplex is released off the AuNP. In order to better understand the disassembly kinetics and role of nuclease and reducing environment on the disassembly of DNA-AuNP, which could potentially shed light on better design of conditional oligonucleotide AuNP conjugates, we sought to track the disassembly of DNA-AuNP conjugates with fluorescence lifetime imaging (FLIM). By tracking the dissociation of the fluorophore tagged on DNA from AuNP, we found that unmodified DNA-AuNPs disassembled rapidly after entering mouse macrophages, whereas chemical modification significantly decelerated the process. However, strengthening the Au-thiol bond did not further slowdown the disassembly. This study underlined the significance of chemical modifications on oligonucleotides tethered on their AuNP conjugates for gene regulation purposes, even though these SNAs have been reported to provide nuclease resistance compared to their linear counterparts [94].

2.4.3 Specific aim 3: Design and optimize miR-122 inducible HIF1α antisense

ASOs are an emerging class of promising therapeutics to treat diseases. However, like other oligonucleotide therapeutics, ASOs alone lack targeted actions only in desired cell subtypes or tissues, raising potential concerns regarding unwanted effects in unintended cells and tissues. To provide a better control over ASO activity only in targeted cells, we designed a miR-122-inducible HIF1α ASO. Our aim is to develop a conditional HIF1α ASO, which can be activated to inhibit HIF1α only in the presence of a trigger

miRNA via a toehold exchange reaction. To test the proof-of-concept, we used miR-122 since it is a hepatocyte-specific miRNA. First, we tested several duplex structures and their chemical compositions and found that nuclease-resistance and thermostability are both required for effective conditional ASOs with minimal spontaneous dissociation. Next, we screened for the conditional ASOs that can be activated and knockdown HIF1α upon triggering with synthetic miR-122 mimic and endogenous miR-122. We found that the activation of conditional ASO depends on the miR-122 level and the presence of the toehold. The design principle of the conditional miRNA-inducible ASO provides a proof-of-concept that it is feasible to develop specific transcript-inducible ASOs to impact cell type, cell condition, or disease-dependent control of oligonucleotide therapeutics.

CHAPTER 3. CONDITIONAL DEOXYRIBOZYME-NANOPARTICLE CONJUGATES FOR MIRNA-TRIGGERED GENE REGULATION

Chapter 3 is reproduced with permission from Zhang, Jiahui, *et al*. "Conditional Deoxyribozyme–Nanoparticle Conjugates for miRNA-Triggered Gene Regulation." *ACS Applied Materials & Interfaces* 12.34 (2020): 37851-37861.

3.1 Introduction

Programmable control of gene expression is critical for constructing biological circuits for applications such as genetics research, creating models of disease, and high-specificity gene therapy. The earliest conditional gene regulation strategies include drug-inducible systems [299] and Cre-mediated excision systems [300], which utilize regulating molecules or recombinases to trigger expression of interfering RNAs to knock down genes of interest. Recently, conditional CRISPR-Cas9 systems utilizing structure-switchable [301] or toehold-gated guide RNA (gRNA) [191, 194, 302] have been created, which use either a ligand-induced conformational switch or toehold-displacement to expose the hidden spacer region on gRNAs. Another strategy for conditional CRISPR-Cas9 systems relies on transcription of pre-gRNA flanked by miRNA binding sites, which could be processed by Dicer to release mature gRNA upon miRNA binding. [207] Despite the robustness of these systems in activating or inactivating gene expression, the need to

genetically engineer target cells or organisms using virus-based vectors and plasmid transfection for the delivery of these conditional systems hinders their potential clinical applications as gene regulatory therapeutics.

Non-genetically encoded oligonucleotides, such as siRNA, antisense and deoxyribozymes (DNAzymes), can be transiently delivered to regulate gene expression, and thus are more practical for therapeutic purposes. One prominent strategy to generate triggered oligonucleotides employs photocaging groups on the nucleotide bases to disrupt hybridization between oligonucleotides and their target mRNA. [139, 140, 303] Light irradiation uncages the oligonucleotides and thus restores their activity. Although photochemically-triggered gene regulation using caged oligonucleotides provides a high degree of spatial and temporal control, this approach is limited therapeutically due to tissue damage caused by UV irradiation and the sub-mm penetration of light into tissue. In addition, this strategy relies on external intervention, thus lacking the ability to autonomously implement gene regulation based on endogenous cellular information. Therefore, conditional regulation of gene expression by oligonucleotide therapeutics in response to endogenous inputs is ideal for the purpose of smart gene regulation therapies. To achieve this goal, conditional siRNA responding to endogenous transcripts that drive toehold-mediated stand displacement have been created either by using a conditional Dicer substrate [209] or by the triggered assembly of siRNA. [198] These examples carry tremendous potential for toehold-gated oligonucleotides activated by endogenous nucleic acids as smart therapeutics; however, they are confronted with the common challenges facing RNA therapeutics, including stability against nucleases and poor cellular uptake.

An alternative class of gene regulatory agents are DNA-NP conjugates, or spherical nucleic acids (SNAs), which are polyvalent oligonucleotides-modified nanostructures, most commonly gold nanoparticles (AuNPs). [93] DNA-NPs confer advantages compared to linear oligonucleotides in terms of reduced susceptibility to nuclease and greater cellular uptake.[94, 124, 127] DNA-NPs have been shown to enter virtually all cell types, through a mechanism that is mediated by scavenger receptors. [129, 130] Thus DNA-NPs lack cell type or tissue specificity in their gene regulation functions. Strategies to enhance the specificity of DNA-NPs mainly involve passive targeting, which includes localized delivery by topical application [304] or enhanced permeability in tumors, [125] and active targeting via incorporating targeting moieties such as monoclonal antibodies on DNA-NPs, [99] which directs their accumulation to the targeted tissues. However, to the best of our knowledge, there are no DNA-NPs that conditionally execute gene regulation function based on the detection of intracellular inputs. Therefore, we incorporated programmability into DNA-NPs by leveraging toehold exchange, aiming to develop smart NP gene regulation agents with inherent specificity.

MicroRNAs (miRNAs) are short non-coding RNAs, which are 18-23 nucleotides (nt) in length and regulate gene expression post-transcriptionally.[305, 306] They bind to the 3'-untranslated region (UTR) of target mRNAs, leading to degradation of the target mRNAs or inhibition of their translation. The specificity of miRNA for target recognition is based on Watson-Crick pairing of the 5'-seeding region (nucleotides between position 2-8 nt) of the miRNA to the complementary sequence of target mRNA. Besides their roles as key gene regulation factors, expression level of many miRNAs are unique in various cells and tissues under different developmental stages and pathophysiological conditions,

[226, 232] providing an opportunity to utilize them as a disease- or tissue-specific intracellular trigger. Here, we designed conditional DNA-NPs, in which activity of the gene regulatory effector can be controlled by an endogenous miRNA.

The 10-23 DNAzyme is composed of a 15 nt catalytic core and two recognition arms, which can selectively bind to and degrade target mRNA. [54] Compared to siRNA therapeutics, DNAzymes offer several advantages including enhanced stability, cost-effective synthesis and facile programmability due to their single-strand nature. Previously, we and others characterized DNAzyme-NP conjugates and showed their efficacy in regulating gene expression *in vitro* [94, 307] as well as in rat models [127]. In this study, we chose miR-33 as the input and a TNFα DNAzyme as the gene regulation effector to construct a model system for miRNA-triggered gene regulation. Increased level of miR-33 is known to promote lipid accumulation in macrophages by decreasing a critical cholesterol transporter ATP-binding cassette transporter-1 (*ABCA1)*, and to drive polarization of macrophages toward the proinflammatory M1 phenotype in atherosclerosis. [254, 256, 308] During atherosclerosis development, miR-33 overexpressing lipid-laden macrophages, or foam cells, accumulate in the artery wall, where they contribute to chronic inflammation and plaque progression by expressing pro-inflammatory cytokines, including TNFα. [309] Inhibition of TNFα has been shown to slow the progression of atherosclerosis, [310] but systemic inhibition of TNFα using antibody therapeutics are not problem-free as most patients develop anti-antibodies over time, [311] and it also carries increased risk of infection and cancer as TNFα plays important roles in immune function. [293, 294, 312] The development of selective anti-TNFα therapeutics can address the limitations inherent to systemic delivery of TNFα antibody. DNA-NP conjugates have

been reported to effectively internalized by macrophages in atherosclerotic plaques, [313] which shows their potential as therapeutic agents targeting macrophages in atherosclerosis. In addition, the cost and ease of producing DNA-NPs is significantly favorable over that of biologics. Therefore, we aimed to design conditional TNFα regulation DNA-NPs, which silences TNFα induced by high miR-33 expression level, potentially leading to regulation of TNFα more selectively in pro-inflammatory lipid-laden macrophages in atherosclerosis.

3.2 Design of conditional DNAzyme NPs

Figure 3.1 depicts the overall design of the conditional DzNPs and its functional mechanism. The specific sequences that we used are shown in Figure 3.5a. The conditional Dz is a duplex composed of a Dz strand hybridized to a lock strand, which we call the locked Dz. The lock strand consists of 3 domains: a toehold domain (α'), a branch migration domain (β') and a lock domain (γ'). The α' and β' domains are antisense to the miRNA (α + β) that serves as the trigger, and the γ' domain is complementary to the left arm (γ) of the Dz. To avoid inadvertently introducing the miR-33 seeding sequence into cells, the toehold domain (α') was designed to be complementary to the 5' end (α) of miR-33 (Figure 3.5a). The Dz strand was also engineered to display the β sequence of the 5' terminus of miR-33 to stabilize binding to the lock strand. Initially, the left arm of the Dz (γ) is bound to the lock strand, inactivating its cleavage activity against TNFα mRNA target. The locked Dzs are attached to the surface of AuNPs to form locked DzNPs in order to facilitate their cellular uptake. We hypothesized that, in the presence of trigger miRNA in the cytosol, the α domain of the miRNA binds to the α' domain on the lock strand and

initiates toehold exchange that is driven to completion via hybridization of the miRNA's β domain to the lock strand's β' domain. This leads to unlocking of the Dz strand and thus its release from the surface of the AuNPs. The released free Dz strand is then active to cleave TNFα mRNA, leading to reduction of TNFα levels. We ensured that the locked Dz remains hybridized at 37 °C in the absence of miR-33 by designing a thermally stable complementary sequence (*vide infra*) in order to minimize spontaneous activation. Note that, while the 3' recognition (right) arm of the Dz is available for binding to TNFα mRNA as a remote toehold, such a mRNA-mediated unlocking process is hindered by the large kinetic barrier for branch migration due to the spacing introduced by the 15 nt catalytic core. [314] This is an inherent advantage to use Dzs in this design. Our results, vide infra, confirm this prediction. Our work also shows that only a specific miRNA can drive activation of the locked Dz because the activation barrier for dehybridization is significant, and lock-miRNA toehold binding (α' to α) is essential for accelerating the unlocking process.

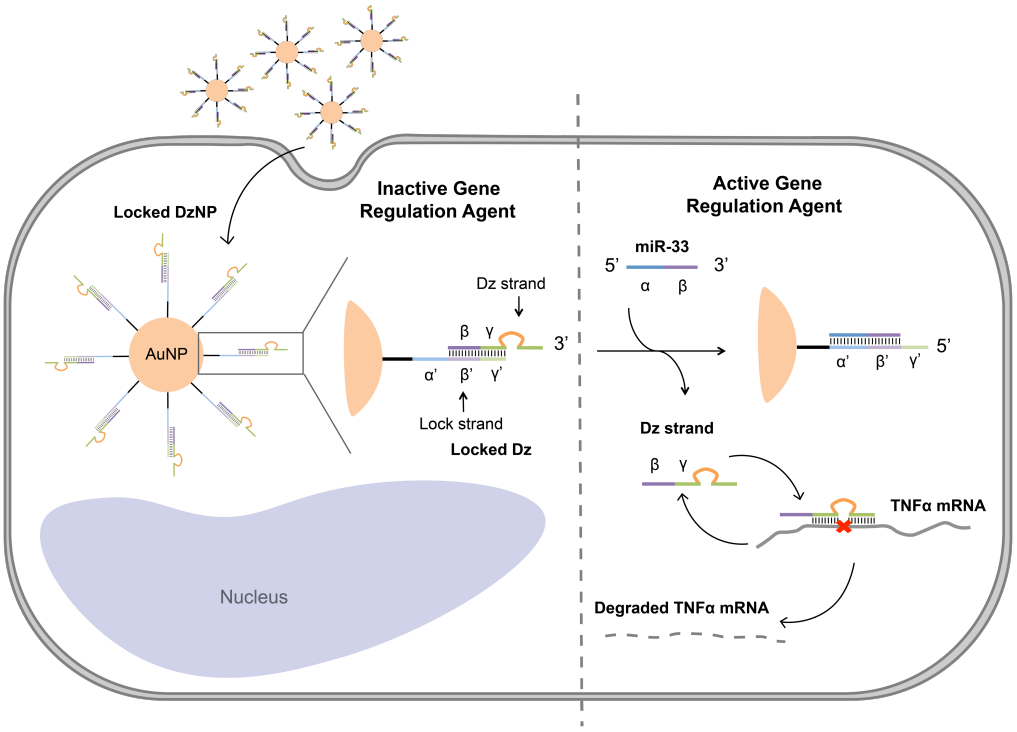

Figure 3.1 Schematic description of miR-33 induced TNFα knockdown by locked DzNPs.
The locked DzNPs are composed of Dzs that are inactivated by hybridization to a lock strand attached to the surface of AuNPs. The lock strand consists of 3 domains: toehold domain (α'), branch migration domain (β') and lock domain (γ'). The α' and β' domains comprise the anti-miRNA sequence, and the γ' domain is complementary to one binding arm of the DNAzyme. Since one binding arm of the Dz is blocked, its cleavage activity against its target mRNA is deactivated. However, a trigger miRNA can bind to the α' domain and initiate toehold exchange, thus leading to release and activation of the Dz strand followed by cleavage and degradation of its target mRNA.

3.3 Results

3.3.1 Screen and Optimization of mouse TNFα DNAzyme

Based on our prior work targeting TNFα in a rat model, [127, 264] we screened a small library of Dzs that target the mouse TNFα mRNA and identified a Dz that knocks down TNFα most effectively. The screen was necessary, as the prior Dz had been

optimized for the rat TNFα mRNA, and our present study focused on mouse models. Dz library selection was guided using a customized sequence search and binding optimization algorithm described in Figure 3.2a. We selected 8 Dzs targeting different regions of mouse TNFα mRNA and transfected them in RAW264.7 cells, a mouse macrophage cell line, to evaluate their TNFα knockdown efficacy at both the mRNA and protein level (Figure 3.2b,c). We found that the most active Dz (Dz-168) targets the AU junction in the start codon at position 168 nt of the mouse TNFα transcript (NM_001278601.1). This Dz is similar to the prior rat/human Dz as it targets the same start codon despite having a 2 nt difference compared to the rat Dz. To maximize the Dz activity, we performed a substrate cleavage assay to compare the catalytic activity of Dzs with different binding arm lengths (7 nt, 8 nt and 9 nt) as well as with or without 2'-O-Methyl (2'-OMe) modification (to enhance nuclease resistance) on the four most external nucleotides (Figure 3.3a). The Dzs were incubated with FAM-labeled substrates mimicking the mouse TNFα mRNA sequence for 140 min (Figure 3.3b), and the reaction mixture was resolved using a denaturing gel (Figure 3.3c). We found that increasing binding arm length from 7 nt to 9 nt resulted in increased Dz activity, which is likely due to enhanced binding affinity. Incorporating four 2'-OMe modified nucleotides to the terminal ends of the binding arms led to increased activity of Dzs with 7 nt and 8 nt arms (27% to 52% or 46% to 55% substrate cleaved, respectively), but the 9 nt arm Dz maintained a similar level of activity with and without 2'-OMe modification (65% substrate cleaved). We next compared the TNFα knockdown activity of the 2'-OMe modified Dz with 7 nt and 9 nt arms in mouse primary peritoneal macrophages and found similar levels of TNFα knockdown (~60%) (Figure 3.3d). Based on these results, we chose to move forward with the 9 nt arm 2'-OMe

modified Dz for subsequent work, given its efficacy both in buffer and *in vitro*. Previous studies of Dz kinetics showed that designing binding arms with too high an affinity for substrate reduces Dz catalytic activity by slowing the product releasing step. [315] Therefore, aiming to further improve Dz activity by adding more nucleotides to the binding arms or introducing modifications that enhance substrate affinity will likely have diminishing returns and may inhibit Dz activity.

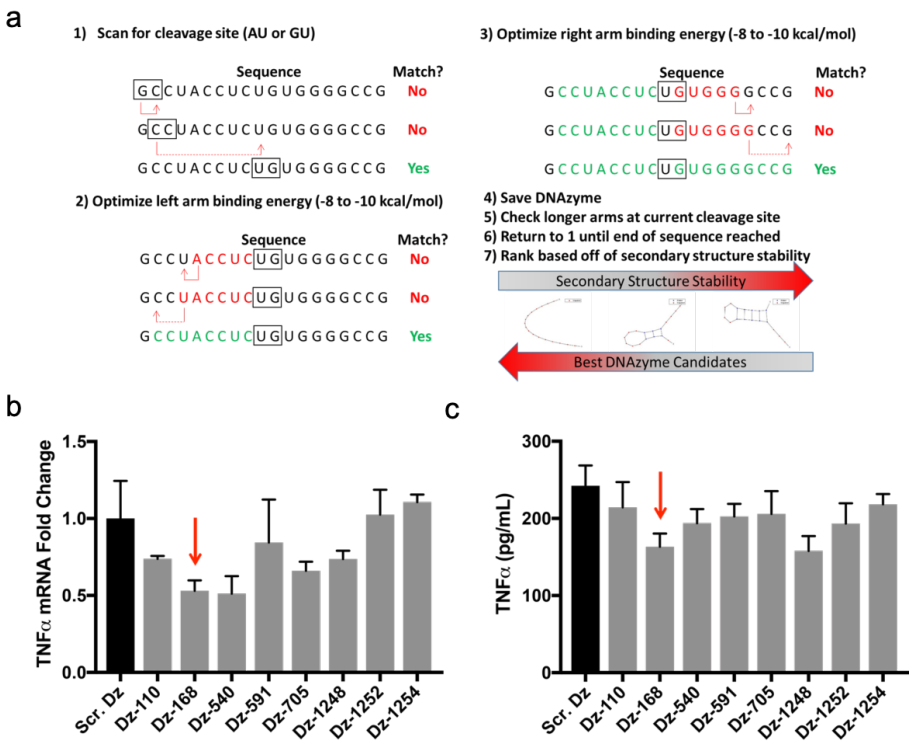

Figure 3.2 Screen of a small library of DNAzymes that target mouse TNFα in RAW264.7 cells.

(a) Schematic describing the computational DNAzyme selection process. First, the mRNA sequence is scanned for target sites and, at each target site, arm length is tuned until each arm has a free energy of hybridization within a specified range. Target sequences are then ranked by secondary structure free energy and stored. This process is repeated for the entire mRNA sequence and multiple DNAzymes can be obtained for a given target site. (b, c) RAW264.7 cells were transfected with 200 nM of each DNAzyme using Oligofectamine, and incubated for 24 h. A non-specific DNAzyme (NS Dz) was included as a negative control. The standard manufacturer recommended concentration of Oligofectamine was used for this screen (2 μL/well for 24 well plate). Each well was plated with ~100,000 cells. (b) RNA was isolated using RNease kit (QIAGEN #74104), and TNFα mRNA levels were quantified by qRT-PCR. The primers are listed in Table S3. (c) The cell medium was collected for ELISA analysis of secreted TNFα using a commercial ELISA kit (Invitrogen #88-7324-22). Sequences for each DNAzyme are included in Table S2. The error bars represent SEM of triplicate samples. The red arrow corresponds to the DNAzyme used in this work.

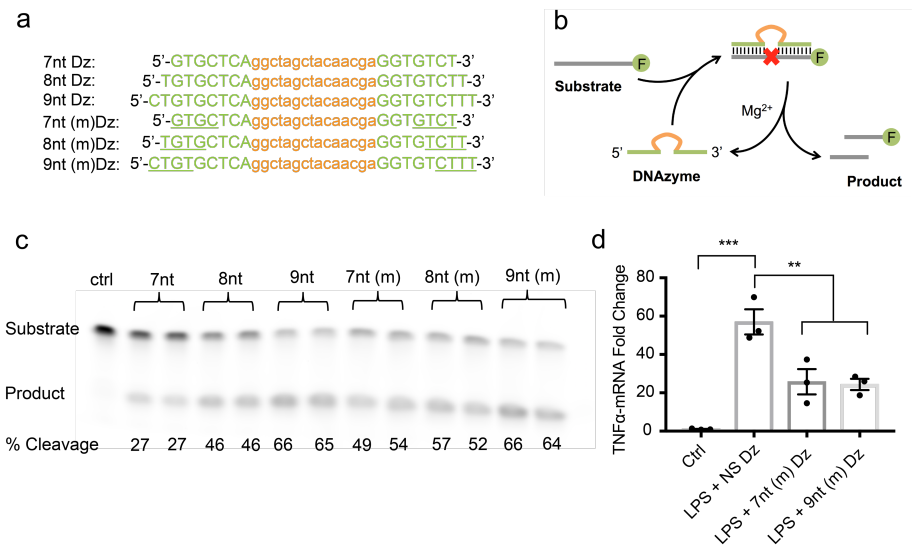

Figure 3.3 Optimization of TNFα DNAzyme Dz-168.
(a) Sequences of mouse TNFα DNAzyme (Dz-168) with different arm lengths and with or without 2'-OMe modifications. The green color corresponds to the left and right arms of the Dz that are complementary to the start codon region of mouse TNFα transcript. The lowercase orange sequence is the 10-23 catalytic domain of the Dz. The underlined nucleotides are 2'-OMe modified. (b) Schematic of substrate cleavage assay used to quantify catalytic activity of DNAzymes. (c) DNAzyme catalyzed multiple turnover of substrate cleavage. 200 nM of DNAzymes were incubated with 1 μM FAM-labeled substrates in 50 mM Tris-HCl supplemented with 150 mM NaCl and 2 mM $MgCl_2$ with pH 7.4. After incubation in a water bath at 37 °C for 2 h 20 min, the reaction mixture was mixed with the same volume of gel loading buffer and subjected to 15% Mini-PROTEAN® TBE-Urea Gel. The gel was run with 170 V in 1× TBE buffer and imaged with an Amersham Typhoon Biomolecular Imager using the FITC channel. The % cleavage values were determined using ImageJ analysis after background subtraction. (d) Plot showing TNFα levels in peritoneal macrophages transfected with non-specific (NS), 7nt(m) and 9nt(m) DNAzyme at a concentration of 1 μM. 24 h after transfection, 0.5 ng/mL lipopolysaccharide (LPS) was added, and cells were incubated for another 4 h before RNA isolation and qPCR analysis of TNFα mRNA level. The error bars represent SEM and each dot represents a biological replicate (**p<0.01, ***p<0.001, one-way ANOVA with Tukey's multiple comparison).

3.3.2 Conditional DNAzyme activation triggered by miR-33 in buffer

The locked Dz was prepared by annealing the Dz strand and the lock strand at a 1:1 ratio. The Dz strand was labeled with Cy5 to facilitate visualization in gel analysis. It is

important to note that the Dz modified with β domain and Cy5 showed similar activity compared to the parental Dz lacking β domain and Cy5, based on a substrate cleavage assay as described above (Figure 3.4). As expected, the Dz showed a ~6-fold inhibition of activity upon locking (Figure 3.4). We next tested the efficiency of toehold exchange between the locked Dz and the miR-33 trigger (DNA analogue of miR-33 for stability consideration), and then quantified Dz activity in buffer (Figure 3.5b). The locked Dz and the miR-33 trigger were incubated at 37 °C for 2 h, and then analyzed by native PAGE gel electrophoresis to determine the interactions among Dz strand, lock strand and miR-33 trigger. A scrambled miR-33 sequence (scr. miR-33) was used as a control to verify the specificity of the toehold exchange. The gel was stained with SYBR Gold to visualize all DNA species, whereas the Cy5 fluorescence indicated the Dz strand specifically. As shown in Figure 3.5c, in Lane 3 loaded with locked Dz incubated with miR-33 trigger, the Cy5 channel showed a shift in the locked Dz band, confirming its dehybridization due to toehold exchange. The percentage of unlocked Dz strand was ~61% as quantified by measuring the intensity of the bands after background subtraction. This exchange was specific as there was no shift in Lane 4 loaded with locked Dz incubated with scr. miR-33. To confirm that the miRNA rescues Dz catalytic activity, locked Dz was incubated with miR-33 trigger along with FAM-labeled substrates (locked Dz: miR-33: substrate=1:1:5) at 37 °C for 2 h and 22 h. Gel electrophoresis of the reaction mixtures showed that locked Dz incubated with miR-33 trigger showed an ~8 fold increase of substrate cleavage at the 2 h time point and near-completion of the substrate cleavage at the 22 h time point; whereas locked Dz incubated with scr. miR-33 exhibited background activity (Figure 3.5e). Together, these

results demonstrate the specificity of toehold exchange as well as the restoration of Dz activity upon triggering by the miR-33 mimicking strand in buffer.

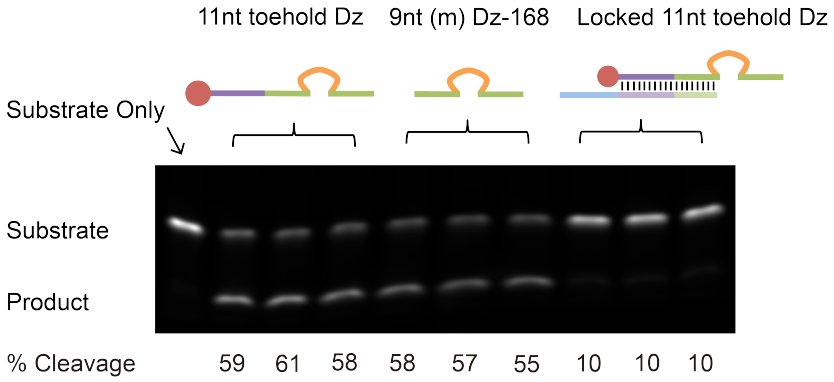

Figure 3.4 Activity of Dz strand and locked Dz compared to parental Dz-168 (9nt modified arms).
To quantify Dz activity, 200 nM 11nt toehold Dz, parental Dz-168, and locked 11 nt toehold Dz were incubated with 1 μM FAM-labeled substrate in 50 mM Tris-HCl supplemented with 150 mM NaCl and 2 mM $MgCl_2$ with pH 7.4 at 37 °C for 3 h. The reaction mixture was then subjected to 15% Mini-PROTEAN® TBE-Urea Gel. The first lane only includes substrate. The next three lanes were replicates of the 11 nt toehold Dz, followed by three replicates of the parental Dz-168, and finally by the 11 nt toehold Dz hybridized to the lock strand. The % cleavage values were determined using ImageJ analysis after background subtraction.

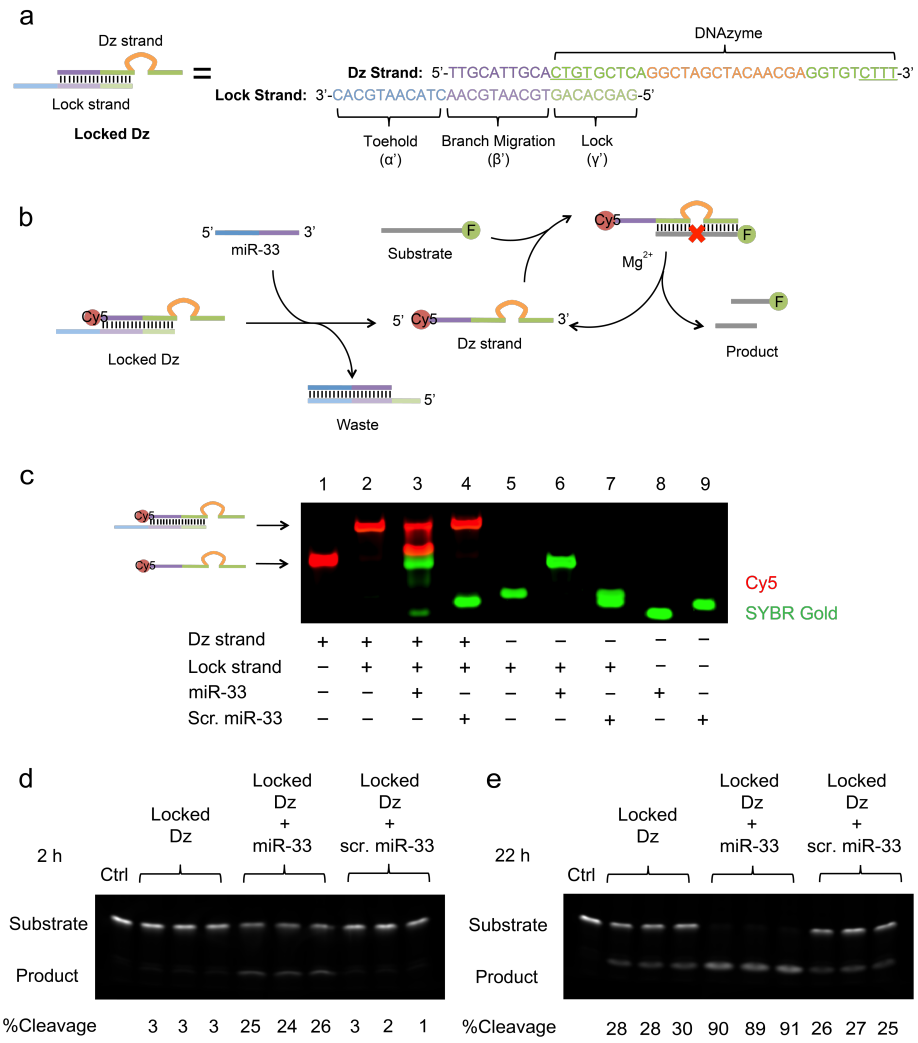

Figure 3.5 Design and validation of toehold exchange and activation of locked Dz by miR-33 trigger in buffer.

Design and validation of toehold exchange and activation of locked Dz by miR-33 trigger in buffer. (a) Design and sequence of locked Dz. (b) Scheme depicting activation of locked Dz by miR-33 trigger and substrate cleavage by activated Dz strand. Underscore indicates 2'-OMe modification. (c) Gel image showing toehold exchange between locked Dz and miR-33 trigger. [locked Dz] = 1 μM, [miR-33 trigger] = 1 μM, [scr. miR-33] = 1 μM, [locking strand] = 1 μM; 37°C for 2 h. Red channel indicates Cy5 fluorescence; Green channel indicates SYBR Gold staining. (d, e) Substrate cleavage activity of locked Dz incubated with miR-33 trigger or scr. miR-33. [locked Dz] = 200 nM, [miR-33 mimic] = 200 nM, [scr. miR-33] = 200 nM, [substrate] = 1 μM, [Mg^{2+}] = 2 mM; 37 °C for 2 h (d) or 22 h (e).

3.3.3 miR-33 triggered activation of locked DNAzyme and TNFα knockdown in macrophages

To test if endogenous miR-33 triggers activation of locked Dz, we used RAW264.7, a mouse macrophage cell line that expresses miR-33, as a model *in vitro* system. Locked Dz was transfected into RAW264.7 cells using Oligofectamine, and qRT-PCR was performed to quantify TNFα mRNA level after 24 h incubation. Note that there is a CpG motif in the catalytic core of DNAzyme sequence, which is known to stimulate Toll-like Receptor 9 (TLR9) signaling, and induce proinflammatory cytokine expression. [316, 317] To account for this background pro-inflammatory effect of the nucleic acid, an inactive Dz with the same catalytic core but with scrambled binding arms was used as the negative control. Unlocked Dz, or the Dz strand alone, was used as the positive control. Unexpectedly, the locked Dz showed a similar level of TNFα mRNA knockdown compared to the unlocked Dz, which indicated complete activation of Dz in RAW264.7 cells (Figure 3.6). We hypothesized that this result occurred due to nuclease-caused degradation of unmodified linear DNA, specifically the α', β' and β domains, leading to unlocking in RAW264.7 cells. To address this, we incorporated 2'-OMe modification in the α', β', β and γ' domains. Note that the 2'-OMe modification was only introduced at the 4 nt terminus of the 3' end of γ' domain, matching the Dz binding arm. As shown in Figure 3.7, active Dz strand alone knocked down TNFα mRNA by ~45% compared to negative control inactive Dz strand, whereas locked Dz showed only ~30% TNFα mRNA knockdown. To confirm that the mRNA knockdown by locked Dz is dependent on the toehold, we also created and transfected a locked Dz with its toehold truncated, which did not show significant TNFα knockdown. These results suggest that the 2'-OMe

modification helped reduce spontaneous activation caused by nucleases, and activation of locked Dz depends on the toehold. Our attempt to further enhance TNFα knockdown with exogenously transfected miR-33 mimics did not provide positive results (Figure 3.8). RAW264.7 cells were sequentially transfected with miR-33 mimic then locked Dz after a 24 h interval, and allowed to incubate for another 24 h. Based on the qPCR results, miR-33 level was increased by ~50 fold in miR-33 mimics transfected cells compared to control miRNA mimic transfected cells (Figure 3.8a). Surprisingly, we observed higher TNFα level in miR-33 mimics transfected cells compared to the control cells (Figure 3.8b). We thus hypothesized that the increased expression of TNFα was due to cross talk between miR-33 and the innate immune response, which elevates TNFα levels. Indeed, previous literature showed that miR-33 augments TLR signaling indirectly in macrophages by increasing cholesterol-enriched lipid raft micro-domains in which TLR complexes are assembled and activated. [257] This provides a potential explanation for why exogenously transfecting miR-33 mimic did not lead to further knockdown of TNFα by locked Dz (Figure 3.8).

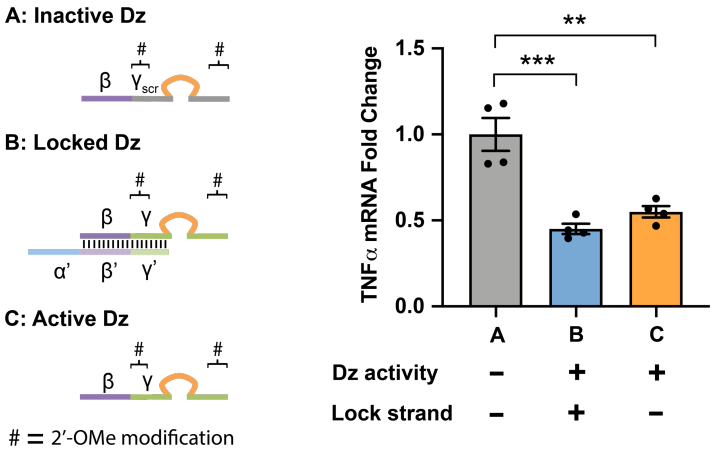

Figure 3.6 Dz locking is inefficient with unmodified toehold and branch migration domains *in vitro*.

RAW264.7 cells were transfected with inactive Dz (A), locked Dz with toehold (B) and unlocked Dz (C) using Oligofectamine and incubated for 24 h. TNFα mRNA level was quantified by qRT-PCR. Dz activity: "-" indicates Dz with scrambled Dz binding arms, "+" indicates Dz with TNFα mRNA complementary binding arms; Lock strand: "-" indicates that the Dz is not hybridized to the lock strand, "+" indicates that the Dz is hybridized to the lock strand. The error bars represent SEM of biological replicates (**p <0.01, ***p <0.001, one-way ANOVA compared to A with Tukey's multiple comparison).

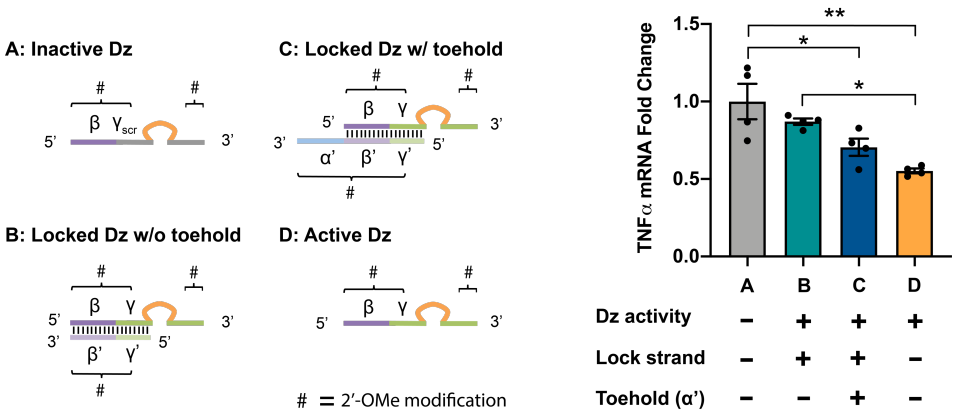

Figure 3.7 Endogenous miR-33 triggered activation of locked Dz and TNFα knockdown *in vitro*.
RAW264.7 cells were transfected with 200 nM inactive Dz (A), locked Dz without toehold (B), locked Dz with toehold (C) or active Dz (D) with Oligofectamine and incubated for 24h before RNA isolation and qRT-PCR quantification of TNFα mRNA. # indicates 2'-OMe modification. Dz activity: "-" indicates Dz with scrambled binding arms, "+" indicates Dz with TNFα mRNA complementary binding arms; Lock strand: "-" indicates that the Dz is not hybridized to a lock strand, "+" indicates that the Dz is hybridized to a lock strand; Toehold: "-" indicates the absence of toehold, "+" indicates the presence of the toehold. The error bars represent standard error of the mean (SEM) for biological replicates (*p<0.05, **p<0.01, one-way ANOVA with Tukey's multiple comparison).

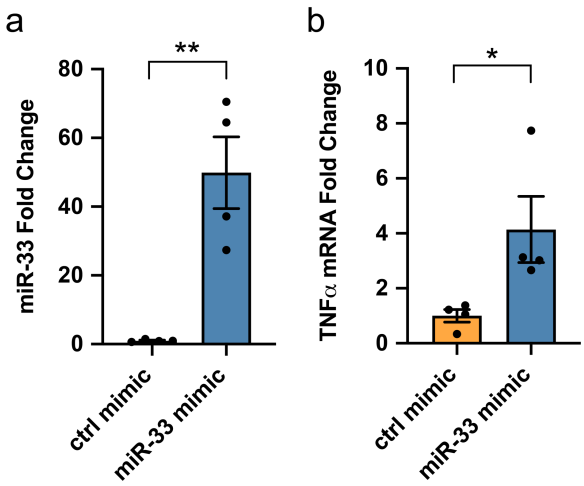

Figure 3.8 Exogenously transfected miR-33 upregulates TNFα expression.
RAW264.7 cells were transfected with 200 nM *mir*Vana™ miR-33 mimic (#4464066) or *mir*Vana™ negative ctrl mimic (#4464058) using Oligofectamine. 24 h later, cells were transfected with 200 nM locked Dz, and incubated for another 24h before RNA isolation and qRT-PCR analysis of (a) miR-33 and (b) TNFα mRNA. The error bars represent SEM for biological replicates (*p <0.05, **p <0.01, two-tailed t test).

3.3.4 Preparation and characterization of conditional DzNPs

We next sought to conjugate locked Dzs on the surface of AuNPs. Citrate-stabilized 13 nm AuNPs were prepared using published procedures. [318] AuNPs with this size was chosen because DNA-AuNP conjugates with a 13 nm AuNP core are extensively taken up by a variety of cell lines, based on our prior work [127] and studies done by Mirkin and others [129, 319]. The AuNPs were monodispersed as shown by Transmission Electron Microscopy (TEM) (Figure 3.9a), and the AuNPs also showed an absorption peak at 520 nm (Figure 3.9b). At present, there are two general methods for preparation of double stranded-DNA conjugated NPs. The first and most commonly used method employs gradual salting of AuNPs and thiolated single strand DNA (ssDNA) over many hours to maximize DNA packing and screen charge repulsion. [318] These NPs are then hybridized with complementary DNA. A more recent approach which is less commonly used utilizes freezing of thiolated ssDNA, complementary DNA and AuNPs in a single pot. [119] Based on several screening experiments, we determined that the freezing method produced the highest density of DNA duplexes per AuNP, in agreement with literature precedent. [119] Specifically, Dz strand and thiolated lock strand were frozen together with AuNPs and salted to 0.3 M NaCl right before thawing at room temperature (Figure 3.10a). [119] The resulting locked DzNPs with 11 nt α' domain and 10 nt β' domain possessed an average of 84±17 Dz strands per NP (Figure 3.10b) and a ~69% Dz strand/lock strand ratio (Figure 3.10c). Furthermore, we studied the effect of toehold length on Dz strand loading. Locked DzNPs with 7 nt toehold (α' = 7 nt, β' = 14 nt) and 4 nt toehold (α' = 4nt, β' = 17nt) gave an average of 95±17 and 117±10 Dz strands per NP and a Dz strand/lock strand ratio of 71% and 86%, respectively (Figure 3.10b,c). The increased loading of duplex DNA per

AuNPs with reduced toehold length is likely due to increased thermodynamic stability of locked Dz duplex with longer β' domain. This hypothesis is supported by the increased melting temperature (T_m) of locked DzNPs with shorter toehold length: T_m of 11 nt, 7 nt and 4 nt toehold locked DzNPs were measured to be 62.3±0.6 °C, 68.7±0.2 °C and 69.2±0.1 °C, respectively (Figure 3.10d and Figure 3.11a-c). The hydrodynamic diameters of locked DzNPs with 11 nt, 7 nt and 4 nt toehold were 72.7±3.2 nm, 82.8±14.0 nm and 88.0±4.7 nm, as measured by dynamic light scattering (DLS) based on the number distribution of their sizes (Figure 3.11d-g). The zeta potentials of locked DzNPs with 11 nt, 7 nt and 4 nt toehold were measured to be -14.6±2.8 mV, -16.8±0.5 mV and -14.1±1.2 mV, respectively, compared to -2.8±1.6 mV for citrate-stabilized AuNPs (Figure 3.11h).

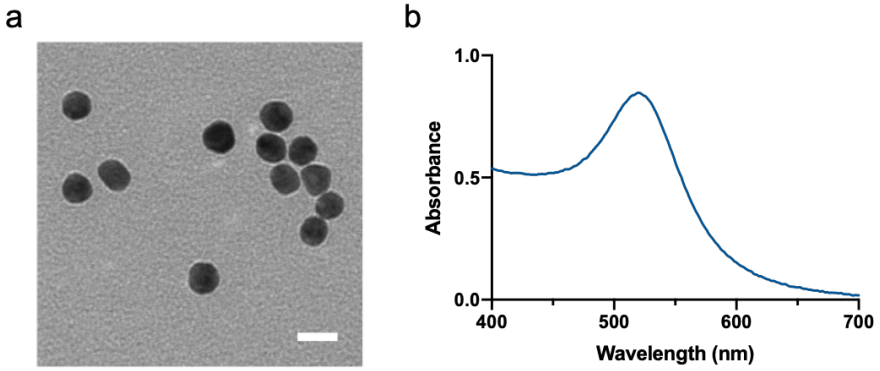

Figure 3.9 Characterization of AuNPs.
(a) Representative TEM image (scale bar=20 nm), and (b) absorption spectrum of AuNPs used in this work.

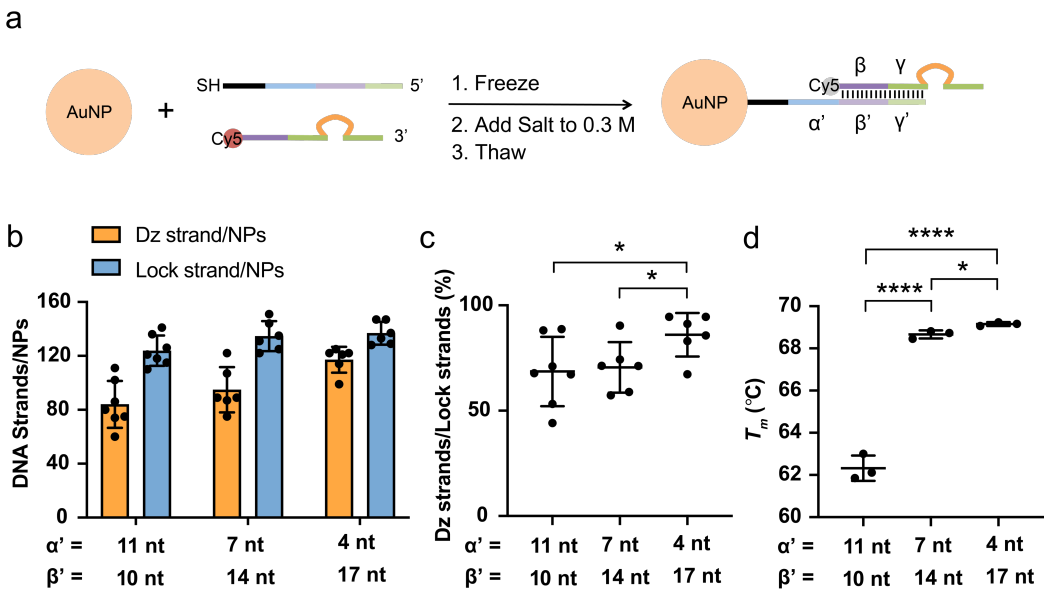

Figure 3.10 Preparation and characterization of locked DzNPs.
(a) Schematic showing preparation of conditional DzNPs by freezing of lock strand (3 μM) and Dz strand (3 μM) with AuNPs (8 nM), adding salt and thawing at room temperature. (b) Quantification of the number density of Dz strands and lock strands per AuNP. (c) Lock strands occupancy by Dz strands as a function of toehold (α') length. (d) T_m of conditional DzNPs as a function of toehold (α') length. Each data point represents an independent sample. The error bars represent standard deviation (SD) (*p<0.05, ****p<0.0001, student t-test).

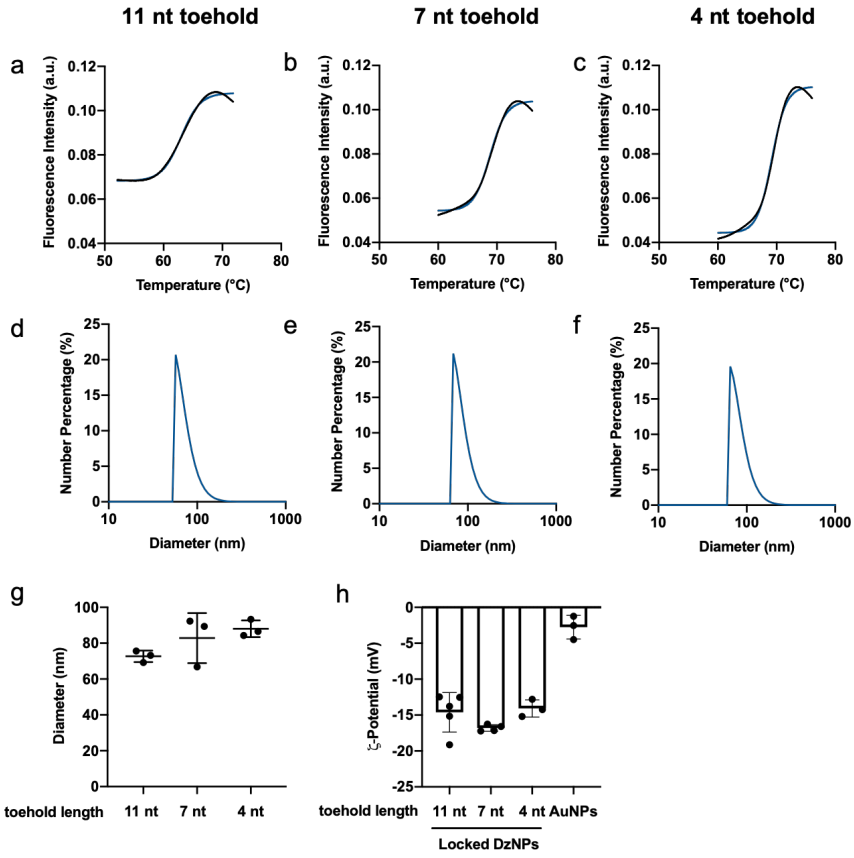

Figure 3.11 Characterization of locked DzNPs with different toehold length.
(a-c) Representative melting curves of locked DzNPs with (a) 11nt, (b) 7nt and (c) 4nt toehold. The fluorescence intensity of 5 nM Cy5-labeled locked DzNPs with different toehold length in PBS was measured with a LightCycler® 96 instrument as a function of temperature. The temperature was ramped from 45°C to 95 °C at the rate of 0.04 °C/s, and 25 measurements were performed per °C with an interval of 0.04 °C. The black lines indicate measured data, and the blue lines indicate fitted curves. T_m was determined as the temperature that generates a half-maximal fluorescence increase in the fitted curves. The data shown in Figure 4d was compiled from three independent melts collected for each locked DzNPs. (d-f) Size distribution of locked DzNPs with (d) 11nt, (e) 7nt and (f) 4nt toehold measured by dynamic light scattering (NanoPlus zeta/nano particle analyzer, Particulate Systems). (g) Hydrodynamic diameters of locked DzNPs with different toehold length. (h) ζ-potentials of locked DzNPs with different toehold length, as well as citrate-stabilized AuNPs, measured with the NanoPlus zeta/nano particle analyzer. The error bars represent SD.

The kinetics of Dz unlocking and subsequent substrate cleavage of locked DzNPs were studied using time-resolved fluorescence assays. To quantify Dz activity, the substrate was labeled with FAM and Black Hole Quencher (BHQ) at its termini. Upon cleavage, FAM fluorescence increases, thus reporting the catalytic activity of the Dz strand (Figure 3.12a). We compared locked DzNPs of two configurations, with either lock strand or Dz strand directly attached to the surface of AuNPs, by tuning the position of the thiol group. Lock strand attached locked DzNPs released Cy5-labeled Dz strands in response to miR-33 trigger, causing an increase of Cy5 fluorescence due to separation from the AuNP and dequenching of Cy5. As miR-33 trigger concentration was increased, there was a more rapid and more complete release of Dz strands, as indicated by the Cy5 signal (Figure 3.12b). This response was specific, as scr. miR-33 did not trigger the release of Dz strands (Figure 3.12b). Locked DzNPs triggered with miR-33 were catalytically active and cleaved their substrates, causing an increase of FAM fluorescence, whereas locked DzNPs alone or locked DzNPs incubated with scr. miR-33 were not able to cleave substrates (Figure 3.12c). An alternative design with the Dz strand attached to the AuNPs (Figure 3.13a) also released Cy5-labeled lock strands in the presence of miR-33 trigger (Figure 3.13b) and the NPs were also able to cleave substrates (Figure 3.13c). However, with the same concentration of locked DzNPs (0.5 nM) and miR-33 trigger (500 nM), this design exhibited a reduction in catalytic activity compared to locked strand attached DzNPs (Figure 3.13d), despite the higher loading of Dz strands per NP (Dz/NPs=126; lock strand/NPs=97). This reduction in catalytic activity, which is consistent with our prior work, [94] is likely due to the reduced activity of immobilized Dz strands compared to their soluble counterparts because of steric hindrance for substrate binding. Note that for locked DzNPs with immobilized Dz strands,

there was a substantial amount of Dz strands that were not hybridized with lock strands. However, these Dz strands exhibited negligible substrate cleavage activity. A possible explanation is that the Dz strands that were not accessible for lock strand hybridization were also not accessible for substrate binding. Since the attachment of Dz strands to the AuNPs led to reduced Dz activity, the configuration shown in Figure 3.12a is preferable to the one shown in Figure 3.13a and was chosen for *in vitro* studies.

Interestingly, we found that the lengths of the toehold domain (α') and the branch migration (β') domain controlled the toehold exchange rate in buffer. By adjusting the lengths of α' and β' domains, we were able to tune the release rate of Dz strands and cleavage rate of the substrates. 0.5 nM locked DzNPs with 11 nt, 7 nt and 4 nt toehold released about 58%, 10%, and 0.4% Dz strand after incubation with 500 nM miR-33 trigger for 2 h (Figure 3.12d). Locked DzNPs with reduced toehold length showed reduced substrate cleavage activity when incubated with the same concentration of miR-33 trigger, due to fewer released Dz strands (Figure 3.12e). Locked DzNPs with truncated toehold showed negligible substrate cleavage activity compared to inactive DzNPs control (Figure 3.12e), confirming the toehold dependency of Dz activation.

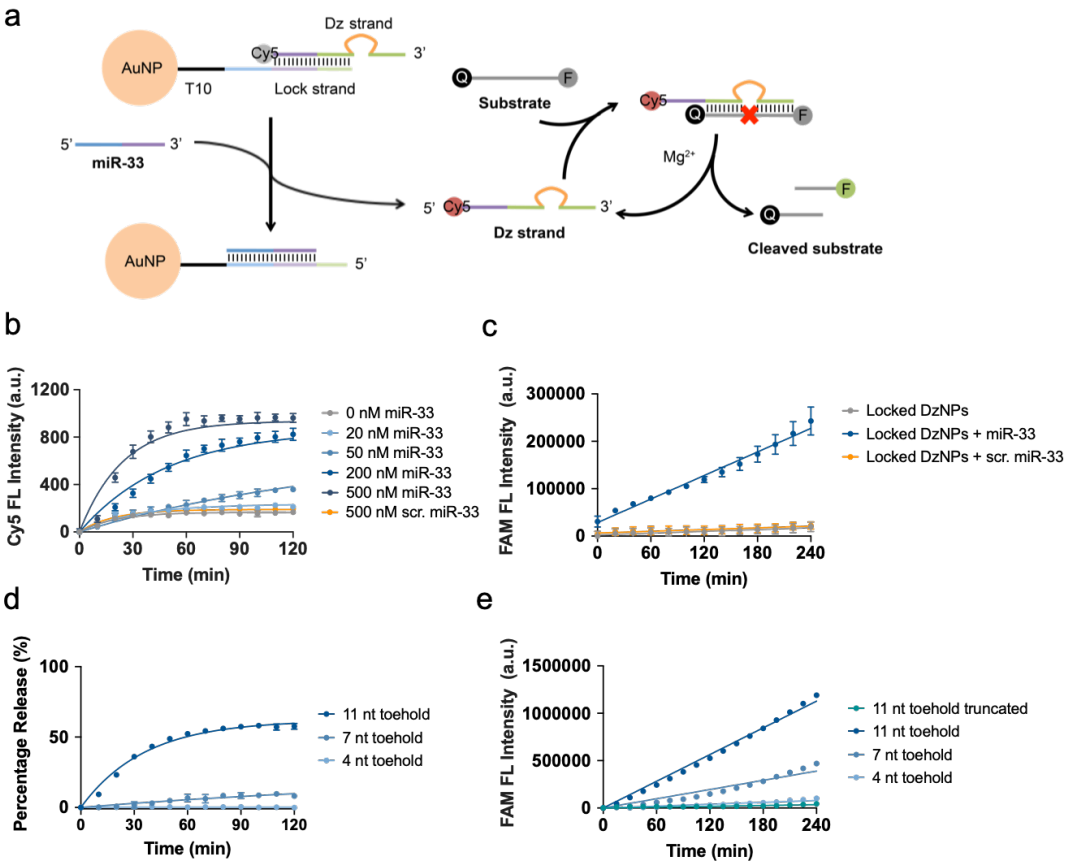

Figure 3.12 Activation of locked DzNPs in buffer.
(a) Scheme of fluorogenic assay to test release and catalytic activity of locked DzNPs. (b) Cy5 fluorescence intensity of 0.5 nM locked DzNPs incubated with different concentration (0, 5, 20, 50, 200, 500 nM) of miR-33 trigger or 500 nM scr. miR-33 at 37 °C for 2 h. The error bars represent SD (n=3). (c) 0.5 nM locked DzNPs were pre-incubated with 500 nM miR-33 trigger or scr. miR-33 at 37 °C. After 1 h incubation, 300 nM fluorogenic substrate was added and FAM fluorescence intensity was measured for 4 h. The error bars represent SD (n=3). (d) Percentage release of Dz strands from 0.5 nM AuNPs incubated with 500 nM miR-33 trigger. The error bars represent SD (n=3 for 11 nt and 7 nt toehold, n=1 for 4 nt toehold). (e) 0.5 nM locked DzNPs with different toehold lengths and Dz activity were pre-incubated with 500 nM miR-33 trigger. After 1 h incubation, 300 nM fluorogenic substrate was added and FAM fluorescence intensity was measured for 4 h. The error bars represent SD (n=3) and some of them are too small to show in the plot.

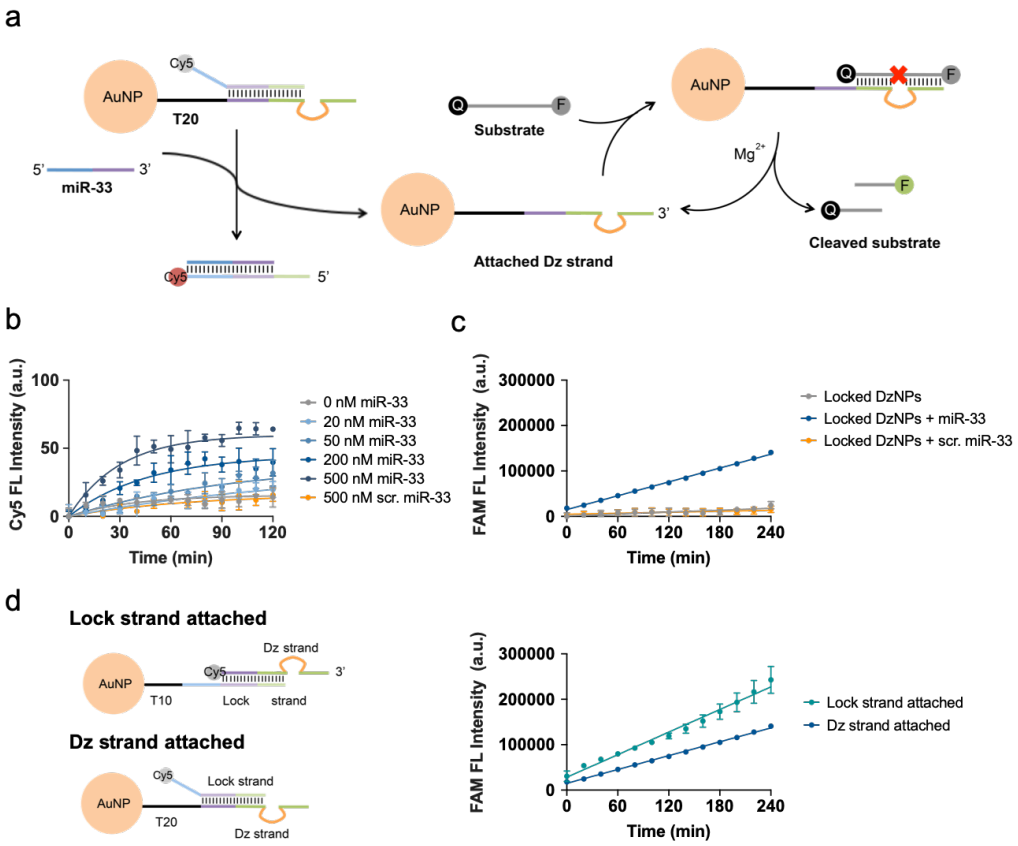

Figure 3.13 Characterization of DzNPs engineered with an anchored Dz strand. (a) Scheme for Dz strand anchored locked DzNPs. (b) Cy5 fluorescence intensity of 0.5 nM locked DzNPs incubated with different concentrations (0, 5, 20, 50, 200, 500 nM) of miR-33 trigger and 500 nM scrambled miR-33 for 2h. The Cy5 fluorescence intensity quantifies the efficiency of toehold exchange as a function of time. The error bars represent SD of three replicates. (c) 0.5 nM locked DzNPs was pre-incubated with 500 nM miR-33 trigger or scrambled miR-33. After a 1h incubation, 300 nM of fluorophore-quencher tagged substrate was added and the fluorescence of FAM was measured for 4h. (d) Comparison of activities of 0.5 nM locked DzNPs of two configurations incubated with 500 nM miR-33 trigger. The plot shows the average intensity from three replicates, and the error bar represent SD and some of them were too small to show on the plot.

3.3.5 miR-33 triggered TNFα knockdown by locked DzNPs in macrophages

The cellular uptake of locked DzNPs was assessed by fluorescence imaging of RAW264.7 cells after 1 h to 24 h incubation with 5 nM Cy5-labeled locked DzNPs (Figure

3.14a). We observed substantial internalization of NPs at the 1 h time point and further increased internalization at the 4 h time point. The time scale of uptake was consistent with previous work. [94, 132] The fluorescence intensity of the cells decreased at 16 h and 24 h time points, likely due to oxidation of degradation of Cy5 over time. The internalization of locked DzNPs was confirmed by Z-stack confocal microscopy (Figure 3.14b, c). We also investigated the effect of serum on cellular uptake of locked DzNPs. A previous study has shown that serum proteins can adsorb to DNA-AuNPs and enhance cellular uptake of G-rich DNA-AuNP but not poly-T DNA-AuNPs by THP-1 monocytes in the presence of serum. [320] Another study showed that IgG and human serum albumin adsorption lead to reduced uptake of DNA-AuNPs by THP-1 cells. [321] In addition, it has been reported that in the presence of bovine serum albumin, the cellular binding of anionic NPs is inhibited. [322] These studies suggest that the amount and type of proteins adsorbing on DNA-AuNPs influence their cellular uptake differently. To study the effect of serum on our system specifically, we incubated Cy5-labeled locked DzNPs with RAW264.7 cells for 4 h and performed flow cytometry to quantify cell-associated fluorescence. As shown in Figure 3.14d and 3.14e, cells incubated with locked DzNPs showed slightly enhanced uptake in the presence of serum.

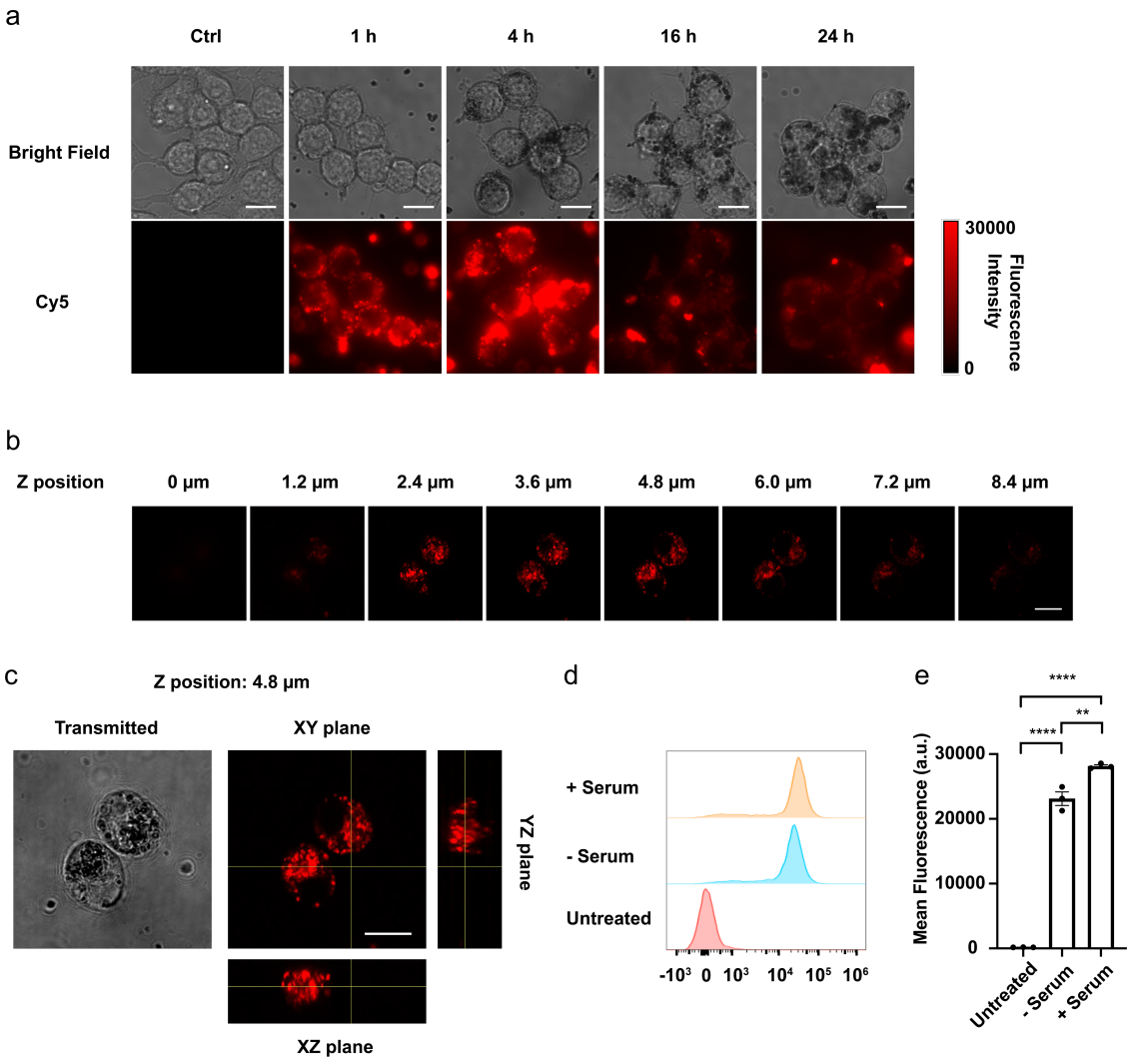

Figure 3.14 Uptake of locked DzNPs by RAW264.7 cells.
(a) 5 nM of 11nt toehold locked DzNPs (with Cy-5 labeled Dz strands) were incubated with RAW264.7 cells for 1h, 4h, 16h and 24h. Cell uptake was assessed with widefield fluorescence imaging in the Cy5 channel. Scale bar represents 10 µm. (b, c) Confocal microscopy images of RAW264.7 cells incubated for 4h with 5 nM 11nt toehold locked DzNPs (with Cy-5 labeled Dz strands). (b) Confocal images at different Z positions and (c) orthogonal view showing XY, YZ, and YZ planes when Z position was set to 4.8 µm. Scale bar represents 10 µm. (d,e) Flow cytometry analysis of RAW264.7 cells incubated for 4h with 5 nM of the 11nt toehold locked DzNPs (with Cy-5 labeled Dz strands) in the presence or absence of serum. Flow cytometry was performed to quantify DzNP uptake. (d) Representative histograms of cell-associated fluorescence and (e) mean fluorescence intensity, for untreated cells and cells that were incubated with DzNPs without (-) or with (+) serum. The error bars represent SEM for biological replicates. Each data point represents the mean fluorescence intensity of 4000 to 13000 cells in one replicate. (**p<0.01, ****p<0.0001, one-way ANOVA with Tukey's multiple comparison).

To test miR-33 triggered TNFα knockdown *in vitro*, we designed four types of conditional DzNPs (Figure 3.15a) that validate the role of the toehold and the Dz activity in mediating gene regulation. Again, to account for the background pro-inflammatory effect caused by CpG motif in the Dz catalytic core, locked inactive DzNPs were used as a negative control. These particles present an inactive Dz, which has the same 10-23 catalytic core as the active Dz but with scrambled binding arms. This locked inactive DzNPs also contained the same toehold and branch migration domains as the locked active DzNPs. In addition, locked DzNPs lacking the toehold domain and locked DzNPs a scrambled toehold domain were included as controls to further confirm the role of the toehold in triggered TNFα knockdown. These nanoparticles were incubated with RAW264.7 cells for 24 h before TNFα mRNA levels were quantified with qRT-PCR. Locked DzNPs with 11nt toehold knocked down TNFα mRNA by ~41% compared with locked inactive DzNPs control (Figure 3.15b). If the 11 nt toehold of locked DzNPs was truncated (locked DzNPs without toehold), there was a weak (~11%) but not statistically significant TNFα knockdown. The 4-fold reduction in TNFα knockdown efficacy after removing the toehold (α') domain demonstrate that the activation of gene regulation depends on toehold-mediated release of the Dz strands. Locked DzNPs with scrambled toehold also showed weak, but not significant TNFα knockdown (~23%) compared to negative control. This result may be due to a combination of nuclease-mediated unlocking of the Dz as well the binding of other endogenous transcripts to the scrambled toehold driving background activation of the Dz.

We further investigated the effect of toehold length on TNFα knockdown efficacy. We again found that TNFα mRNA knockdown was dependent on the availability of a specific toehold and also on catalytical active Dz (Figure 3.15c). In contrast to their differential activity in buffer, locked DzNPs with shorter toehold lengths did not show difference in TNFα knockdown activity (Figure 3.15c). This finding may be due to a number of factors including the continuous expression of miR-33 in cells, which may be different to the consumption of miR-33 trigger in buffer. Also, the long incubation duration *in vitro* may lead to further activation of locked DzNPs with shorter toeholds. Finally, nucleases present in cells may also accelerate the release of Dz strands. Regardless, these experiments clearly show that TNFα knockdown using conditional DzNPs and this activity requires a specific miR-33 complementary toehold along with active Dz.

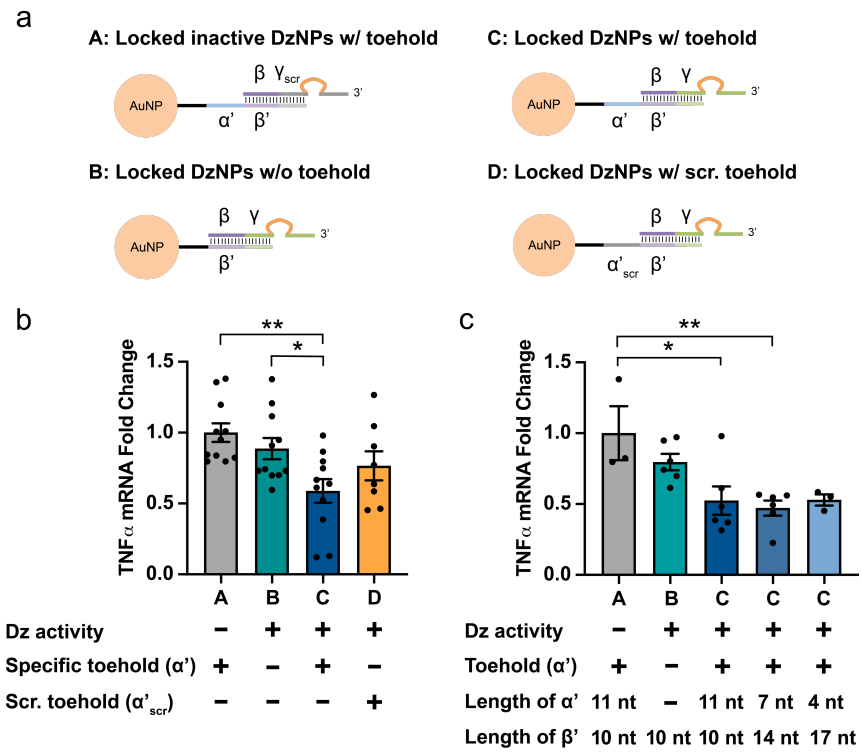

Figure 3.15 miR-33 triggered TNFα knockdown by locked DzNPs *in vitro*.
(a) Schematic description of locked inactive DzNPs w/ toehold, locked DzNPs w/o toehold, locked DzNPs w/ toehold and locked DzNPs w/ scr. toehold. (b) Effect of toehold on TNFα knockdown. RAW264.7 cells were incubated with 5 nM locked inactive DzNPs w/ toehold, locked DzNPs w/o toehold, locked DzNPs w/ toehold and locked DzNPs w/ scr. toehold for 24 h (α' = 11 nt, β' = 10 nt). TNFα mRNA was quantified by qRT-PCR. Dz activity: "-" indicates Dz with scrambled binding arms, "+" indicates Dz with TNFα mRNA complementary binding arms; Specific toehold: "-" indicates the absence of a miR-33 complementary toehold, "+" indicates the presence of a miR-33 complementary toehold; Scr. toehold: "-" indicates the absence of a scrambled toehold, "+" indicates the presence of a scrambled toehold. The error bars represent SEM of biological replicates (*p<0.05, **p<0.01, one-way ANOVA with Tukey's multiple comparison). (c) Effect of toehold length on TNFα knockdown. RAW264.7 cells were incubated with 5 nM locked inactive DzNPs w/ toehold, locked DzNPs w/o toehold, and locked DzNPs w/ 11 nt, 7 nt and 4 nt toehold for 24 h. TNFα mRNA was quantified by qRT-PCR. The error bars represent SEM of biological replicates (*p<0.05, **p<0.01, one-way ANOVA with Tukey's multiple comparison).

3.4 Methods

3.4.1 Materials

All oligonucleotides (Table 3.1), the library of DNAzymes (Table 3.2) and primers for qRT-PCR (Table 3.3) were custom synthesized by Integrated DNA Technologies (IDT), except for the fluorogenic substrate which was custom synthesized by BioSearch Technologies. 15% Mini-PROTEAN® TBE-Urea Gel was acquired from Bio-Rad. RNeasy Mini Kit, miScript II RT Kit, and miScript Primer Assays were acquired from QIAGEN. Quant-iT™ OliGreen® ssDNA Assay Kit (Invitrogen), Oligofectamine™ Transfection Regent (Invitrogen), High-Capacity cDNA Reverse Transcription Kit (Applied Biosystems), PerfeCTa SYBR Green FastMix Reaction Mixes (QuantaBio), TNFα Mouse ELISA Kit (Invitrogen), *mir*Vana™ miR-33 mimic (#4464066) and *mir*Vana™ negative ctrl mimic (#4464058) were acquired from ThermoFisher Scientific.

3.4.2 Screen for mouse TNFα DNAzyme

A library of mouse TNFα DNAzymes (Table 3.2) predicted with a customized algorithm were screened in RAW264.7 cells. 200 nM of each DNAzyme was transfected into RAW264.7 cells using Oligofectamine according to manufacturer's protocol. After 24 h incubation, the cell medium was collected for ELISA analysis of secreted TNFα. QIAzol was then added into the wells to lyse the cells and total RNA was isolated using RNeasy Mini Kit per manual. RNA was reverse transcribed using High-Capacity cDNA Reverse Transcription Kit. TNF-α mRNA level were quantified by qRT-PCR using PerfeCTa SYBR Green FastMix Reaction Mixes (QuantaBio) with 0.5 μM of custom designed primers (Table 3.3) with Applied Biosystems StepOnePlus™ real time PCR system. The

relative quantification of TNFα mRNA level was determined using ΔΔCt method with 18s mRNA as a reference.

Table 3.1 Oligonucleotide sequences used in Chapter 3

BHQ = Black Hole Quencher; FAM =6-Carboxyfluorescein; m=2'-O-Methyl modification; r=RNA base; /5AmMC6/=5' Amino Modifier C6; /3ThioMC3-D/=3' Thiol Modifier C3 SS; /5ThioMC6-D/=5' Thiol Modifier C6 SS; /3AmMO/=5' Amino Modifier

Name	**Sequence (5'→3')**
miR-33 trigger	GTG CAT TGT AGT TGC ATT GCA
Scrambled miR-33	AGC TTG ATG TTC GTT AGG CAT
7nt mDz	mGmUmG mCTC AGG CTA GCT ACA ACG AGG TmGmU mC mU
8nt mDz	mUmG mUmGC TCA GGC TAG CTA CAA CGA GGT G mUmC mUmU
9nt mDz	mCmUmG mUGC TCA GGC TAG CTA CAA CGA GGT GTmC mUmUmU
Fluorogenic substrate	FAM-AA AGA CAC CrArU GAG CAC AG-BHQ
FAM-labeled substrate	FAM-AA AGA CAC CrArU GAG CAC AG
11nt toehold Dz strand	TTG CAT TGC AmCmU mGmUG CTC AGG CTA GCT ACA ACG AGG TGT mCmUmU mU
Lock strand	GAG CAC AGT GCA ATG CAA CTA CAA TGC AC
Inactive Dz strand	TTG CAT TGC AmGmC mUmGT TAT GGG CTA GCT ACA ACG ATT CCG mUmGmC mU
11nt toehold Dz strand with modified β domain	mUmUmG mCmAmU mUmGmC mAmCmU mGmUG CTC AGG CTA GCT ACA ACG AGG TGT mCmUmU mU
Inactive Dz strand with modified β domain	mUmUmG mCmAmU mUmGmC mAmGmC mUmGT TAT GGG CTA GCT ACA ACG ATT CCG mUmGmC mU
Lock strand with modified α', β' and γ' domains	GAG CmAmC mAmGmU mGmCmA mAmUmG mCmAmA mCmUmA mCmAmA mUmGmC mAmC
11nt toehold inactive Dz strand with amine (for Cy5 labeling)	/5AmMC6/TT GCA TTG CAG CTG TTA TGG GCT AGC TAC AAC GAT TCC GTG CT

Table 3.2 Library of mouse TNFα DNAzymes screened
m=2'-O-Methyl modification; 3InvdT=3' Inverted dT

Name	Sequence (5'→3')
NS Dz	TCA AGG GAG GCT AGC TAC AAC GAA AGA AGC GG/3InvdT/
Dz110	mGmGmG mACA GAA GGC TAG CTA CAA CGA CTG CmCmU mGmG
Dz168	mUmGmU mGCT CAG GCT AGC TAC AAC GAG GTG TmCmU mUmU
Dz540	mUmGmA mAGA GAA GGC TAG CTA CAA CGA CTG GGmA mGmUmA
Dz591	mCmGmG mCTG AGG CTA GCT ACA ACG AGG TGmU mGmGmG
Dz705	mCmCmA mGGT ATA GGC TAG CTA CAA CGA GGG CTmC mAmUmA
Dz1248	mCmAmA mATA TAA AGG CTA GCT ACA ACG AAG AGmG mGmGmG
Dz1252	mGmUmG mCAA ATA GGC TAG CTA CAA CGA AAA TAG mAmGmG mG
Dz1254	mAmAmG mUGC AAA GGC TAG CTA CAA CGA ATA AAT AmGmA mGmG

Table 3.3 Primer sequences used in Chapter 3

Primer	Sequence (5'→3')
TNFα_Forward	CCAGAACATCTTGGAAATAGCTC
TNFα_Reverse	GGACCGATCACCCCGAAGT
18s_Forward	AGGAATTGACGGAAGGGCACCA
18s_Reverse	GTGCAGCCCCGGACATCTAAG

3.4.3 Optimization of mouse TNFα DNAzyme in buffer

200 nM of DNAzymes with different arm lengths and modification were incubated with 1 μM FAM-labeled substrates in 50 mM Tris-HCl supplemented with 150 mM NaCl and 2 mM $MgCl_2$ with pH 7.4. After incubated in a water bath at 37°C for 2 h 20 min, the reaction mixture was mixed with same volume of gel loading buffer and subjected to 15% Mini-PROTEAN® TBE-Urea Gel. The gel was run with 170V in 1× TBE buffer and imaged with Amersham Typhoon Biomolecular Imager using FITC channel. The

percentage cleavage of substrate was quantified by measuring intensity of substrate or product bands after background subtraction using ImageJ.

3.4.4 Labeling of Dz strands with Cy5

To label Dz strand with Cy5 for the purpose of examination of toehold exchange, 20 μL 1 mM amine modified Dz strands was mixed with 100 μg Cy5-NHS ester dissolved in 20 μL DMSO, 20 μL 1M $NaHCO_3$, 20 μL 10× PBS and 120 μL nanopure water. The mixture was allowed to react on an orbital shaker for overnight. The mixture was diluted with a 1:4 ratio with nanopure water and run through P2 gel and a Nap-25 column or High-performance liquid chromatography (HPLC) for purification.

3.4.5 Demonstration of toehold exchange and activation of locked Dz in buffer

Locked Dz was prepared by annealing the lock strand and the Cy5-labeled Dz strands at 1:1 ratio in PBS by incubating at 95°C for 5 min and 25°C for 30 min in a thermocycler. The toehold exchange between locked Dz and miR-33 trigger was examined by native PAGE gel electrophoresis. 1 μM locked Dz was incubated with 1 μM miR-33 trigger or scr. miR-33 in a water bath at 37 °C for 2 h, and then the reaction mixture was mixed with the same volume of gel loading buffer and loaded in 10% non-denaturing polyacrylamide gel. The gel was run with 110V in cold 1× TBE buffer and post stained with 1× SYBR Gold for 15 min. Then, the gel was imaged using Amersham Typhoon Biomolecular Imager with both FITC and Cy5 channel.

To demonstrate miR-33 triggered Dz activity, 200 nM locked Dz was incubated with 200 nM miR-33 trigger or scr. miR-33 as well as 1 μM FAM-labeled substrates in a water bath at 37 °C for 2 h and then the reaction mixtures were resolved with 15% Mini-PROTEAN® TBE-Urea Gel and imaged with Amersham Typhoon Biomolecular Imager, as described above. The percentage cleavage of substrates was quantified by measuring intensity of substrate or product band after background subtraction using ImageJ.

3.4.6 Synthesis of AuNPs

Citrate-stabilized 13 nm AuNPs were prepared using published procedures.[318] 200 mm solution of 1 mM hydrogen tetrachloroaurate (III) trihydrate solution was heated to a vigorous boil in a three-neck round bottom flask. Then, 20 mL of 38.8 mM sodium citrate tribasic dehydrate solution was added quickly, and the color of the mixture was changed swiftly from clear to purple to red. The reaction mixture was allowed to reflux for 15 min and cooled down to room temperature. The mixture was filtered through a 0.45 μm acetate filter to produce monodisperse AuNPs. The absorption peak of the AuNPs is at 520 nm determined by UV-vis spectrometry.

3.4.7 Preparation of locked DzNPs

Locked DzNPs were prepared using freezing method according to literature. [119] 1 mL 8 nM AuNPs was mixed with 3 μL 1mM thiol-modified lock strand (3 nmole) and 3 μL 1 mM Dz strand (3 nmole) in a 1.5 mL tube. Note that the thiol-modified lock strand

was used directly as acquired form IDT without reduction. The tube was frozen in a -30 °C freezer for at least 3 h. 176 μL salting buffer (2M NaCl in 10 mM phosphate buffer) was added into the tube right before thawing, resulting in a final NaCl concentration of 0.3 M. The mixture was allowed to thaw at room temperature. After thawing, the NPs were centrifuged down with 13000 rpm for 20 min and washed with PBS for three times. The absorbance of NPs was measured with Nanodrop at a wavelength of 520 nm. The concentration of NPs was calculated with the following equation.

$$Conc. = \frac{Abs}{2.7} \times 100\ (nM)$$

3.4.8 Quantification of lock strands and Dz strands on locked DzNPs

Cy5 labeled Dz strand was used to quantify Dz strands per NPs. A standard curve was prepared by diluting a stock of Cy-5 labeled Dz strand to 0.01, 0.1, 0.2, 0.5, 0.75 and 1 μg/mL in 1× TE buffer to a final volume of 100 μL in a 96 well plate. Locked DzNPs were diluted to 0.2, 0.4 and 0.6 nM in 1× TE buffer to a final volume of 100 μL in the same plate. The AuNPs were then dissolved by adding 1 μL of 5 M potassium cyanide (KCN) in the wells and incubating for 30 min. Fluorescence intensity (Ex/Em=630/670 nm) of each well was then measured using a Bio-Tek Cytation™ 5 Multi-Mode plate reader to determine the concentration of Dz strands per well. The number of Dz strands per NP was calculated by dividing the concentration of Dz strands by AuNP concentration.

The commercial Quant-iT™ Oligreen ssDNA Kit was used to determine the number of lock strands per NP. Locked DzNPs were washed with nanopure water for 3 times to

dehybridize Dz strands from AuNPs, remaining only lock strands. A standard curve was prepared by diluting a stock of lock strand to 0.01, 0.1, 0.2, 0.5, 0.75 and 1 μg/mL to a final volume of 100 μL in 1× TE buffer. Washed locked DzNPs were diluted to 0.2, 0.4 and 0.6 nM in 1× TE buffer. The AuNPs were then dissolved by adding 1 μL of 5 M KCN in the wells and incubating for 30 min. 100 μL of freshly prepared 1× Oligreen solution was added to each well and mixed by pipetting. Fluorescence intensity (Ex/Em=485/528 nm) of each well was then immediately measured using a Bio-Tek Cytation™ 5 Multi-Mode plate reader to determine the concentration of lock strands per well. The number of lock strands per NP was calculated by dividing the concentration of lock strands by AuNP concentration.

3.4.9 Hydrodynamic size and zeta potential measurement

The hydrodynamic size and size distribution of locked DzNPs in PBS were measured by dynamic light scattering (DLS) using a Particulate System NanoPlus zeta/nano particle analyzer with a glass cuvette at room temperature. For each measurement, the hydrodynamic sizes of 100 particles were calculated, and the peak values of their number distributions were reported. Zeta potentials of locked DzNPs in PBS and citrate-stabilized AuNPs in water were also measured using the same instrument at room temperature.

3.4.10 Release kinetics of Dz strands from locked DzNPs and determination of percentage release

90 μL PBS containing different concentrations of miR-33 trigger or scr. miR-33 in a 96 well plate was pre-incubated at 37 degree. 10 μL of 5 nM locked DzNPs was added into each well (final concentration = 0.5 nM) and mixed briefly, and the fluorescence intensity (Ex/Em=630/670 nm) was immediately measured with a Bio-Tek Cytation™ 5 Multi-Mode plate reader at 37 °C for 4 h with an interval of 5 min. To determine percentage release of Dz strands, end point fluorescence measurement after 4 h incubation at 37°C was conducted in a separate experiment to avoid inaccuracy caused by photo-bleaching in kinetic measurements. Fluorescence intensity of T10 NPs with matched quantity of Cy5-labeled Dz strand calculated with Dz strands/NPs as determined above was used as a standard to mimic 100% release.

3.4.11 miR-33 triggered activation of locked DzNPs

500 nM miR-33 trigger or scr. miR-33 trigger and 0.5 nM conditional DzNPs were mixed in 97 μL of 35 mM Tris-HCl buffer (pH=7.4) containing 150 mM NaCl and 2 mM $MgCl_2$. The mixture was pre-incubated at 37 °C for 1 h to allow activation of Dz strands. 3 μL of 10 μM fluorogenic substrate was then added to each well and mixed briefly. The fluorescence intensity (Ex/Em=485/528 nm) of each well was measured immediately with a Bio-Tek Cytation™ 5 Multi-Mode plate reader at 37°C for 4 h with an interval of 5 min.

3.4.12 Cell Culture

RAW264.7 mouse macrophages were maintained in DMEM with 4.5 mg/L glucose, containing 10% (v/v) fetal bovine serum (FBS), penicillin (100 U/mL) and streptomycin (100 mg/mL), 1500 mg/L sodium bicarbonate, 1 mM sodium pyruvate and 2 mM L-Glutamine at 37°C under a humidified atmosphere of 5% CO_2. RAW264.7 cells with passage number between 10-13 were used in the entire study. Mouse peritoneal macrophages were isolated from mouse peritoneal cavity according to published procedure. [323] Briefly, 10 mL cold medium (RPMI supplement with 10% FBS, 100 U/mL penicillin and 100 mg/mL streptomycin) was injected to the abdominal cavity of mouse and the fluid is slowly removed with syringe after carefully shaking the mouse for 5 min. Cells were spun down by centrifugation at 15000 rpm for 8 min at 4 °C. The cell pellet was resuspended in the medium and plated in 12 well plate. Unattached cells were washed away with PBS after 4 h and the adhered cells were incubated overnight for the treatment in the following day.

3.4.13 Fluorescence imaging and confocal imaging to assess cellular uptake

RAW264.7 cells were seeded in 8 well chambers on a glass slide with 5×10^4 cells per well. 5 nM of 11 nt toehold locked DzNPs (with Cy-5 labeled Dz strands) were incubated with RAW264.7 cells for 1 h or 4 h in complete medium. After washing with PBS to remove NPs that were unbound and not internalized, the cells were imaged immediately at 150× magnification with Cy5 channel on a Nikon Eclipse Ti2 microscope.

To confirm internalization of locked DzNPs inside the cells, RAW264.7 cells incubated with 5 nM 11 nt toehold locked DzNPs (with Cy-5 labeled Dz strands) for 4h, and washed with FluoroBrite DMEM medium once to remove unbound and not internalized NPs. FluoroBrite DMEM medium was then added to the wells. Z-stack confocal images were taken with a step size of 0.2 μm on a Nikon Ti Eclipse Inverted confocal microscope with a Plan Apo Lambda 60X/1.40 Oil objective.

3.4.14 Flow cytometry to investigate the effect of serum on cellular uptake

RAW264.7 cells were seeded in 12 well plate with a density of 2×10^5 cells per well the day before experiment. 5 nM Cy5-labeled locked DzNPs were added to the cells in the presence or absence of serum. After 4 h, the cells were washed with cold HBSS for 3 times, and the cells were removed from the surface using cell scrapers. The cells were pelleted by centrifugation and resuspended in HBSS for flow cytometry measurement of cell-associated fluorescence.

3.4.15 In vitro knockdown of TNFα with locked Dzs or locked DzNPs

For testing locked Dz, RAW264.7 were seeded in a 48 well plate with a density of 5×10^4 cells per well the day before transfection. 200 nM of inactive Dz, locked Dz with toehold, locked Dz without toehold and active Dz were transfected into the cells using Oligofectamine according to manufacturer's protocol. The cells were incubated for 24 h,

and RNA was isolated for quantification of TNFα mRNA using qRT-PCR as described above.

For testing locked DzNPs, RAW264.7 were seeded in a 48 well plate with a density of 5×10^4 cells per well the day before treatment. 5 nM of locked inactive DzNPs, locked DzNPs with toehold (different toehold lengths), locked DzNPs without toehold and locked DzNPs with scrambled toehold were incubated with RAW264.7 cells for 24 h in complete medium, and RNA was isolated for quantification of TNFα mRNA using qRT-PCR as described above.

3.4.16 qRT-PCR of miR-33

Cells were lysed with QIAzol reagent and total RNA was isolated with miRNeasy Mini Kit (QIAGEN) following manufacturer's protocol. RNA was reverse transcribed using miScript II RT Kit (QIAGEN). qPCR of miR-33 was conducted using miScript Primer Assays (QIAGEN) with PerfeCTa SYBR Green FastMix Reaction Mixes (QuantaBio). The relative quantification of miR-33 level was determined using ΔΔCt method with RNU6 as a reference.

3.4.17 Statistics

All statistical analysis was performed using Graphpad Prism software. Quantitative results of TNFα knockdown *in vitro* were presented as mean ± SEM. Statistical analysis

were performed by one-way analysis of variance (ANOVA) followed by post-test multiple comparison as described in the figure captions. P values of less than 0.05 were considered significant.

3.5 Conclusion, discussion and future direction

Conditional DzNPs are desirable smart gene regulation agents due to their molecularly specific response and their ability to be transiently and easily delivered into cells rather than genetically encoded. In this study, we demonstrated a proof-of-concept for conditional DzNPs that can be activated by endogenous miR-33 in macrophages. We demonstrated miR-33 triggered release and activation of conditional DzNPs in buffer and *in vitro,* and investigated the effect of configuration and toehold length on their activity. This work provides an example of intracellular toehold-mediated interaction between an endogenous transcript and "pro-drug" conditional DzNPs, which holds promise for targeted gene therapy with reduced off-target effects. Our design is modular and in principle one can engineer triggered DzNPs against a wide variety of targets that are activated using different transcriptional inputs. Targeted and cell-specific delivery of drugs, including nucleic acid-based drugs, is now part of the FDA-approved arsenal of therapies to treat multiple diseases, including breast cancer (Enhertu) and acute hepatic porphyria (Givosiran). The common targeting mechanism involves conjugating antibodies or ligands to a drug molecule, thus resulting in enhanced uptake of the molecule in the cells expressing specific surface markers. We envision that conditional DzNPs will be critical in drug targeting when a specific surface marker is absent to allow for discrimination

between cell types. The vast majority of proteins are intracellular and hence mutations in cytoplasmic proteins cannot be used in conventional drug-homing mechanisms. In this case, cell type-specific or mutated transcripts are potential triggers to switch on the activity of silenced therapeutics, including conditional DzNPs, in diseased tissues. To this end, discovery of cell type- or disease-specific transcripts and development of potent oligonucleotide therapeutics are indispensable. However, the precise mechanism of Dz activation of our system is unclear and it is possible for the triggering step to occur on the AuNP surface or alternatively, the triggering could occur after the locked duplex is released off the AuNP. Additionally, nuclease activity will also contribute to background activation of the Dz. To further address the challenge of nuclease cleavage-induced spontaneous activation of conditional oligonucleotide-NP conjugates, incorporating chemical modification of oligonucleotides may further improve robust ON/OFF behavior in physiological conditions. For this purpose, the effect of chemical modifications on toehold exchange reaction kinetics needs to be investigated in greater detail. Conditional DNA-NP conjugates also have substantial applications in programmable gene regulation. Toehold-mediated strand exchange has been demonstrated as a versatile and universal molecular programming language to construct logic gates, molecular circuits and networks. Moving forward, conditional DNA-NP conjugates could be potentially designed to bridges multiple native transcripts and synthetic gene regulatory agents via logic gates to realize more complex functions via biocomputing.

CHAPTER 4. INVESTIGATION OF THE INTRACELLULAR FATE OF DNA-AUNP CONJUGATES USING FLUORESCNECE LIFETIME IMAGING

4.1 Introduction

DNA-AuNP conjugates readily enter cells without additional carriers, which makes them ideal agents for delivering gene regulatory therapeutics. Although internalization of DNA-AuNP conjugates as well as their gene regulatory effects has been well demonstrated, the intercellular fate of DNA-AuNP is still unresolved.

Mirkin *et al*. reported that a strong colocalization of Cy5-tagged DNA-AuNP conjugates with late endosome can be observed even after 24h incubation with C166 cells, which indicates that the majority of DNA-AuNPs remain trapped in late endosome. [132] However, determination of the integrity of DNA-AuNP conjugates is challenging as AuNPs lack fluorescence, which limits analysis of DNA-AuNP colocalization. To address this problem, Mirkin *et al*. synthesized quantum dot (QD) with similar size as AuNPs covalently modified with fluorophore-tagged oligonucleotides. By studying the correlation between the fluorescence emitting by QD and the fluorophore, they investigated disassembly of the DNA-QD conjugates. The result revealed a decreased fluorescence correlation after 16h incubation. [132] The disassembly of the construct was attribute to nuclease-mediated degradation of DNA. However, as the DNA was covalently attached on the surface of QDs, the disassembly of DNA-AuNP due to breakage of Au-thiol bond was not mimicked using this DNA-QD construct. A recent study utilizes correlative

fluorescence and plasmonic imaging to monitor the dynamics of endosome trafficking and clustering of DNA-AuNPs, which indicated that DNA-AuNPs appear as single particles in the early stage of endocytosis, and gradually cluster during vesicular transport and maturation. [324] The authors reported no apparent separation of fluorescence signal from Cy3 tagged DNA and plasmonic signal from AuNPs, implying colocalization of the DNA and AuNPs. However, the colocalization of signals may result from the constrain of DNA-AuNPs in intracellular vesicles, and thus does not provide direct evidence for the integrity of DNA-AuNPs constructs. Another method to assess the integrity of DNA-AuNP conjugates is radiometric measurement of two fluorophores on the DNA with different distances to the AuNP surface, an unquenched fluorophore (F1) due to greater distance and a quenched fluorophore (F2) that is quenched due to shorter distance. Release of the DNA from AuNP surface leads to an increased fluorescence intensity ratio of F2/F1. Based on this principle, Strouse *et al*. reported that DNA release occurs within early time points after transfecting of the DNA-AuNP constructs using lipofectamine, with a half-life of 1.5h. [325] However, chemically unmodified DNA was used in this study and the effect of DNase was not evaluated. [325]

Herein, we propose to utilize a more direct metrics, fluorescence lifetime, to monitor the disassembly kinetics of DNA-AuNP conjugates intracellularly and identify the dominant factor influencing the integrity of DNA-AuNP conjugates. Our goal is to provide new insights for designing criteria of DNA-AuNP constructs as therapeutics. Unlike correlative imaging modalities, which rely on signal colocalization of the signals from the DNA and AuNP core, fluorescence lifetime depends on the local microenvironment of the fluorophore, in this case the proximity of DNA and AuNP. The use of fluorescence

lifetime-based imaging overcomes many of the limitations of intensity-based methods. For example, it precludes any erroneous measurement in fluorescence intensity due to fluorophore bleaching and degradation. Furthermore, there is no need to overlay multiple signals; hence fluorescence lifetime-based imaging also circumvents complications such as fluorophore bleed-through.

Fluorescence lifetime is the time for an excited fluorophore to return to its ground state. Fluorescence lifetime of a fluorophore depends on its molecular environment but not its concentration. Fluorescence lifetime, τ, can be measured using Time Correlated Single Photon Counting (TCSPC) [326], where the sample is excited by a high frequency pulsed laser and the arrival times of the photons is recorded and fitted into a decay function to determine the fluorescence lifetime parameters, including the amplitude-weighted ($\tau_{Av\ \ Amp}$) and intensity-weighted ($\tau_{Av\ \ Int}$) averages. [327, 328] Energy transfer from a donor to an acceptor decrease the donor fluorescence lifetime, therefore, a fluorophore tagged on DNA-AuNP shows decreased fluorescence lifetime due to surface energy transfer (SET) due to proximity quenching by the AuNP surface. By quantifying fluorescence lifetime of a fluorophore tagged on DNA that is attached on AuNPs, we hope to map the spatial and temporal dynamics of DNA-AuNP conjugate disassembly as well as the role of nuclease-caused degradation and detachment of DNA from AuNP on the disassembly of the conjugates.

4.2 Results

4.2.1 In buffer fluorescence lifetime measurements of fluorophore-tagged DNA-AuNP conjugates

After internalization of DNA-AuNP conjugate in cells, they traffic through the endolysosomal pathway. To preclude the influence of pH on the fluorescence lifetime of the fluorophore, we chose Atto647N as the fluorescence tag, whose fluorescence lifetime only shows slight changes in PBS with different pH. The fluorescence lifetime of 500 nM solution of Dz strands labeled with Atto647N in PBS with pH 7.4, 4.6 and 3.4 were measured to be 4.6 ns, 4.1 ns and 3.7 ns for $\tau_{Av\ Amp}$ and 4.7 ns, 4.2 ns and 3.9 ns for intensity-weighted lifetime $\tau_{Av\ Int}$ calculated from biexponential reconvolution fitting of the FLIM decay curve (Figure 4.1).

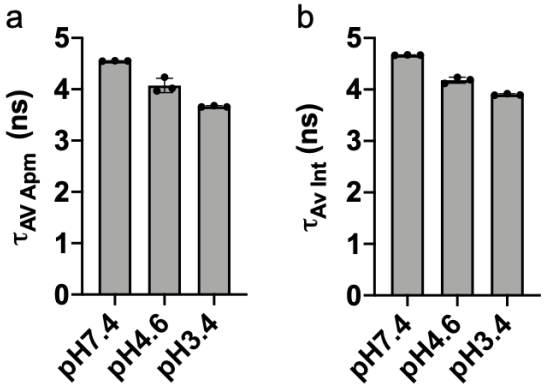

Figure 4.1 Fluorescence lifetime of Atto647N attached on Dz strand in PBS with different pH.
(a) Amplitude-weighted lifetime ($\boldsymbol{\tau_{Av\ Amp}}$) and (b) intensity-weighted lifetime ($\boldsymbol{\tau_{Av\ Int}}$) of 500 nM Dz strand-Atto647N in PBS with pH7.4, 4.6 and 3.4.

Next, we sought to demonstrate that fluorescence lifetime time measurement is able to distinct soluble DNA and DNA attached on AuNPs. Therefore, we attached thiolated T30 strands tagged with Atto647N (1:10) on AuNP and measured fluorescence lifetime of the soluble T30 strand and T30-AuNP conjugates in PBS (Figure 4.2a). As expected, Atto647N-T30-AuNPs exhibited much faster decay in FLIM decay curve and shorter fluorescence lifetime ($\tau_{Av\ \ Amp}$=0.8 ns, $\tau_{Av\ \ Int}$=1.6 ns) compared to Atto647N-T30 strand ($\tau_{Av\ \ Amp}$=3.3 ns, $\tau_{Av\ \ Int}$=3.5 ns) due to SET (Figure 4.2b,e,f).

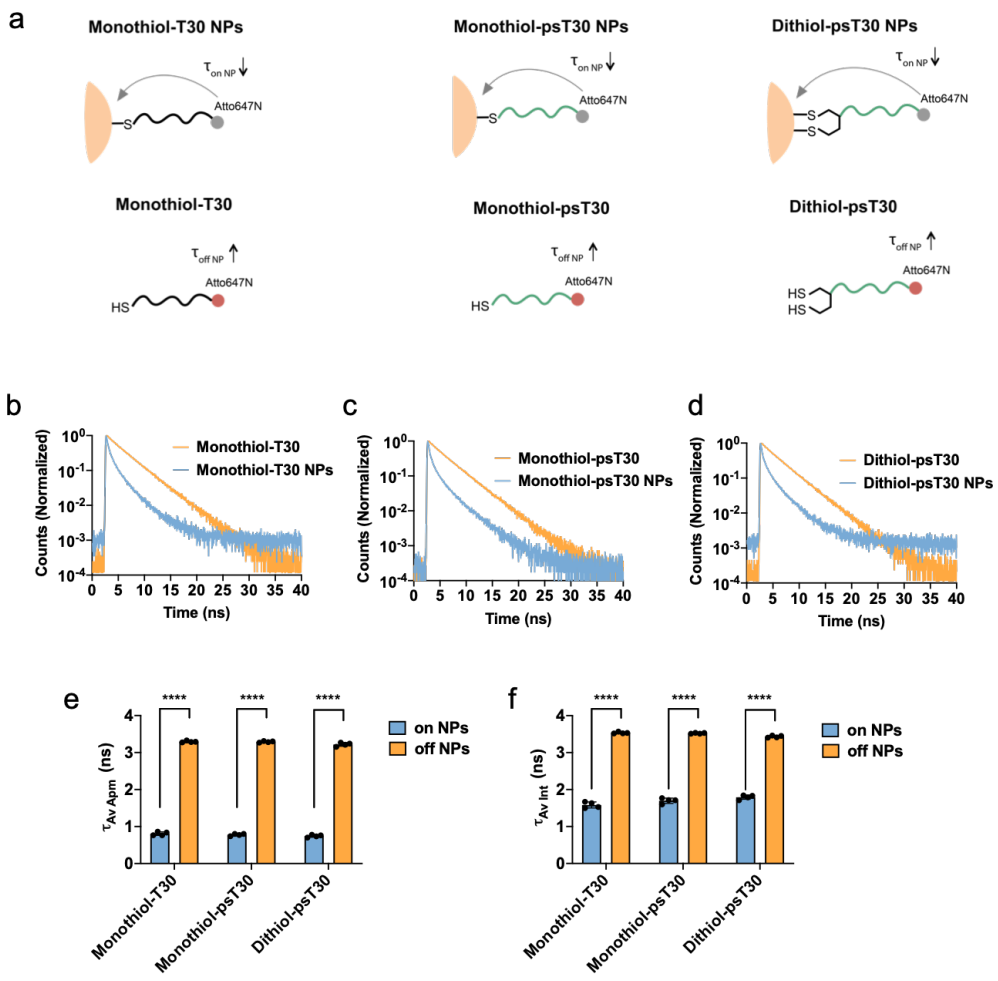

Figure 4.2 Fluorescence lifetime of Atto647N tagged on soluble DNA and on DNA-AuNP conjugates.

(a) Schemes of Atto647N tagged DNA and DNA-AuNP conjugates with or without PS modified backbone and monothiol or dithiol anchors. (b-d) FLIM decay curves, (e) $\boldsymbol{\tau_{Av\ \ Amp}}$ and (f) $\boldsymbol{\tau_{Av\ \ Int}}$ of Atto647N tagged on soluble DNA (50 nM) and on DNA-AuNP conjugates (5nM) in PBS.

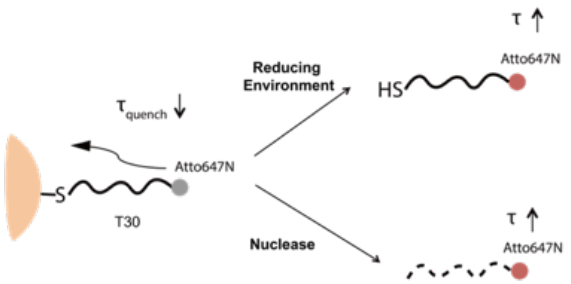

Figure 4.3 Mechanism of intracellular disassembly of DNA-AuNP conjugates.

As shown inFigure 4.3, there are potentially two mechanisms that may contribute to the disassembly of DNA-AuNP conjugates intracellularly: (1) breakage of the Au-thiol bond due to intracellular reducing agents; (2) DNA degradation caused by intracellular nucleases. To study the role of nucleases and reducing environment on the integrity of DNA-AuNP conjugates, we also prepared another two types of DNA-AuNPs conjugates (Figure 4.2a). One is T30-AuNP conjugates with PS modified backbone (monothiol-psT30-NP), which offers nuclease resistance and increases lifetime of DNA. The other one is formed by attaching DNA strands on AuNP surface with a bidentate Au-thiol bonds instead of monothiol-Au bond in addition to PS modification (dithiol-psT30-NP), to render increased stability against reducing agents as well as nuclease resistance. Previous studies have reported that DNA conjugation on AuNP surface with cyclic disulfide was more stable compared to monothiol group under the treatment of competing thiols, such as mercaptohexanol and dithiothreitol (DTT). [329] As shown in Figure 4.2c-f, monothiol-psT30-NPs and dithiol-psT30-NPs tagged with Atto647N also showed reduced fluorescence lifetime compared to their soluble linear counterparts, similar as monothiol-T30-NPs.

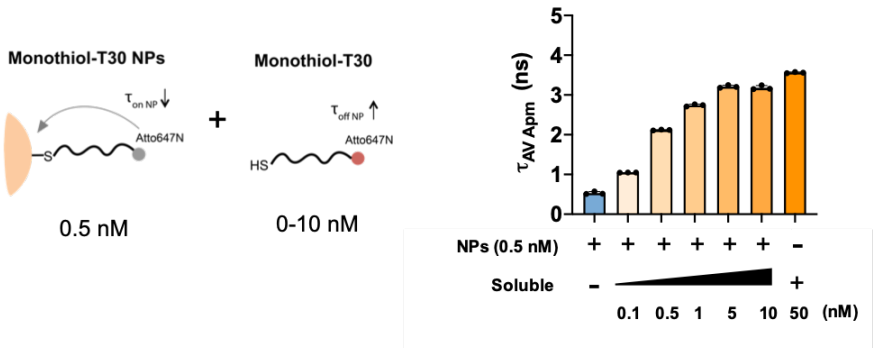

Figure 4.4 Fluorescence lifetime of Atto647N-T30-NP titrated with linear Atto647N-T30.
0.5 nM of monothiol-T30-NPs tagged with Atto647N (1:10) in PBS was titrated with 0-10 nM Atto647N-T30 strands, and fluorescence lifetime was measured.

Next, we asked if a mixture of Atto647N-tagged DNA-NP and linear DNA could produce an intermediate fluorescence lifetime. To answer the question, we measured fluorescence lifetime of mixtures of 0.5 nM monothiol-T30-NP with different concentrations of soluble T30 strands. The result showed a gradually increased fluorescence lifetime with the increase of soluble T30 strands titrated in the solution (Figure 4.4), which suggests that it is possible to monitor the gradual fluorescence lifetime increase with the detachment of the fluorophore from the AuNP. To be noticed is that there are about 5 nM Atto647N attached on 0.5 nM monothiol-T30-NP, and when the ratio of Atto647N on and off AuNP is about 1 to 1, the fluorescence lifetime of the mixture is approaching that of the soluble strand alone group (Figure 4.4).

Next, we tested the chemical stability of bidentate thiol-Au bond compared to monothiol-Au bond. We incubated 0.5 nM monothiol-psT30-NPs or dithiol-psT30-NPs with 100 μM DTT for 5 min and 30 min at 37 °C and measured fluorescence lifetime. The

fluorescence lifetime of Atto647N on both monothiol-psT30-NPs and dithiol-psT30-NPs increased after 5 min incubation, indicating the release of Atto647N-tagged DNA (Figure 4.5). However, the increase of fluorescence lifetime of dithiol-psT30-NPs group is lesser than monothiol-psT30-NPs. This confirms higher stability of bidentate thiol-Au bond compared to monothiol-Au bond (Figure 4.5). The fluorescence lifetime of both samples continued to increase after 30 min incubation, and still dithiol-psT30-NPs group exhibited shorter fluorescence lifetime than monothiol-psT30-NPs (Figure 4.5).

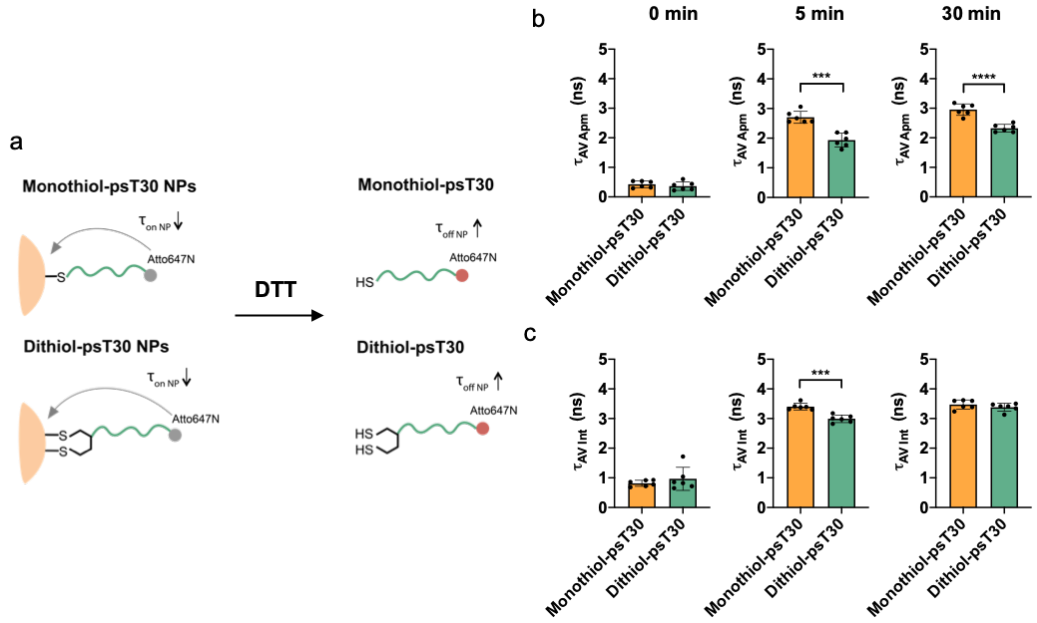

Figure 4.5 Chemical stability of monothiol- and dithiol-Au bonds against reducing agents in buffer.
(a) Scheme showing fluorescence lifetime increase of Atto647N when DNA detach from AuNPs due to reduction by DTT. (b) $\tau_{Av\ \ Amp}$ and (c) $\tau_{Av\ \ Int}$ of 0.5 nM monothiol-psT30-NPs and dithiol-psT30-NPs alone or incubated with 100 μM DTT for 5min and 30 min at 37 °C.

4.2.2 Monitoring the disassembly of DNA-AuNP conjugates in RAW264.7 cells

After characterization of the DNA-AuNP conjugates using FLIM in buffer, we moved on to monitoring their intracellular disassembly, to elucidate the role of nucleases and reducing environment on their integrity. For this purpose, we exposed RAW264.7 cells to 5 nM of the three DNA-AuNP conjugates for 5 min and then removed uninternalized and unbound AuNPs. After incubation of the cells for different period of time, FLIM imaging was conducted on the cells. We found that DNA-AuNP entered cell very rapidly and the 5 min pulsed exposure led to substantial amount of fluorescence associated within the cells (Figure 4.6a). FLIM images and calculated average fluorescence lifetimes revealed increased fluorescence lifetime over time for all three DNA-AuNP conjugates (Figure 4.6). Specifically, for cells incubated with Atto647N labeled monothiol-T30-NPs, there is detectable fluorophore dissociation within 30 min incubation and substantial amount of photons showed a long lifetime after 2h incubation (Figure 4.6a). This indicates disassociation of the fluorophore from the AuNPs at fairly early time points. This dissociation is partially attributed to nuclease degradation of the DNA. Indeed, we found that the nuclease resistant PS modified Atto647N-tagged-psT30-NP conjugates showed slower increase of fluorescence lifetime in RAW264.7 cells compared to the unmodified conjugates (Figure 4.6). However, there is no significant difference in the rate of fluorescence lifetime increase when the PS modified DNA is anchored to AuNPs via bidentate thiol-Au bond (Figure 4.6).

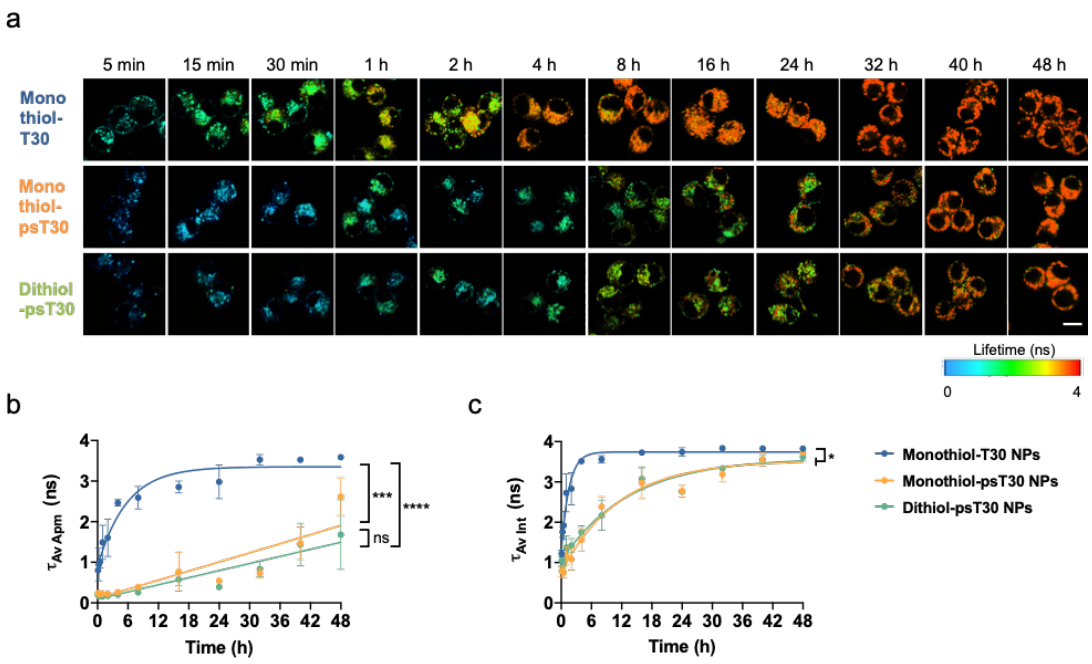

Figure 4.6 FLIM of RAW264.7 cells incubated with Atto647N labeled DNA-NP conjugates.
RAW264.7 cells were incubated with 5 nM monothiol-T30-NPs, monothiol-psT30-NPs or dithiol-T30-NPs for 5min and then unbound or uninternalized NPs were washed away. (a) FLIM images, (b) $\tau_{Av\ \ Amp}$ and (c) $\tau_{Av\ \ Int}$ of the cells after incubation for different period of time. The scale bar in (a) represents 10 μm. For (b) and (c), the mean fluorescence lifetime of 4 to 5 images was reported; the error bars represent SD. * p<0.05, *** p<0.001, **** p<0.0001, t-test.

To determine if the rapid nuclease degradation is specific to macrophage cells, we compared disassembly kinetics of monothiol-T30-NPs and monothiol-psT30-NPs in HeLa cells. As shown in Figure 4.7, there is also significant amount of NPs associated with the cells after 5 min pulsed exposure, and the fluorescence initially rises at the cell periphery in the first 1 h of incubation. In contrast to RAW264.7 cells, there is no significant difference in the rate of fluorescence lifetime increase over time between unmodified and PS modified Atto647N labeled T30-NPs. The dissociation of Atto647N from AuNPs for

monothiol-T30-NPs is much slower in HeLa cells compared to RAW264.7 cells (Figure 4.7), perhaps due to lower expression level of DNase in HeLa cells. This indicates that the intracellular half-life of DNA-AuNP is cell-type dependent.

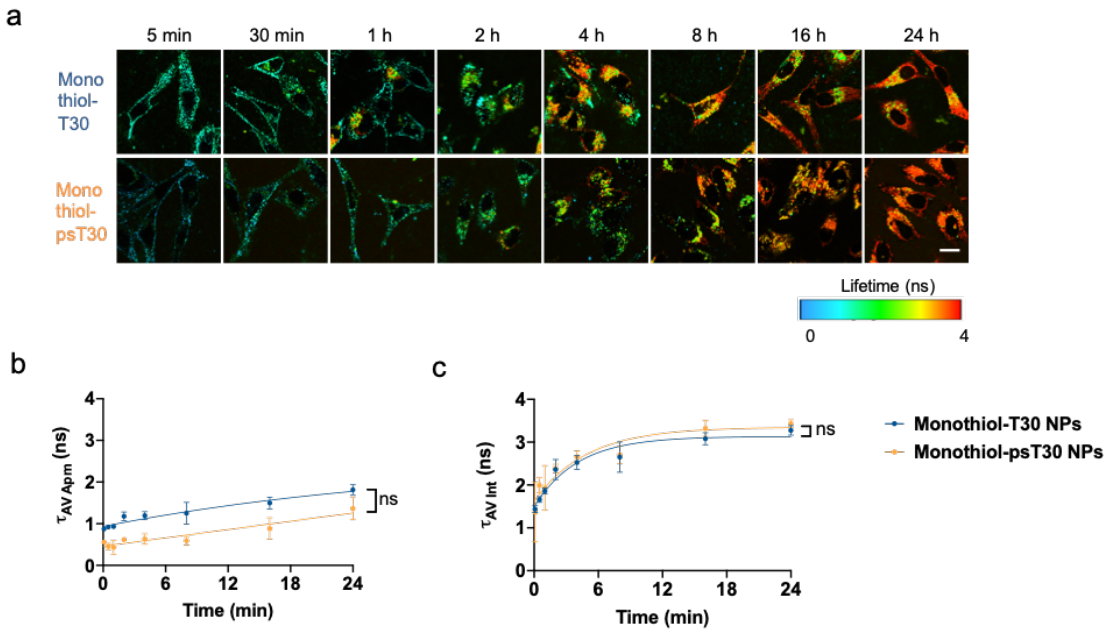

Figure 4.7 FLIM of HeLa cells incubated with Atto647N labeled DNA-NP conjugates. HeLa cells were incubated with 5 nM monothiol-T30-NPs or monothiol-psT30-NPs for 5 min and then unbound or uninternalized NPs were washed away. (a) FLIM images, (b) $\tau_{Av\ \ Amp}$ and (c) $\tau_{Av\ \ Int}$ of the cells after incubation for different period of time. The scale bar in (a) represents 10 μm. For (b) and (c), the mean fluorescence lifetime of 4 to 7 images was reported; the error bars represent SD.

4.3 Methods

4.3.1 Labelling of DNA strands with Atto647N

To label Oligonucleotides with Atto647N, 20 μL 1mM amine modified oligonucleotides was mixed with 100 μg Atto647N-NHS ester dissolved in 20 μL DMSO, 20 μL 1M $NaHCO_3$, 20 μL 10× PBS and 120 μL nanopure water. The mixture was allowed to react on an orbital shaker for overnight. The mixture was diluted with a 1:4 ratio with nanopure water and run through P2 gel and HPLC for purification.

4.3.2 Synthesize of Atto647N-labeled DNA-AuNP conjugates

13 nm AuNPs were synthesized as previously described. Oligonucleotides were conjugated on AuNPs via a freezing method described in literature. The thiol-modified oligonucleotides were used directly as acquired form IDT without reduction. Briefly, 3 nmole thiolated oligonucleotides (1:10 labeled with Atto647N) was mixed with 1 mL 8 nM AuNPs, and the mixture was frozen at -30 C for at least 2h before thawing at room temperature. The NPs were spun down at 13000 rpm for 20 min, and washed with nanopore water for 3 times, before resuspended in PBS. The concentration of AuNPs was determined by absorbance at 520 nm measured with Nanodrop.

4.3.3 FLIM imaging of NPs in buffer to determine chemical stability against competing thiols

100μL 0.5 nM Atto647N labeled NPs was incubated with 100 μM dithiothreitol (DTT) in PBS for 5 min or 30 min at 37°C in glass-bottom 96 well plates and then imaged to determine fluorescence lifetime.

4.3.4 Cell Culture

RAW264.7 mouse macrophages cell line was maintained in DMEM with 4.5 mg/L glucose, containing 10% (v/v) fetal bovine serum (FBS), penicillin (100 U/mL) and streptomycin (100 mg/mL), 1500 mg/L sodium bicarbonate, 1 mM sodium pyruvate and 2 mM L-Glutamine at 37°C under a humidified atmosphere of 5% CO_2. HeLa cells and LN229-V6R-Luc cells were maintained in DMEM containing 4.5 g/L glucose, 10% (v/v) fetal bovine serum (FBS), penicillin (100 U/mL) and streptomycin (100 mg/mL) at 37 °C under a humidified atmosphere of 5% CO_2.

4.3.5 Microscope setup

FLIM imaging were performed on a Nikon Ti Eclipse Inverted confocal microscope with a Plan Apo Lambda 60×/1.40 Oil objective. The confocal microscope is equipped with a Picoquant Laser Scanning microscope TCSPC Upgrade with SymPhoTime 64. Samples were excited with a 20 MHz pulsed 640 nm laser. The laser light was reflected using a 645 nm dichroic filter and the detector collected emitted photons that passed a 690/35 bandpass filter.

4.3.6 FLIM imaging of RAW264.7 cells and HeLa cells

RAW264.7 cells or HeLa cells were plated in glass-bottom black 96 well plates with a density of 10^4 cells/well one day before experiment. 5 nM of monothiol-T30 NPs, monothiol-psT30 NPs or dithiol-psT30 NPs (1:10 labeled with Atto647N) in normal medium were incubated with cells for 5 min. After the NPs containing medium was removed, the cells were washed with normal medium once to remove unbound and uninternalized NPs. The cells were then incubated in normal medium for different period of time from 0 h to 48 h. The cells were washed with FluoroBrite once and then 100 uL of FluoroBrite was added to the wells before the cells were imaged.

4.3.7 Image Analysis

The FLIM images were analyzed using SymphoTime (PicoQuant) software. The overall fluorescence lifetime decay trace was fitted to a biexponential function through an iterative reconvolution method. The instrument response function (IRF) for the iterative reconvolution analysis was collected using saturated Coomassie Blue and potassium Iodide (KI) solution.

4.4 Conclusion, Discussion and Future Direction

So far, the most common approaches to determine the integrity of DNA-AuNP is colocalization of the NP core and the DNA via corelative imaging and ratiometric measurements of two fluorophores on the AuNPs. Although colocalization provides proof for association of fluorescence and NPs signals, it does not directly report the physical

association of the DNA and the NPs. In addition, the endosomal trapping of the NPs and/or DNA may screw the correlation statistics towards high values. Ratiometric measurements rely on fluorescence intensity, which may be influenced by bleaching and degradation of the fluorophores. Fluorescence lifetime is an intrinsic property of a fluorophore, which is independent on their concentration, but only on the microenvironment of the fluorophore. The SET between the fluorophores tagged on the DNA and AuNP offers a direct evidence of their physical association. This study demonstrated the utility of FLIM in determination of intracellular integrity of DNA-AuNP conjugates.

Based on literature precedent by Mirkin and others, the DNA-AuNP conjugate affords some resistance to intracellular nucleases compared to linear DNA. [94, 132] DNA-NP construct leverages this effect to increase half-life of oligonucleotide therapeutics and potentially increase the effectiveness of the therapeutics. However, the effect of nuclease on the degradation of DNA-AuNP conjugates *in vitro* has not been studied. In this study, we demonstrated rapid disassembly of chemically unmodified DNA-AuNP in macrophages dominantly due to degradation of the DNA, whereas PS modification greatly reduce the rate of fluorescence lifetime increase. Noticeably, we showed that the effect of nucleases is cell-type dependent. This suggests that although DNA-AuNP can provide some degree of nuclease resistance, modification to further improve the nuclease resistance of the oligonucleotide therapeutics may still be necessary to achieve maximal potency of the drug, depending on the targeted cell type. In addition, we found that bidentate thiol-Au bond does not improve the stability of DNA-AuNP conjugates *in vitro*.

It has been reported that the DNA-AuNPs inside the cells are trapped within vesicles. 13 nm AuNP coated with DNA have been found to be mostly trapped in late

endosomes and not transported to lysosomes [132], whereas 50 nm AuNPs coated with DNA are eventually transported in lysosomes after 16 h incubation [324]. Because oligonucleotides encounter their target mRNA and execute gene regulation function in the cytosol, it is important to understand the spatial dynamics of DNA-AuNP disassembly and the endosome escape of released linear DNA and/or DNA-AuNP as a single entity. Correlation studies measuring the relationship between fluorescence lifetime of fluorophores tagged on DNA-AuNPs and staining of subcellular locations could potentially provide insights to answer these questions. For example, correlation of early endosome, late endosome and lysosome stain with the fluorescence lifetime of DNA-AuNP conjugates can determine the subcellular location of DNA-AuNP disassembly (Figure 4.8). Furthermore, to overcome endosome trapping, which is the bottle neck of intracellular delivery, strategies to enhance endosomal escape have been incorporated in the design of biologics and NPs. [330, 331] For example, endosomal escape peptides can be modified on DNA-AuNP conjugates. FLIM can potentially provide a tool to study the effect of endosomal escaping strategies on the escape of AuNP core and the DNA cargo separately by measuring the percentage of photons with long and short lifetime that are associated with cytosol.

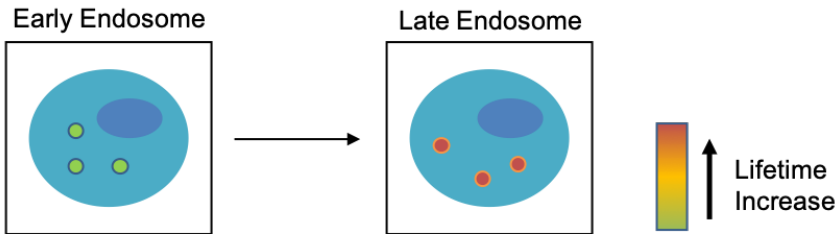

Figure 4.8 Scheme showing correlation study to determine the subcellular location of DNA-AuNP disassembly.

CHAPTER 5. DESIGN AND OPTIMIZATION OF MIR-122-INDUCIBLE HIF1α ANTISENSE

5.1 Introduction

ASOs are short synthetic nucleic acids used for modulating the cleavage of target mRNAs through Watson-Crick base pairing and recruitment of RNase H. [332] Through engaging mRNAs, ASOs indirectly regulate their protein products, including those that are otherwise "undruggable" by conventional small molecule and antibody-based drugs, which makes ASOs promising therapeutics for treating intractable diseases [333, 334]. In addition, due to the ease of tailoring ASO towards virtually any mRNA of interest, the synthesis and design of ASOs for new targets is relatively straightforward, leading to significantly shorter timeline to identifying drug candidates compared to conventional small molecule drugs and biologics [47]. Despite these advantages, clinical success of ASOs was initially hindered by their low efficacy due to nuclease susceptibility and limited cell entry. Over the past decades, with the discovery of new chemical modifications (eg. the gapmer design) [51] and conjugation strategies [335], the potency of ASOs are no longer considered as a road block for their clinical success. Currently, the grand challenge in ASO therapeutics pertains to reduce undesired adverse events by increasing the specificity of nucleic acid delivery to desired cell types or tissues. ASO are taken up by a wide variety of cell types and hence knocking down the mRNA of interest in normal tissues, perturbing homeostatsis as well as inhibiting partially complementary mRNA unrelated to the intended target.

One strategy to provide specificity for ASOs is photo-caging [140, 336], where the nucleobases are blocked with photolabile groups, such as 6-nitropiperonyloxymethyl, that reduce the binding affinity of ASOs to their targets. Upon UV-irradiation, the ASO is uncaged allowing it efficiently to bind its target mRNA. Despite the precise spatial and temporal control of ASO activity via photo-caging, this technique is limited by sub-mm tissue penetration and potential cytotoxicity of UV light. A second strategy is to formulate the nucleic acid in a lipid-nanocarrier with specific tissue tropism [107], which is a viable strategy but is unlikely to provide specificity of cell subtypes within tissues and requires high-throughput synthesis and analysis of nanomaterials *in vivo* for targeting each new tissue or cell type [337]. Another commonly adopted strategy to enhance specificity of nucleic acid drugs is ligand conjugation. For example, GalNAc conjugated siRNA targeting aminolevulinic acid synthase 1 (ALAS1) mRNA just received FDA approval to treat acute hepatic porphyria in 2019 [53], and this siRNA takes advantage of efficient liver targeting and cellular uptake due to high expression and turnover rate of its receptor (ASGPR) on hepatocytes which significantly improve its potency *in vivo* [97]. This ligand-mediated specific cellular uptake strategy can be successful when the targeted tissue or cell type displays unusually high expression levels of a surface marker. However, the majority of cellular information distinguishing cell types or diseased tissues are not easily found on the cell surface. Therefore, the receptor targeting mechanism is not universally applicable and specifically fails when a specific cell marker is absent, unknown, promiscuous for different ligands, or fails to induce ASO internalization. Hence, discovery and utilization of intracellular markers for controlling activity of ASOs may expand the targeting

competency to a broader range of clinical indications and provide better control over ASOs therapeutics.

To control oligonucleotide-mediated activity, a complementary sequence with high affinity against the oligonucleotide can be hybridized to it thus blocking its ability to bind the mRNA target and hence inhibiting its activity. This principle has been demonstrated in several examples. For instance, antagomiRs inhibit miRNA function by hybridizing to the miRNAs and blocking their binding to specific mRNA targets, and have advanced in clinical studies. [338] REVERSIR, a synthetic oligonucleotide designed to block the seeding sequence of siRNA guide strand with high affinity, can reverse the knockdown effect of siRNA *in vivo*. [180] In addition, anti-CRISPR nucleic acid inhibitors abolish Cas9 DNA cleavage activity by binding to the guide sequence, repeat sequence or protospacer adjacent motif-interaction (PAM) domain of the guide RNA. [339] These examples inspired us to consider the possibility that ASO activity could be inhibited via simple hybridization using a complementary sequence. We further hypothesized that de-hybridization of the duplex will rescue the ASO activity, which can be achieved via toehold-mediated displacement or exchange reaction [181] triggered by an endogenous nucleic acid, such as a transcript. As a proof-of-concept, we chose miRNA as the trigger transcript. miRNAs are key regulators of gene expression, with their expression dynamically changing at different developmental and disease stages as well as in specific tissues and cell types [226, 230, 232]. We specifically aimed to utilize miRNAs as endogenous triggers that could potentially control ASO activity and enable mRNA knockdown in specific cell types or tissues.

Herein, we report liver-specific miRNA (miR-122) triggered activation of a conditional HIF1α ASO. miR-122 is a highly specific miRNA exclusively expressed in hepatocytes [340] and makes up to 70% and 52% of the total hepatic miRNA pool in adult mouse and human, respectively [341]. The tissue-specificity and high abundancy make miR-122 an ideal model miRNA trigger to prove the concept of miRNA-inducible ASO. HIF1α is a master transcription factor that is related to diverse human diseases, such as cancer [342, 343] and cardiovascular diseases [277, 344]. However, since HIF1α is involved in a variety of cell activities, and plays protective roles in wound healing and repairing acute injury [295, 296] as well as regulating neoangiogenesis and tissue vascularization [297], systemically inhibiting of HIF1α may lead to side effects. Therefore, conditional regulation of HIF1α in targeted tissue or cell type could be beneficial.

In this study, we created and characterized a library of conditional ASOs. The library was tested to identify the design features that result in the most selective triggering of the ASO. We investigated the role of duplex architecture, including the length and spatial arrangement of single- and double stranded domains, thermostability and chemical composition of the conditional ASO. Then, we demonstrated activation of the conditional ASO by both a synthetic oligonucleotide mimicking miR-122 and endogenous miR-122 *in vitro*. The design principles of the locked ASO discovered herein may lay out a path for the development of specific transcript inducible ASOs to enhance specificity of oligonucleotide therapeutics.

5.2 Design of miRNA-inducible antisense oligonucleotides

As shown in Figure 5.1a, the conditional ASO was silenced due to the sequestration of the ASO sequence; however, upon triggering by the miRNA input, the conditional ASO was activated, allowing for binding and degradation of the target mRNA. The conditional ASO is a duplex formed by an extended ASO strand and a locking strand. The ASO strand was comprised of two domains: the parental ASO and a partial miRNA sequence at the 5' terminus. We termed this sequence the partial miRNA-ASO (pM-ASO) strand. The partial miRNA domain lacks the key seeding sequences (2-8 nt) of the miRNA, and hence avoids introducing the seeding sequence which may knockdown the miRNA target genes. The locking strand is composed of the complementary sequence to the entire miRNA and the parental ASO. Once hybridized, the two strands form a duplex with a single stranded toehold domain (Figure 5.1b). In the absence of the trigger miRNA, the duplex remains hybridized and the activity of the ASO is inhibited; whereas after internalization of the duplex by the trigger miRNA expressing cells, the miRNA binds to the toehold domain of the locking strand and thus initiates a competition reaction between miRNA and pM-ASO strand for the binding to the locking strand. If the binding of miRNA to the locking strand is favorable, the pM-ASO is displaced to expose and activate the ASO sequence. The activated ASO can then bind to and recruit RNase H to cleave the target mRNA (Figure 5.1c). Specifically, in the case of miR-122 inducible HIF1α ASO, the parental HIF1α ASO for conditional ASO is **EZN2968** [280], which is a 16 nt oligonucleotide with phosphorothioate (PS) backbone and locked nucleic acid (LNA) modification. miR-122-inducible HIF1α ASO is a duplex formed by the partial miR-122-EZN2968 (**pM-EZN**) strand and the locking strand.

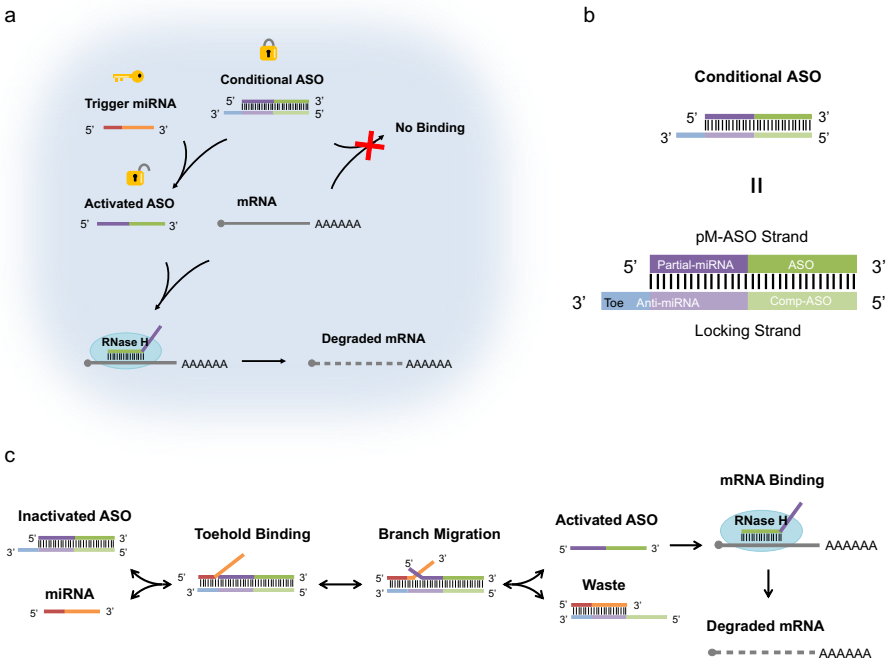

Figure 5.1 Scheme showing (a) the principle, (b) the design and (c) the triggering mechanism of conditional ASO.
(a) Conditional ASO is a duplex with the mRNA targeting ASO sequence sequestered, which abolishes its binding capability to the target mRNA. The duplex can dissociate at the presence of the trigger miRNA, exposing the mRNA targeting ASO sequence and causing the down regulation of the target mRNA. (b) Conditional ASO is formed by annealing the pM-ASO strand and the locking strand. The pM-ASO strand is the parental ASO extended with partial miRNA sequence at its 5' terminus. The locking stand comprises anti-miRNA sequence and complementary sequence of the ASO. (c) The triggering mechanism of the conditional ASO is toehold-mediated strand exchange. miRNA binds to the toehold region on the conditional ASO, which initiates branch migration and eventually leads to the dissociation of the pM-ASO strand and the locking strand. The activated pM-ASO strand can then bind to the target mRNA and cause its degradation.

5.3 Results

5.3.1 Bulge-destabilized conditional EZN2968 provides low HIF1α mRNA triggered leakage activation and high miR-122 sensitivity

To create the most selective and efficient **miR-122 inducible EZN2968** ASO, we had to optimize for 1) minimum spontaneous dissociation (leakage) of the duplex in the absence of miR-122 to keep the HIF1α ASO activity low, and 2) a high miR-122 sensitivity that leads to maximum activation of the HIF1α ASO. We predicted that due to the thermostability of the completely locked duplex, its miR-122 sensitivity would be limited (Figure 5.2). To rationally enhance sensitivity to miR-122, several nucleotides can be removed from the complementary sequence of **EZN2968**, rendering the duplex either in an end-destabilized conformation or in a bulge-destabilized conformation (Figure 5.3a). We hypothesized that bulge destabilization is advantageous over end destabilization in terms of lower leakage activation triggered by HIF1α mRNA due to the relative inaccessibility of the bulge region for mRNA binding. To test this hypothesis, we created a library of chemically unmodified duplexes with different lengths (4 nt, 7 nt and 10 nt) of the toehold (α domain) and numbers of nucleotides removed in the duplex region (length of β domain) for both conformations. The duplexes were labeled with Cy5 on the 3' termini of the **pM-EZN** strands and a quencher on the 5' termini of the locking strands. Their de-hybridization upon triggering by a HIF1α mRNA mimicking strand was quantified by measuring the increase in fluorescence intensity driven by de-quenched Cy5 (Figure 5.3b). The results showed that the percentage of displaced **pM-EZN** for all bulge-destabilized duplexes were lower than their end-destabilized counterparts, except for the ones with a 7 nt bulge and 7 nt or 10 nt toehold (Figure 5.3c). The low stability of 7 nt bulge duplexes may be attributed to lower thermodynamic stability because of the shorter double stranded domains as well as the lower stability of duplexes with larger bulge sizes, indicated by calculated ΔG (Figure 5.2b). miRNA triggered activation was also measured with a similar

assay, where the Cy5-Q-labled duplexes were incubated with miR-122 mimicking sequence (Figure 5.3d). The result showed that the miRNA triggered activation increased as the number of nucleotides removed from the duplex region (length of β domain) was increased for both conformations (Figure 5.3e), due to the reduced stability of the duplexes indicated by calculated ΔG (Figure 5.2b). Based on these results showing low HIF1α mRNA triggered leakage activation and high miR-122 sensitivity of the bulge-destabilized conformation, we decided to move forward with bulge-destabilized duplex conformation for *in vitro* screen.

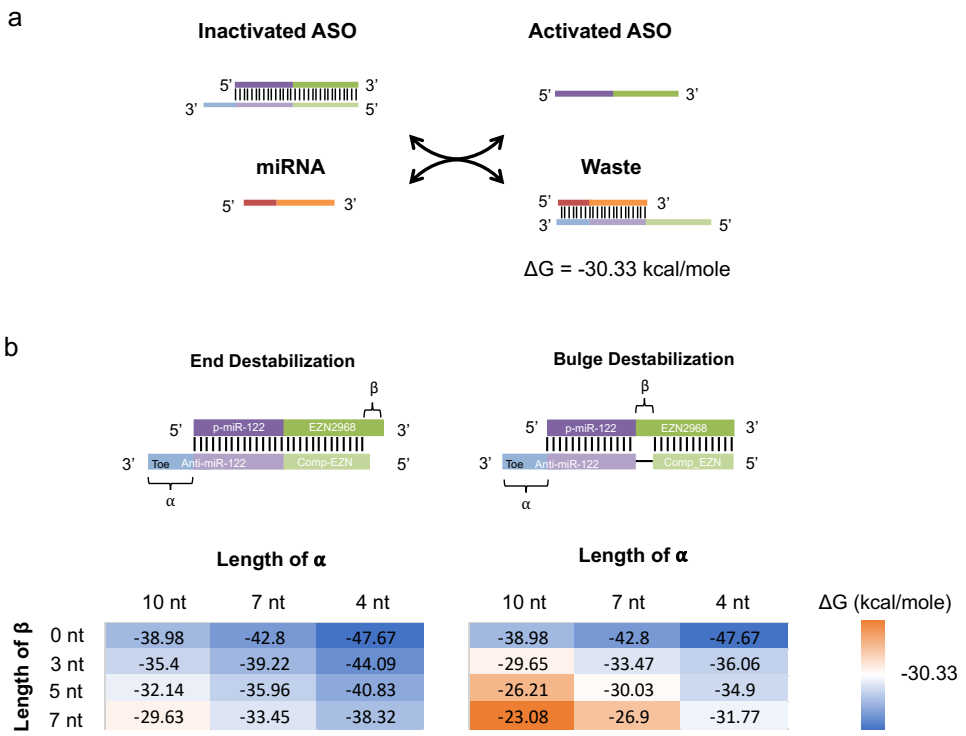

Figure 5.2 NUPACK calculation of free energy (ΔG) for conditional ASOs and miR-122/locking strand duplex at 37 °C.

(a) Scheme showing displacement of the **pM-EZN** strand by miR-122. The predicted ΔG of miR-122/locking strand duplex is -30.33 kcal/mole. (b) Predicted ΔG of conditional ASO duplexes with different length of α domain and β domain. When ΔG > -30.33 kcal/mole, the displacement reaction if favorable. These values were calculated using the default parameter set for DNA (SantaLucia, 1998) in NUPACK with 1M NaCl and 10 nM oligonucleotide concentrations at 37 °C.

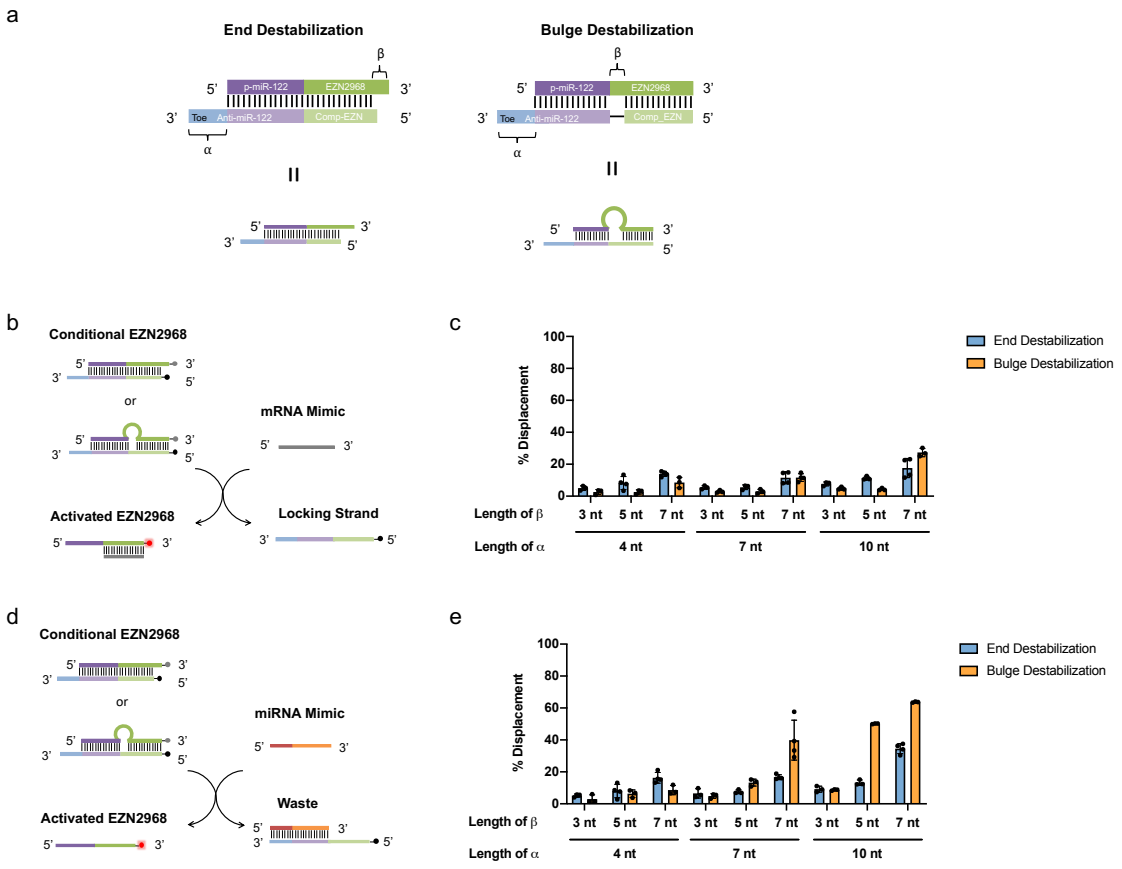

Figure 5.3 Design optimization of duplex conformation of conditional EZN2968. (a) Design of **conditional EZN2968** with end-destabilized conformation and bulge-destabilized conformation. For end destabilization, 3-7 nt on the 5' termini of the locking strand were removed. For bulge destabilization, 3-7 nt in the middle of the locking strand were removed. (b) Schematic description of in buffer assay to measure leakage activation of the **conditional EZN2968** triggered by a HIF1α mRNA mimicking sequence. Cy5 and Quencher were labeled on the **conditional EZN2968** and the locking strand separately. The annealed duplex was incubated with a HIF1α mRNA mimicking sequence (mRNA mimic), and the fluorescence increases due to dequenching caused by displacement was quantified with plate reader to calculate the percentage displacement. (c) 10 nM unmodified duplex was incubated with 100 nM HIF1α mRNA mimic at 37 °C for 2h, and fluorescence intensity of Cy5 was measured to determine the percentage of displaced and activated **pM-EZN** strands. (d) Schematic description of in buffer assay to measure miR-122 triggered activation of the **conditional EZN2968**. Cy5 and Quencher were labeled on the **conditional EZN2968** and the locking strand separately. The annealed duplex was incubated with a miR-122 mimicking sequence (miRNA mimic), and the fluorescence increases due to dequenching caused by displacement was quantified with plate reader to calculate the percentage displacement. (c) 10 nM unmodified duplex was incubated with 100 nM miRNA mimic at 37 °C for 2h, and fluorescence intensity of Cy5 was measured to determine the percentage of displaced and activated **pM-EZN** strands.

5.3.2 Extended EZN2968 knocks down HIF1α in a dose and time dependent manner

To evaluate the potency of **pM-EZN** strands composed of partial miR-122 sequences for HIF1α knockdown as a benchmark, we created **pM-EZN** with 12 nt (**pM_{12}-EZN**) or 15 nt (**pM_{15}-EZN**) extension on the 5' termini of **EZN2968** (Figure 5.4a). The **pM-EZN** strands maintained the LNA modification and the PS backbone as the parental **EZN2968**. We transfected **pM_{12}-EZN** or **pM_{15}-EZN** in U373 cells, a glioblastoma cell line that expresses high level of HIF1α and negligible level of miR-122 (Figure 5.5) and incubated for different time periods. We found that these two strands knocked down HIF1α mRNA in a dose and time dependent manner, with a remarkable nearly complete knockdown at the condition of 200 nM concentration and 48 h incubation time (Figure 5.4b). In addition, **pM_{12}-EZN** and **pM_{15}-EZN** knocked down HIF1α on both mRNA and protein level with similar potency (Figure 5.4c,d). To confirm the inhibition of HIF1α activity by **pM-EZN** strands, we transfected them in LN229-V6R-Luc cells, which stably express luciferase under the control of a promoter containing Hypoxia Response Element (HRE) to report HIF1α activity (Figure 5.4e) [345]. Since this cell line expresses low amounts of luciferase at normoxic conditions, IOX4, a prolyl-hydroxylase 2 (PHD2) inhibitor [346], was added to inhibit HIF1α degradation and induce luciferase expression. Consistent with mRNA knockdown in U373 cells, transfection of 10 nM **pM_{12}-EZN** and **pM_{15}-EZN** led to significant reduction of luciferase expression in this reporter cell line (Figure 5.4e).

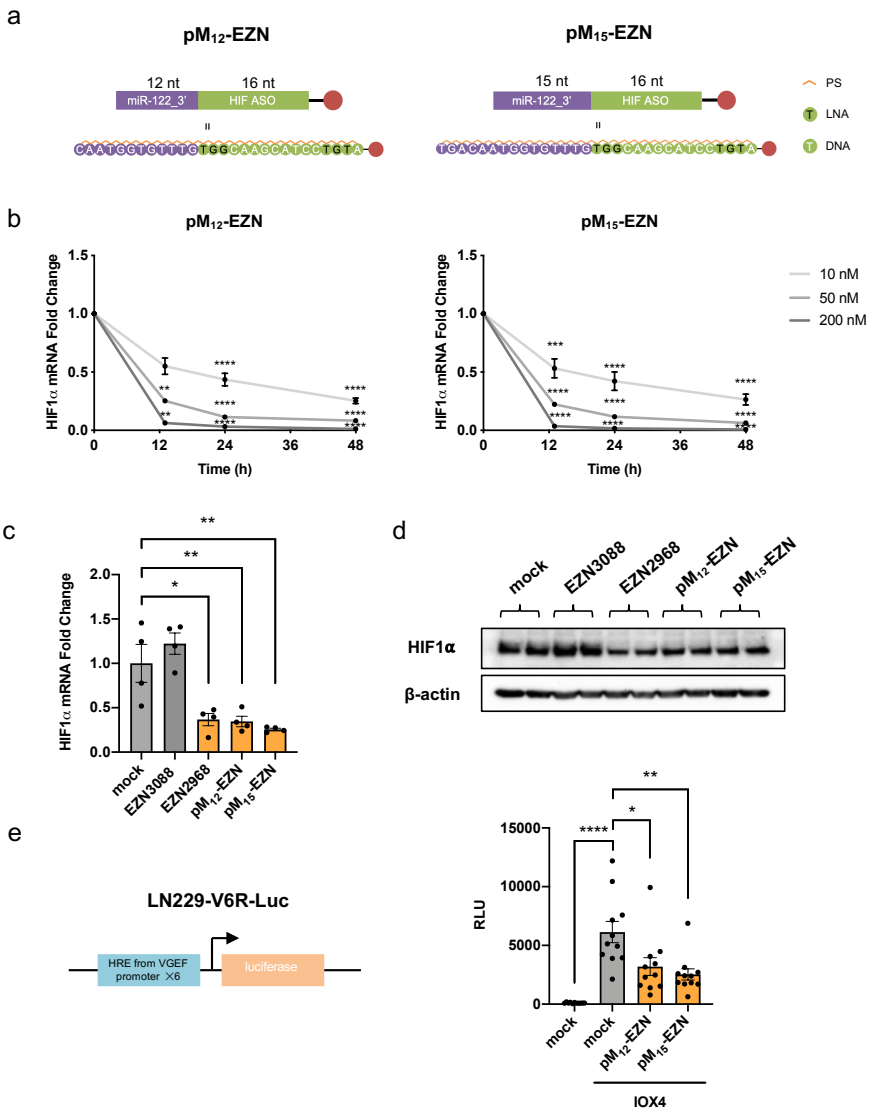

Figure 5.4 Extended EZN2968 knocks down HIF1α in a dose- and time-dependent manner in U373 cells.

(a) Design and sequences of extended EZN2968, **pM$_{12}$-EZN** and **pM$_{15}$-EZN**. (b) U373 cells were transfected with 10 nM, 50 nM and 200 nM of **pM$_{12}$-EZN** or **pM$_{15}$-EZN**, using Oligofectamine, and incubated for 13h, 24h or 48h. HIF1α mRNA levels were quantified by qPCR normalized to 18s. (c, d) U373 cells were transfected with 10 nM **EZN3088** (scrambled **EZN2968**), **EZN2968**, **pM$_{12}$-EZN** and **pM$_{15}$-EZN**, and incubated for 24h. Comparison of HIF1α mRNA (c) and protein (d) knockdown efficacy of **pM$_{12}$-EZN**, **pM$_{15}$-EZN** and their parental HIF1α ASO **EZN2968**. (e) LN229-V6R-Luc cells were transfected with 10 nM **pM$_{12}$-EZN** and **pM$_{15}$-EZN** using Oligofectamine. After 4h, 20 μM of IOX4 was added in to each well. After incubation for another 20h, luciferase assay was conducted to quantify HIF1α activity. The error bars represent SEM. ** p<0.01, *** p<0.001, **** p<0.0001, one-way ANOVA with Tukey's multiple comparison.

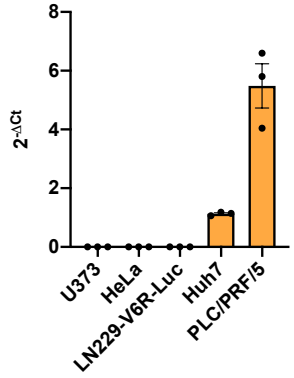

Figure 5.5 miR-122 expression levels in different cell lines.
RNA was isolated from each cell line using miRNeasy Mini Kit (QIAGEN), and reverse-transcribed using miScript II RT Kit (QIAGEN). miR-122 levels were quantified by qPCR with RNU6 as a reference. $\Delta Ct = Ct_{miR\text{-}122} - Ct_{RNU6.}$ The error bars represent SEM.

5.3.3 Screening for conditional EZN2968 with minimum spontaneous leakage

To investigate the effect of chemical modification, bulge size and toehold length on the efficacy of locking strand in terms of spontaneous leakage of HIF1α knockdown activity, we created a library of 12 **conditional EZN2968** by annealing **pM_{12}-EZN** or **pM_{15}-EZN** with 6 different locking strands (**B_0**, **B_3**, **B_5**, **B_0***, **B_3***, and **B_5***) at a 1:1 ratio in PBS. The locking strands are named based on the size of the bulge when hybridized to **pM-EZN** strand and the chemical modification. For example, **B_0** is the unmodified locking strand that does not generate a bulge when hybridized to **pM-EZN** strands; whereas **B_3*** represents the modified locking strand forming a 3 nt bulge duplex when hybridized to **pM-EZN** strands. Because PS modification reduces affinity for complementary nucleic acid by ~0.5 °C per incorporation [74], LNA modification was also incorporated in the locking strands to compensate for and maintain the thermodynamic stability of the duplex,

so that it displays a similar melting temperature (T_m) compared to its unmodified counterpart (Figure 5.6a). The resulting duplex library included permutations with a bulge size of 0 nt, 3 nt or 5 nt, a toehold length of 7 nt or 10 nt, and chemically modified (PS/LNA) or unmodified locking strands (Figure 5.6a). The duplexes are termed based on the toehold length and bulge size of the duplex. For example, the duplex formed by **pM_{12}-EZN** and **B_3*** has a 10 nt toehold and a 3nt bulge, therefore it is named as **$T_{10}B_3$***.

Transfection experiments in HeLa cells showed that PS/LNA chemical modification of the locking strand was critical for maintaining the ASO in the inactive state. We performed these experiments in HeLa cells because they do not express miR-122 (Figure 5.5). As a result, all the unmodified locking strands **B_0, B_3**, and **B_5** failed to inhibit ASO activity as measured by qRT-PCR and using the luciferase reporter cell line (Figure 5.6b,c). Importantly, incorporating locking strands with the PS and LNA modifications showed substantial improvement, resulting in dampened knockdown of HIF1α as measured by qRT-PCR and the luciferase reporter (Figure 5.6b,c). Given that the T_m of **B_0** and **B_0*** against the **pM-EZN** strands are similar, this indicates that the differential response is not driven by thermodynamic difference between the conventional nucleobases and the PS/LNA nucleic acids. We hypothesized that the failure in locking efficacy by unmodified locking strands was due to their nuclease susceptibility, which leads to degradation of the locking strands and the spontaneous activation of the **pM-EZN** ASO. To test this predication, we transfected HeLa cells with **pM_{15}-EZN** duplexes labeled with Cy5 and quencher pair and measured the cell-associated fluorescence by flow cytometry (Figure 5.6d,e). As expected, cells transfected with **pM_{15}-EZN** duplexes with unmodified locking strands (**T_7B_0**, **T_7B_3**, **T_7B_5**) resulted in similar and even slightly higher levels of

fluorescence intensity compared to single-stranded **pM$_{15}$-EZN** alone transfected cells, indicating complete dissociation of the locking strand and **pM$_{15}$-EZN** strand (Figure 5.6d,e). The slightly higher level of fluorescence intensity was consistent with the higher HIF1α knockdown efficacy by the duplexes with unmodified locking strands compared to **pM$_{15}$-EZN** only group in Figure 5.6b,c. This may be due to higher transfection efficiency of double stranded DNA compared to single stranded DNA in HeLa cells. In contrast, **pM$_{15}$-EZN** duplexes with modified locking strands (**T$_7$B$_0$***, **T$_7$B$_3$***, **T$_7$B$_5$***) resulted in reduced fluorescence intensity compare to the **pM$_{15}$-EZN** only group, showing that the duplexes remain primarily locked (hybridized) 24 h after transfection.

Furthermore, increasing bulge size decreases the thermodynamic stability of the duplex as measured by T_m (Figure 5.6a) and caused the reduction of ASO inactivation (Figure 5.6b,c). **T$_7$B$_3$*** did not knockdown HIF1α, whereas **T$_{10}$B$_3$*** knockdown HIF1α significantly, indicating that the length of toehold and branch migration domain also plays an important role in the spontaneous leakage. Inhibition of **EZN2968**-mediated HIF1α knockdown by chemically modified locking strands was also validated in U373 cells by both qRT-PCR and Western Blot analysis (Figure 5.7). We chose to move forward using the **T$_{10}$B$_0$***, **T$_7$B$_0$*** and **T$_7$B$_3$*** duplexes, whose parameters resulted in low spontaneous activation, for testing miR-122 induced HIF1α knockdown.

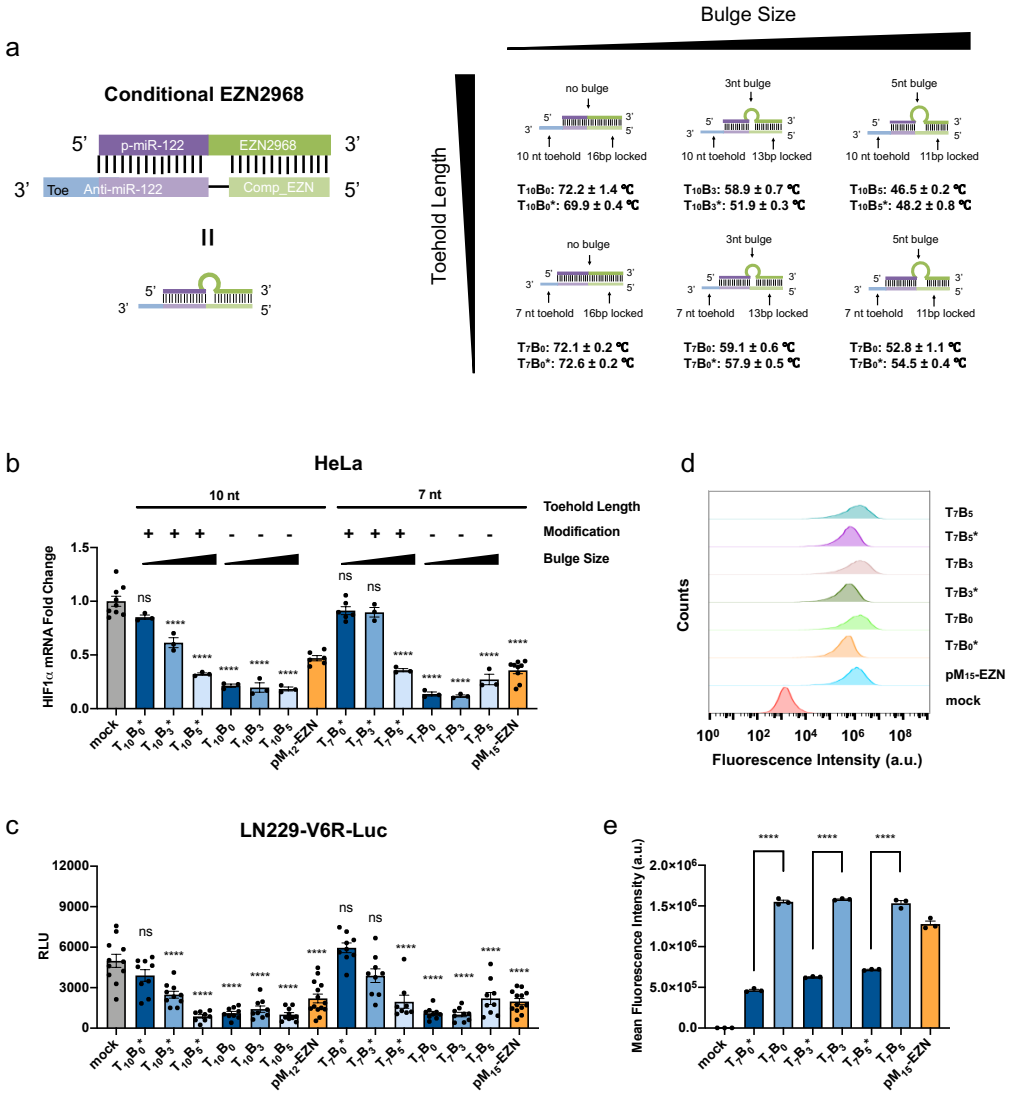

Figure 5.6 Screening for conditional EZN2968 with minimum spontaneous activation. (a) Structure and chemistry of **conditional EZN2968**. A **conditional EZN2968** is composed of a **pM-EZN** strand and a locking strand. By tuning the length of the two strands, the duplexes with different toehold lengths and bulge sizes were created. Chemically modified (annotated with "*") and unmodified locking strands were also compared to assess the role of nucleases in competence of the locking strand to inhibit **EZN2968** activity. (b) HeLa cells were transfected with 10 nM of each duplexes and incubated for 24h. HIF1α mRNA levels were quantified by qPCR normalized to 18s. (c) LN229-V6R-Luc cells were transfected with 10 nM of each duplexes and incubated for 4h. 20 μM IOX4 was added in each well and incubated for another 20h before luciferase assay was conducted to assess HIF1α activity. (d, e) Histogram (d) and mean fluorescence intensity (e) of HeLa cells were transfected with 10 nM Cy5-Quencher labeled duplexes and incubated for 24h, quantified by flow cytometry. The error bars represent SEM. ** p<0.01, *** p<0.001, **** p<0.0001, one-way ANOVA with Tukey's multiple comparison.

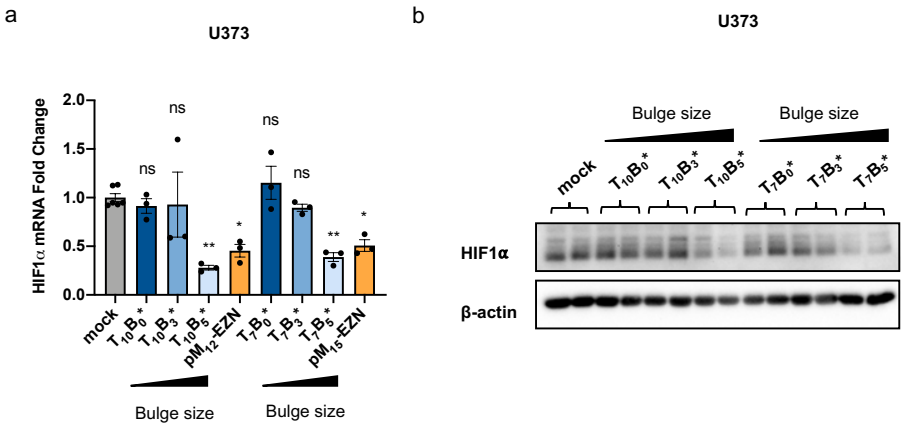

Figure 5.7 Spontaneous activation of conditional EZN2968 in U373 cells.
U373 cells were transfected with 10 nM **conditional EZN2968** using Oligofectamine and incubated for 24h. (a) HIF1α mRNA levels were quantified by qPCR normalized to 18s. The error bars represent SEM. * $p<0.05$, ** $p<0.01$, one-way ANOVA with Tukey's multiple comparison to mock transfected group. (b) Western blot of HIF1α protein with β-actin as a house-keep gene.

5.3.4 Synthetic miR-122 mimic triggers activation of conditional EZN2968 in vitro

Then we moved forward to test if **conditional EZN2968** could be activated *in vitro* by exogenously transfected miR-122 mimic. For this purpose, the duplexes were co-transfected with a synthetic miR-122 mimicking sequence (miR-122 mimic) in U373 cells. To minimize the complexity of the experiment, we prepared the transfection mixture of the **conditional EZN2968** duplex (**$T_{10}B_0$***, **T_7B_0*** or **T_7B_3***) and miR-122 mimic separately with Oligofectamine and added them to cells simultaneously. After 24 h incubation, 10 nM **T_7B_3*** alone did not show significant down regulation of HIF1α mRNA, whereas 10 nM **T_7B_3*** co-transfected with 500 nM miR-122 mimics down regulated HIF1α mRNA by ~50% (Figure 5.8a). In contrast, **$T_{10}B_0$***and **T_7B_0***, which have no bulge and higher

thermodynamic stability, did not knockdown HIF1α mRNA in this condition (Figure 5.8a). These results confirmed our initial hypothesis that completely locked duplexes without bulge render low miR-122 sensitivity, and the destabilization of the duplex is necessary for enhancing miR-122 sensitivity. Co-transfection of **T_7B_3*** and miR-122 mimic was also able to knockdown HIF1α protein level in U373 cells after 24 h incubation (Figure 5.8b,c). It should be noted that when extending incubation time to 48h, **T_7B_3*** alone group started to show more spontaneous knockdown of HIF1α mRNA, and **$T_{10}B_0$***and **T_7B_0*** co-transfected with miR-122 showed significant miR-122-triggered activation (Figure 5.9). For both 24 h and 48 h incubation, **$T_{10}B_0$*** showed slightly more knockdown of HIF1α mRNA when co-transfected with miR-122 mimic compared to **T_7B_0***, due to lower thermostability.

The activation of **T_7B_3*** is dependent on the dose of miR-122 mimics, indicated by decreased HIF1α mRNA level with increased miR-122 mimic concentration co-transfected (Figure 5.8d). Only when co-transfected with miR-122 mimics above 100 nM, **T_7B_3*** showed significant knockdown of HIF1α (Figure 5.8d). In order to confirm the mechanism of toehold-mediated strand displacement, we created a **T_7B_3*** with its toehold domain truncated. After co-transfection with miR-122 mimics, **T_7B_3*** without the toehold only showed slight knockdown of HIF1α mRNA, in contrast to **T_7B_3*** with the toehold (Figure 5.8e). This knockdown is probably caused by displacement that is not mediated by the toehold. In addition, we co-transfected **T_7B_3*** with miR-122 mimic or a miR-122 sequence with the toehold-binding domain (1-7 nt from 5' end) scrambled, and we found that the scr. 1-7nt miR-122 did not trigger significant HIF1α knockdown (Figure 5.8f). These results indicated that toehold binding process facilitated the activation of the **conditional EZN2968**, both thermodynamically and kinetically.

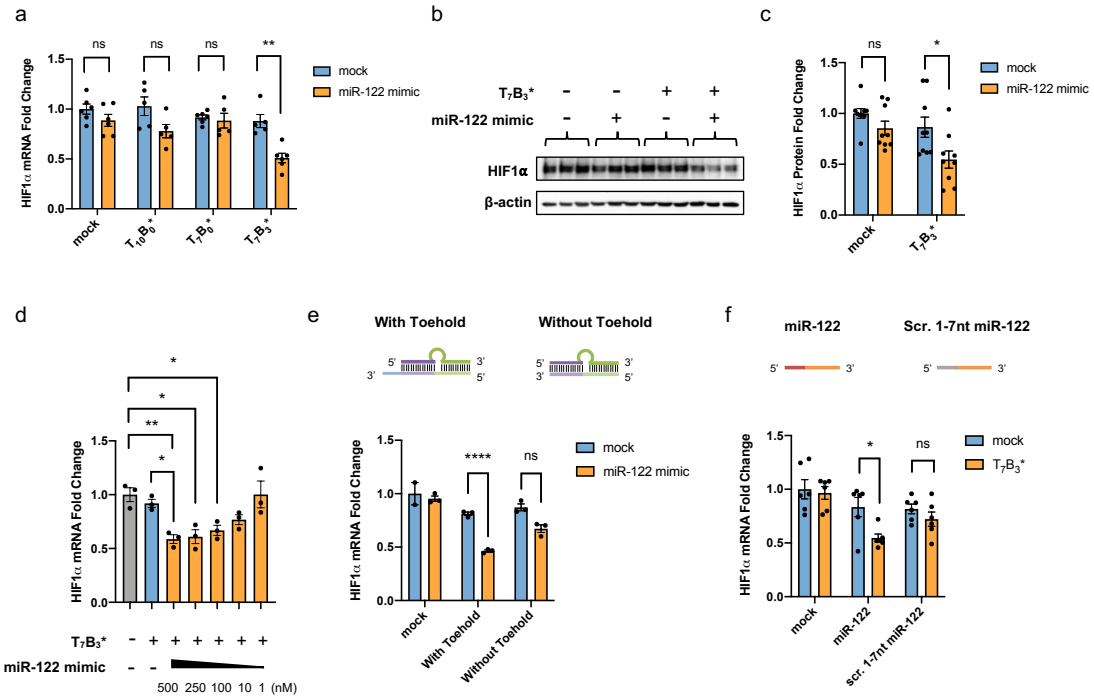

Figure 5.8 Activation of conditional EZN2968 triggered by exogenous transfected miR-122 mimic.

(a) U373 cells were co-transfected with 10 nM **$T_{10}B_0$***, **T_7B_0*** or **T_7B_3*** and 500 nM miR-122 mimic. After 24h incubation, HIF1α mRNA levels were quantified by qPCR normalized to 18s. The error bars represent SEM. * p<0.05, ** p<0.01, t-test. (b, c) U373 cells were co-transfected with 10 nM **T_7B_3*** and 500 nM miR-122 mimic and incubated for 24h incubation. The cells were then lysed and HIF1α protein was quantified by western blot. * p<0.05, t-test. (d) U373 cells were co-transfected with 10 nM **T_7B_3*** and different concentrations of miR-122 mimic. After 24h incubation, HIF1α mRNA levels were quantified by qPCR normalized to 18s. The error bars represent SEM. * p<0.05, ** p<0.01, one-way ANOVA with Tukey's multiple comparison. (e) U373 cells were co-transfected with 10 nM **T_7B_3*** with toehold or without toehold and 500 nM miR-122 mimic. After 24h incubation, HIF1α mRNA levels were quantified by qPCR normalized to 18s. The error bars represent SEM. **** p<0.0001, t-test. (**f**) U373 cells were co-transfected with 10 nM **T_7B_3*** and 100 nM miR-122 mimic or scr. 1-7nt miR-122. After 24h incubation, HIF1α mRNA levels were quantified by qPCR normalized to 18s. The error bars represent SEM. * p<0.05, t-test.

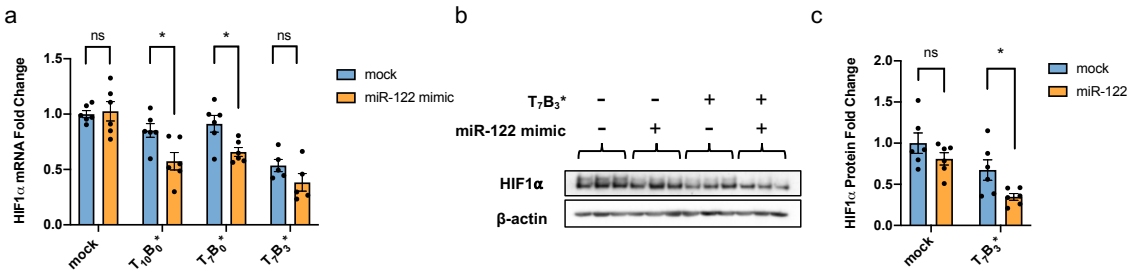

Figure 5.9 Activation of conditional EZN2968 triggered by exogenous transfected miR-122 mimic after 48h incubation.
(a) U373 cells were co-transfected with 10 nM **$T_{10}B_0$***, **T_7B_0*** or **T_7B_3*** and 500 nM miR-122 mimic. After 48h incubation, HIF1α mRNA levels were quantified by qPCR normalized to 18s. The error bars represent SEM. * $p<0.05$, t-test. (b,c) U373 cells were co-transfected with 10 nM **T_7B_3*** and 100 nM miR-122 mimic and incubated for 48h incubation. The cells were then lysed and HIF1α protein was quantified by western blot.

5.3.5 Activation of conditional EZN2968 is specific to miR-122

In order to test specificity of **conditional EZN2968** activation in response to miR-122 sequence, we used two scrambled sequences: one is completely scrambled miR-122 (scr. miR-122), the other one is scr. 1-7nt miR-122. The three miRNA sequences were co-transfected with conditional ASO **T_7B_3*** in U373 cells. The **T_7B_3*** is labelled with Cy5 on the 3' end of the **pM_{15}-EZN** strand and quencher on the 5' end of the **B_3*** strand (Figure 5.10a). After 24h incubation, the cell-associated fluorescence was measured using flow cytometry. The result showed that the fluorescence of U373 cells co-transfected with **T_7B_3*** and miR-122 mimic showed the largest increase compared to **T_7B_3*** alone transfected cells, whereas U373 cells co-transfected with **T_7B_3*** and scr. miR-122 or scr. 1-7 nt miR-122 showed only slight fluorescence increase (Figure 5.10b,c).

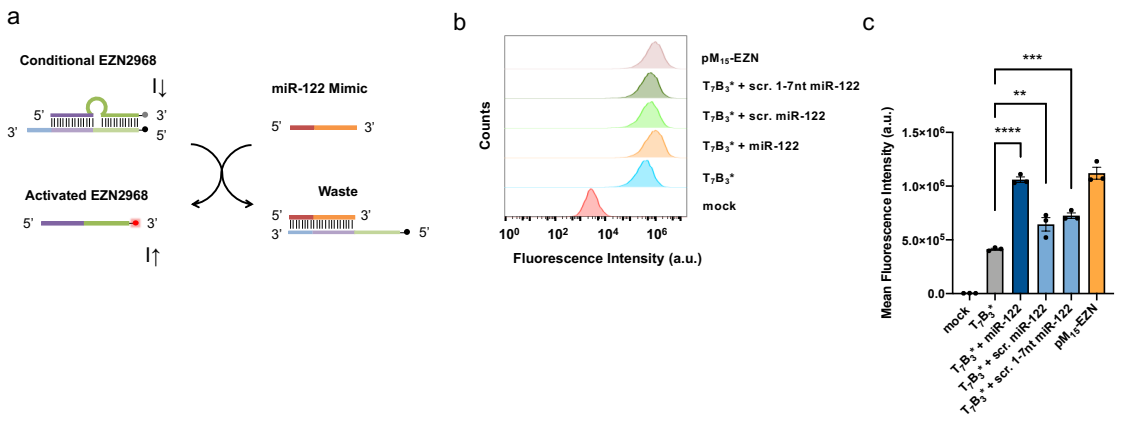

Figure 5.10 Flow cytometry to evaluate specificity of conditional EZN2968 to miR-122.
(a) Scheme showing fluorescence dequenching due to activation of **T_7B_3*** by miR-122 mimic, as well as scheme for scr. miR-122, and scr. 1-7nt miR-122. (b) Histogram and (c) mean fluorescence intensity of U373 cells co-transfected with 10 nM **T_7B_3*** and 500 nM miR-122, scr. miR-122 and scr. 1-7nt miR-122 and incubated for 24h. The error bars represent SEM. ** p<0.01, *** p<0.001, **** p<0.0001, one-way ANOVA with Tukey's multiple comparison.

In addition to the fluorescence intensity-based method, we also utilized changes in fluorescence lifetime to assess specificity of miRNA-inducible ASO activation (Figure 5.11a). In PBS, Cy5 tagged on **pM_{15}-EZN** strand showed an amplitude-averaged lifetime ($\tau_{AV\ Amp}$) of 1.7 ns and an intensity-averaged lifetime ($\tau_{AV\ Int}$) of 1.9 ns; whereas after the **pM_{15}-EZN** strand hybridized to locking strand **B_3*** tagged with quencher, $\tau_{AV\ Amp}$ and $\tau_{AV\ Int}$ of Cy5 decreased to 0.4 ns and 0.7 ns, respectively (Figure 5.11b,c). After incubation of 10 nM Cy5-Q pair labeled **T_7B_3*** with 500 nM miR-122 mimic, $\tau_{AV\ Amp}$ and $\tau_{AV\ Int}$ increased to 0.9 ns and 1.5 ns (Figure 5.11b,c). However, the fluorescence lifetime of **T_7B_3*** with scr. miR-122 and scr. 1-7nt miR-122 showed only slight increase compared to **T_7B_3*** alone group, which is probably due to non-specific binding of the sequences to the **T_7B_3*** (Figure 5.11b,c). Next, we co-transfected U373 cells with **T_7B_3*** and miR-122 mimic or scrambled

miRNA triggers. After 24h, FLIM was conducted on the cells to measure Cy5 fluorescence lifetime within cells. **pM_{15}-EZN-Cy5** and **T_7B_3*** labeled with only Cy5 but not quencher were also transfected as positive controls. As shown in Figure 5.11d-f, cells co-transfected with **T_7B_3*** and miR-122 mimics showed significant increase of Cy5 fluorescence lifetime compared to **T_7B_3*** only group, whereas cells co-transfected with **T_7B_3*** and scr. miR-122 or scr. 1-7nt miR-122 did not. Together, these results indicated that the dequenching of Cy5 caused by separation of the **pM_{15}-EZN** and locking strand **B_3*** was specific to the triggering of miR-122 sequence, which is mediated by the toehold.

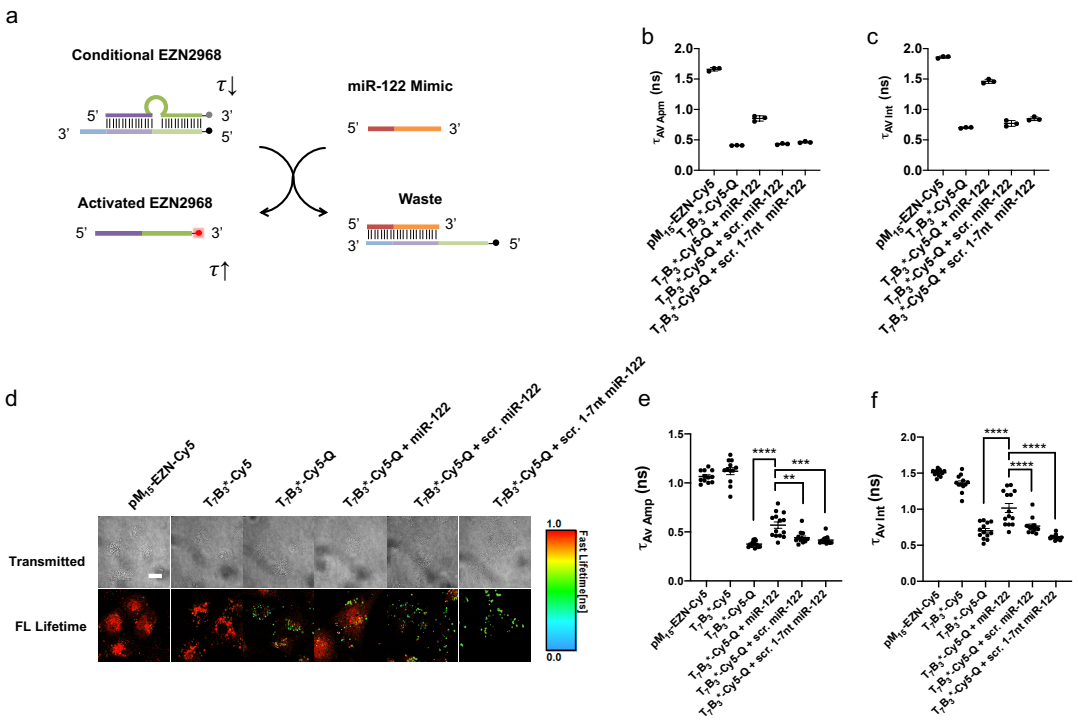

Figure 5.11 FLIM to evaluate specificity of conditional EZN2968 to miR-122.
(a) Scheme showing Cy5 fluorescence lifetime (τ) increase caused by activation of Cy5-Q pair labeled **T_7B_3*** by miR-122. (b) Amplitude-averaged and (c) intensity-averaged Cy5 fluorescence lifetime of 10 nM Cy5-Q-labled **T_7B_3*** solution incubated with 500 nM miR-122, scr. miR-122, or scr. 1-7nt miR-122 for 2h at 37 °C in PBS. Unlocked **pM_{15}-EZN-Cy5** and **T_7B_3*** labeled with only Cy5 but not quencher were used as controls. The error bars represent SD. (d) Representative fluorescence lifetime images (scale bar=20 μm), (e) amplitude-averaged and (f) intensity-averaged fluorescence lifetime of U373 cells transfected with 10 nM Cy5-Q-labeled **T_7B_3*** and 500 nM miR-122, scr. miR-122, or scr. 1-7nt miR-122, and incubated for 24h. Cy5-labled **pM_{15}-EZN** or Cy5-labled **T_7B_3*** transfected cells are positive controls, and Cy5-Q-labled **T_7B_3*** transfected cells are negative controls. Each data point represents the calculated fluorescence lifetime of one image. The error bars represent SEM. ** p<0.01, *** p<0.001, **** p<0.0001, one-way ANOVA with Tukey's multiple comparison.

5.3.6 Endogenous miR-122 induces HIF1α knockdown by conditional EZN2968

Since synthetic miR-122 mimic may have different binding kinetics and thermodynamics to **conditional EZN2968**, which affects its activation, we further tested whether endogenous miR-122 could induce HIF1α knockdown by **T_7B_3***. For this study,

we transfected **T_7B_3*** into Huh7 cells, a hepatocellular carcinoma cell line that express high level of miR-122 (Figure 5.5). The **T_7B_3*** with toehold knocked down HIF1α mRNA by ~40%, whereas the **T_7B_3***with the toehold truncated did not show significant knockdown of HIF1α mRNA, suggesting that the activation by endogenous proceeds through the intended toehold-mediated strand exchange mechanism (Figure 5.12a). Next, we asked if sponging of endogenous miR-122 could prevent the activation of **T_7B_3***. To answer this question, we co-transfected **T_7B_3*** with excess amount of locking strand **B_3*** to compete for endogenous miR-122 binding to **T_7B_3***. The result showed that there was no HIF1α knockdown in the co-transfected groups (Figure 5.12b). We then performed a miR-122 knockdown experiment with Huh7 cells pre-transfected with different concentrations of anti-miR-122. As expected, with increasing concentration of anti-miR-122, the HIF1α knockdown efficacy of **T_7B_3*** in Huh7 cells was reduced, with a complete prevention at 500 nM anti-miR-122 concentration (Figure 5.12c). Together, these data shows that the HIF1α knockdown activity is induced by endogenous miR-122 and depends on miR-122 expression level in the cells.

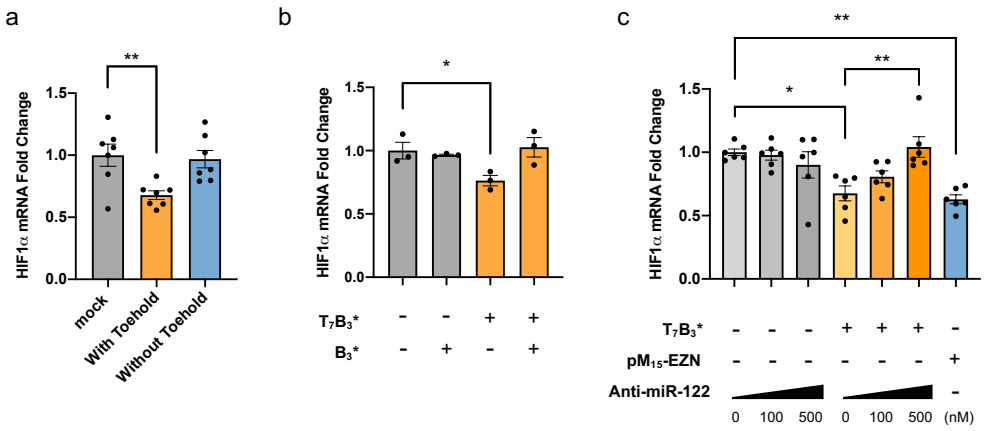

Figure 5.12 Performance of conditional EZN2968 in liver cells.
(a) Huh7 cells were transfected with 50 nM **T_7B_3*** with toehold or without toehold using Oligofectamine. After 24h incubation, HIF1α mRNA levels were quantified by qPCR normalized to 18s. The error bars represent SEM. ** p<0.01, one-way ANOVA with Tukey's multiple comparison. (b) Huh7 cells were co-transfected with 50 nM **T_7B_3*** and 500 nM locking strand **B_3***. After 24h incubation, HIF1α mRNA levels were quantified by qPCR normalized to 18s. The error bars represent SEM. * p<0.05, one-way ANOVA with Tukey's multiple comparison. (c) Huh7 cells were transfected with different concentrations of anti-miR-122 and 50 nM **T_7B_3*** sequentially with a 6h interval. 24h after the second transfection, HIF1α mRNA levels were quantified by qPCR normalized to 18s. The error bars represent SEM. * p<0.05, ** p<0.01, one-way ANOVA with Tukey's multiple comparison.

5.4 Methods

5.4.1 Materials

All oligonucleotides (Table 5.1 and Table 5.2) and primers for qRT-PCR (Table 5.3) were custom synthesized by Integrated DNA Technologies (IDT). Direct-zol RNA Miniprep Plus Kit was acquired from Zymo Research. miScript II RT Kit, and miScript Primer Assays were acquired from QIAGEN. OligofectamineTM Transfection Regent (Invitrogen), High-Capacity cDNA Reverse Transcription Kit (Applied Biosystems) and

PerfeCTa SYBR Green FastMix Reaction Mixes (QuantaBio) were acquired from ThermoFisher Scientific. Luciferase assay system (Cat. #: E4550) was acquired from Promega. HIF1α antibody is purchased from Bethyl Laboratories (Cat. #: A300-286A). β-actin antibody is purchased from Santa Cruz Biotechnology (Cat. #: sc-47778). Goat anti-mouse IgG HRP (Cat. #: 10004302) and Goat anti-rabbit IgG HRP (Cat. #: 10004301) were purchased fromCayman Chemical Company. Ambion Anti-miR miRNA Inhibitor for miR-122 was purchased from ThermoFisher Scientific. U373 cell line was purchased from Sigma-Aldrich (Cat. #: 08061901).

5.4.2 Displacement Assay in buffer

10 nM conditional EZN2968 duplex labeled with Cy5-quencher pair in 90 μL PBS was pre-incubated at 37 degree in a 96 well plate. 10 μL of 1 μM mRNA mimic was added into each well (final concentration = 100 nM) and mixed briefly, and the fluorescence intensity (Ex/Em=630/670 nm) was immediately measured with a Bio-Tek Synergy H1 microplate reader at 37 °C for 2 h with an interval of 15 min. To determine percentage displacement, 10 nM conditional EZN2968 duplex mixed with 10 nM quencher strand was used as a positive control, whose fluorescence intensity represent 100% activation.

5.4.3 Cell Culture

HeLa cells and LN229-V6R-Luc cells were maintained in DMEM containing 4.5 g/L glucose, 10% (v/v) fetal bovine serum (FBS), penicillin (100 U/mL) and streptomycin

(100 mg/mL) at 37 °C under a humidified atmosphere of 5% CO_2. U373 cells were maintained in DMEM containing 1 g/L glucose, 10% (v/v) fetal bovine serum (FBS), penicillin (100 U/mL) and streptomycin (100 mg/mL), 1% NEAA, 1 mM sodium pyruvate and 2 mM L-Glutamine at 37 °C under a humidified atmosphere of 5% CO_2. Huh7 cells were maintained in DMEM containing 4.5 g/L glucose, 10% (v/v) fetal bovine serum (FBS), penicillin (100 U/mL) and streptomycin (100 mg/mL) at 37°C under a humidified atmosphere of 5% CO_2.

5.4.4 T_m Measurement

The melting temperature (T_m) of conditional EZN2968 duplex were measured based on dequenching of fluorescence due to separation of the Cy5-labeled pM-EZN strand and the quencher-labeled locking strand. The fluorescence of 100 nM duplex in PBS was measured with a LightCycler® 96 instrument as a function of temperature. The temperature was ramped from 45°C to 95 °C at the rate of 0.04 °C/s and 25 measurements were performed at each °C. T_m was determined as the temperature that generate half-maximal fluorescence increase in the fitted curves.

5.4.5 Testing spontaneous activation of conditional EZN2968 in HeLa and U373 cells

U373 cells or HeLa cells were plated in 24 well plates with a density of 5×10^4 cells/well the day before experiment. 10 nM conditional EZN2968 was transfected into the cells using Oligofectamine according to manufacturer's protocol (2 μL/well). After 24h

incubation, QIAZOL was then added into the wells to lyse the cells and total RNA was isolated using Direct-zol RNA Miniprep Plus Kit (Zymo Research). RNA was reverse transcribed using High-Capacity cDNA Reverse Transcription Kit (Applied Biosystems). HIF1α mRNA level were quantified by qRT-PCR using PerfeCTa SYBR Green FastMix Reaction Mixes (QuantaBio) with 0.5 μM of custom designed primers (Table S2) with Applied Biosystems StepOnePlusTM real time PCR system. The relative quantification of HIF1α mRNA level was determined using ΔΔCt method with 18s mRNA as a reference.

5.4.6 Testing spontaneous activation of conditional EZN2968 in LN229-V6R-Luc cells

LN229-V6R-Luc cells were plated in opaque 96 well plates with a density of 5×10^4 cells/well the day before experiment. 10 nM conditional EZN2968 was transfected into the cells using Oligofectamine (0.5 μL/well). After 4 h, medium with serum along with IOX4 was added to each well. The final concentration of IOX4 was 20 μM/well. After incubation for another 20 h, luciferase assay was conducted per manufacturer's protocol.

5.4.7 miR-122 mimic triggered activation of conditional EZN2968 in U373 cells

U373 cells were plated in 24 well plates with a density of 5×10^4 cells/well the day before experiment. 10 nM conditional EZN2968 and 500 nM miR-122 mimic were co-transfected into the cells using Oligofectamine according to manufacturer's protocol (2 μL/well in total). Note that the transfection mixtures of conditional EZN2968 and miR-122 mimic were prepared separately and added into the wells simultaneously to avoid reaction

of conditional EZN2968 and miR-122 mimic during incubation before transfection. 10 nM conditional EZN2968 only and 500 nM miR-122 mimic only groups were used as controls. After 24h incubation, HIF1α mRNA levels were quantified by qRT-PCR as described above.

5.4.8 Testing knockdown HIF1α in Huh7 cells triggered by endogenous miR-122

Huh7 cells were plated in 24 well plates with a density of 10^5 cells/well the day before experiment. 50 nM of conditional EZN2968 was transfected into Huh7 cells using Oligofectamine according to manufacturer's protocol (2 μL/well). After 24h incubation, HIF1α mRNA levels were quantified by qRT-PCR as described above.

5.4.9 miR-122 dependency of HIF1α knockdown in Huh7 cells

Huh7 cells were plated in 24 well plates with a density of 10^5 cells/well the day before experiment. Huh7 cells were transfected with 0 nM, 100 nM or 500 nM anti-miR-122 using Oligofetamine and incubated for 6 h (medium with 3× serum was added 4h after transfection). Then, 50 nM conditional EZN2968 was transfected using oligofectamine. After another 24 h incubation, HIF1α mRNA levels were quantified by qRT-PCR as described above.

5.4.10 Western Blot

The cells were lysed using a lysis buffer with 50 mM Tris-HCl (pH 6.8), 10% glycerol, 2.5% SDS, 5mM DTT, and 6 M urea supplemented with a protease inhibitor cocktail. The proteins were quantified with BCA assay and diluted in the lysis buffer with reducing loading dye to a final protein amount of ~10-20 μg, and boiled at 95°C for 5 min. The proteins were separated by electrophoresis in an 8% Tris–HCl polyacrylamide gel, before transferring onto a polyvinylidene fluoride (PVDF) membrane. After blocked for 1h in 5% (w/v) non-fat milk in Tris-Buffered Saline with 0.1% Tween (TBST), the membranes were immunoblotted using primary antibodies against human HIF-1α (1:500 dilution) or β-actin (1:3000 dilution) for overnight at 4°C. After wash, the membranes incubated with secondary horseradish peroxide-conjugated antibody (1:5000) for 1h at room temperature. After washing, Immobilon Western Chemiluminescent HRP substrate was added to the membrane and the membrane was imaged using iBright FL1000 imaging system.

5.4.11 Flow Cytometry

HeLa cells or U373 cells were plated in 12 well plate with 10^5 cells/well the day before experiment. For testing spontaneous activation, cells were transfected with 10 nM conditional EZN2968 labeled with Cy5-quencher pair and incubated for 24 h. For testing miR-122 triggered activation of conditional EZN2968, the cells were co-transfected with 10 nM conditional EZN2968 and 500 nM miR-122 and incubated for 24 h. The cells were then trypsinized and washed with HBSS twice and resuspended in HBSS for flow cytometry assessment to measure cell-associated fluorescence intensity of Cy5.

5.4.12 FLIM

U373 cells were plated in glass-bottom black 96 well plates with a density of 10^4 cells/well one day before experiment. The cells were co-transfected with 10 nM Cy5-Q labeled conditional EZN2968 and 500 nM miR-122, scr. miR-122 or scr. 1-7nt miR-122 using Oligofectamine and incubated for 24 h. The cells were then washed with FluoroBrite once and then 100 uL of FluoroBrite was added to the wells before the cells were imaged. The FLIM images were analyzed using SymphoTime (PicoQuant) software. The overall fluorescence lifetime decay trace was fitted to a biexponential function through an iterative reconvolution method. The instrument response function (IRF) for the iterative reconvolution analysis was measured using saturated Coomassie Blue and potassium Iodide (KI) solution.

5.4.13 Statistics

All statistical analysis was performed using Graphpad Prism software. Quantitative results for *in vitro* experiments were presented as mean ± SEM. Statistical analysis were performed by one-way analysis of variance (ANOVA) followed by post-test multiple comparison as described in the figure captions. P values of less than 0.05 were considered significant.

5.4.14 Sequences

Table 5.1 Oligonucleotide sequences for in buffer testing of leakage activation of bulge and end destabilized conditional EZN2968

/3AmMO/= 3' amino modification; /5IAbRQ/=5' Iowa Black RQ; /5AmMC6/=5' amino modification; "T" indicates a mismatch on the toehold binding region.

ID	Sequence
Unmodified pM_{12}-EZN	CAA TGG TGT TTG TGG CAA GCA TCC TGT A/3AmMO/
Unmodified pM_{15}-EZN	TGA CAA TGG TGT TTG TGG CAA GCA TCC TGT A/3AmMO/
Unmodified pM_{18}-EZN	GTG TGA CAA TGG TGT TTG TGG CAA GCA TCC TGT A/3AmMO/
Unmodified B_0	/5IAbRQ/TA CAG GAT GCT TGC CAC AAA CAC CAT TGT CAC TCT CCA
Unmodified B_3	/5IAbRQ/TA CAG GAT GCT TGC AAA CAC CAT TGT CAC TCT CCA
Unmodified B_5	/5IAbRQ/TA CAG GAT GCT CAA ACA CCA TTG TCA CTC TCC A
Unmodified B_7	/5IAbRQ/TA CAG GAT GCA AAC ACC ATT GTC ACT CTC CA
Unmodified E_3	/5IAbRQ/AG GAT GCT TGC CAC AAA CAC CAT TGT CAC TCT CCA
Unmodified E_5	/5IAbRQ/GA TGC TTG CCA CAA ACA CCA TTG TCA CTC TCC A
Unmodified E_7	/5IAbRQ/TG CTT GCC ACA AAC ACC ATT GTC ACT CTC CA

Table 5.2 Oligonucleotide sequences for *in vitro* testing of conditional EZN2968

"+" = LNA modification; "*" = PS modification; /3AmMO/ = 3' amino modification; "T" indicates a mismatch on the toehold binding region.

ID	Sequence
EZN2968	+T*+G*+G* C*A*A* G*C*A* T*C*C* +T*+G*+T* A
EZN3088	+C*+G*+T* C*A*G* T*A*T* G*C*G* +A*+A*+T* C
Modified pM_{12}-EZN	C*A*A* T*G*G* T*G*T* T*T*G* +T*+G*+G* C*A*A* G*C*A* T*C*C* +T*+G*+T* A/3AmMO/
Modified pM_{15}-EZN	T*G*A* C*A*A* T*G*G* T*G*T* T*T*G* +T*+G*+G* C*A*A* G*C*A* T*C*C* +T*+G*+T* A/3AmMO/
Modified B_0 (B_0*)	/5IAbRQ/+T*+A* +C*A*G* G*A*T* G*C*T* T*G*C* C*A*C* A*A*A* C*A*C* C*A*T* T*G*+T* +C*+A*C* A*C*T* C*C*A
Modified B_3 (B_3*)	/5IAbRQ/*T*A* C*A*G* G*A*T* G*C*+T* +T*+G*+C* +A*+A*A* C*A*C* C*A*T* T*G*T* C*A*C* A*C*T* C*C*A
Modified B_5 (B_5*)	/5IAbRQ/*T*A* C*A*G* G*A*T* +G*+C*+T* +C*+A*+A* A*C*A* C*C*A* T*T*G* T*C*A* C*T*C* T*C*C* A
B_3* without toehold	/5IAbRQ/T*A* C*A*G* G*A*T* G*C*+T* +T*+G*+C* +A*+A*A* C*A*C* C*A*T* T*G*T* C*A
miR-122 mimic	+T*G*G* +A*G*T* +G*T*G* +A*C*A* +A*T*G* +G*T*G* +T*T*T* +G
Scr. miR-122	+G*A*A*+G*T*A*+T*G*T*+G*G*T*+G*A*T*+T*G*C*+G*T*G*+T
Scr. 1-7nt miR-122	+G*G*G*+T*T*G*+A*T*G*+A*C*A*+A*T*G*+G*T*G*+T*T*T*+G

Table 5.3 Primer Sequences used in Chapter 5

Primer	Sequence (5'→3')
HIF1α_Forward	TATGAGCCAGAAGAACTTTTAGGC
HIF1α_Reverse	CACCTCTTTTGGCAAGCATCCTG
18s_Forward	AGGAATTGACGGAAGGGCACCA
18s_Reverse	GTGCAGCCCCGGACATCTAAG

5.5 Conclusion, discussion and future direction

In this study, we established design principles and experimental approaches for adapting dynamic strand displacement reaction to cellular environment for the purpose of conditional gene regulation to improve specificity of ASO therapeutics. We used miR-122 triggered HIF1α ASO activation as a model and systemically explored how the interplay of molecular structure, chemistry and thermostability determine the performance of conditional ASO in cells. We successfully demonstrated ASO-mediated HIF1α knockdown triggered by either synthetic miR-122 mimic or endogenously expressed miR-122, while inhibited by anti-miR-122. Together, this proof-of-concept study demonstrated the applicability of conditional ASO in cell-type specific control of RNA therapeutic activity. This platform holds promise in conditional gene regulation to enhance specificity of RNA therapeutics. By adjusting the specific RNA trigger, their inducible activity could be achieved in a wider range of tissues and cell-subtypes. The conditional oligonucleotides could be further combined with common delivery methods, such as lipid conjugation and nanomaterial delivery vehicles, to facilitate their cellular internalization.

As for future directions, optimization of conditional ASOs can be performed to identify designs that offer a wider dynamic range, higher miRNA sensitivity and faster activation kinetics, possibly through modulation of chemical modifications on different domains of the duplex. Besides, because dehybridization may occur for double-stranded conditional ASOs due to dilution, bridging the 3' terminus of the **pM-EZN** strand and the 5' end of the locking strand could potentially reduce spontaneous activation, and provide reversibility of the conditional ASOs.

Since systemically delivered oligonucleotides mostly accumulate in the liver, conditionally silencing oligonucleotide activity in the liver could be beneficial. This "on-to-off" switching mechanism could potentially be achieved through extending both termini of the ASO with partial miR-122 complementary sequences, which allows formation of three-way junction to conceal the ASO sequence in the presence of miR-122. Because additional sequences are inserted or extended in the oligonucleotide therapeutics, rational design and optimization is needed to prevent the formation of stable secondary structures of the oligonucleotide therapeutics, which might eliminate their RNA binding ability. In addition, off-target effect caused by extended or inserted sequences need to be evaluated through transcriptomics studies to validate the safety of individual design of conditional oligonucleotide therapeutics.

CHAPTER 6. OVERALL SUMMARY AND FUTURE DIRECTION

6.1 Overall Summary and Discussion

Achieving tissue or cell type specificity is the key for application of oligonucleotide therapeutics to a wider range of clinical indications with minimal side effects. In this dissertation, we proposed a novel mechanism to control the activity of oligonucleotides therapeutics with endogenous specific transcript that are either disease-related or tissue-specific. We have demonstrated two model systems for conditional oligonucleotide therapeutics or their NP conjugates to improve their cell type and tissue specificity: (1) miR-33 responsive DNAzyme-AuNP to down regulate TNFα in pro-inflammatory macrophages; (2) miR-122 inducible antisense to down regulate HIF1α in liver cells. These models demonstrated proof-of-concept for conditional gene regulatory agents, whose design principles could be adopted to a wide variety of smart nucleic acid therapeutics that is controlled by endogenous transcripts. In addition, we demonstrated that the intracellular integrity of oligonucleotide-AuNP conjugates can be monitored using FLIM, which provides a powerful tool to potentially map the spatial and temporal dynamics of DNA-AuNP disassembly if combined with correlative fluorescence imaging.

Specifically, we found that by partially or completely blocking the sequence of oligonucleotide therapeutics with complementary sequences can render them inactive for target RNA binding. To minimize spontaneous leakage activation intracellularly, nucleases resistance and thermostability of the hybridized duplex are both necessary.

Removing the blocking sequence via toehold mediated strand displacement reaction by a trigger transcript can recover the binding capability of the oligonucleotide therapeutics to their mRNA targets. We demonstrated the dependence of activation of conditional oligonucleotides depending on the concentration of an intracellular trigger and the presence of the toehold. Attaching the conditional oligonucleotides to AuNP surface could facilitate their cellular uptake. We can also imagine delivery of these conditional oligonucleotides *in vitro* and *in vivo* utilizing the common delivery vehicles, such as lipid nanoparticles, exosomes, and polymer-based nanoparticles.

Using FLIM we showed that chemical modifications of DNA-AuNPs can further enhance the stability of the oligonucleotides, which provides longer intracellular half-life of the therapeutics and potentially improved potency. FLIM studies showed that strengthening the anchor of oligonucleotides on AuNP surface does not enhance the intracellular stability of the DNA-AuNP conjugates.

Nucleic acid-controlled oligonucleotide therapeutics offer opportunities to interface gene regulation with endogenous transcript inputs. In this dissertation, we mostly focused on miRNA-inducible oligonucleotide activities, or "off-to-on" switching. However, since toehold-mediated strand displacement reaction has been demonstrated as a versatile building block for a variety of logic gates as well as more complex computation circuits, we can potentially design and generate smart nucleic acid therapeutics that can translate the recognition of diverse nucleic acid inputs into defined gene regulatory outputs. The simplest designs that can be pursued next are conditional oligonucleotide therapeutics controlled by dual inputs via AND or OR gate, and "on-to-off" switchable oligonucleotide therapeutics through three-way junction formation. In addition to toehold-

mediated strand displacement reactions, interactions of nucleic acid to proteins and small molecules (eg. aptamers) could also be incorporated in the design of smart oligonucleotide therapeutics to achieve responsiveness to a wider range of inputs.

Although nucleic acid-responsive oligonucleotide therapeutics hold great promise in the development of a variety of on-demand and autonomous therapeutics, several factors need to be considered on a case-by-case basis. First, since this approach requires adding extra sequences on the parental oligonucleotide therapeutics, off-target effect of the new sequences need to be assessed to ensure no significant alteration of expression level of non-targeted transcripts. Second, the choice of endogenous trigger is important for the success of controllability of the conditional therapeutics. An ideal trigger transcript should be specific and abundant to ensure minimum non-specific activation and fast response. In addition, if a fragment of a mRNA is chosen as the trigger, the accessibility of the fragment needs to be taken into account as long transcripts may fold into secondary or tertiary structures. Third, chemical modifications can dramatically influence the thermodynamic stability of the duplex and the binding affinity to the trigger. Tuning the type, number and position of the chemical modification could potentially alter the responsiveness of the conditional therapeutics.

In this dissertation, we focused on intermolecular interaction between the “lock” strand and the active oligonucleotide therapeutics. Toward their application *in vivo*, the two strands could be connected to form a hairpin, which may eliminate the potential leakage caused by dehybridization due to dilution and provide reversibility of the conditional therapeutics. To sense a trigger transcript with low abundancy, catalytic

amplification may be incorporated in the design by using a fuel strand to displace the bound trigger, which then enter the next cycle of activation.

The control of oligonucleotide activity is the foundation for programmable oligonucleotide therapeutics. We envision precise medicine by controlling the location, timing, and potency of therapeutic oligonucleotides using pre-programmed logic circuits.

6.2 Future Direction

Although in this dissertation we only investigated two model systems to demonstrate conditional gene regulation, we hope to translate the findings from our studies to improve the pharmacodynamics, specificity and safety of the oligonucleotide therapeutics in clinical applications. Herein, we propose several disease contexts, where conditional oligonucleotides could be used to regulate gene expression selectively in targeted tissue and diseased cell types.

6.2.1 Selective inhibition of HIF1α in cancer cells

Transcriptome alterations are prevalent in cancer due to both genetic and epigenetic alterations involved in oncogenicity. The application of microarray, high-throughput RNA sequencing (RNA-seq) and bioinformatic approaches has revealed diversity and complexity in cancer transcriptome, as well as a set of tumor-specific aberrantly expressed

or spliced transcripts, many of which involve in tumor initiation and development. [347-349]

Hepatocellular carcinoma (HCC) is one of the most lethal cancers worldwide. Zheng *et al*. found that hundreds of tumor-specific transcripts (TSTs) are expressed in HCC through in-depth analysis of tumor-specific junctions using RNA-seq. [347] As an example, TST1, an intergenic noncoding transcript that is expressed in HCC tissues but not detected in normal liver tissues and other healthy tissues, regulates HCC cell proliferation and tumorigenesis by directly binding to onco-suppressor miR-500a-3p and rescue its tumor-inhibitory effects. [347]

Another example of TST is a LIN28B variant. LIN28B is highly expressed during embryogenesis but silent in most adult tissues. [350] LIN28B has been found to be highly expressed in various type of human cancer and promotes tumor initiation and maintenance. [351, 352] RNA-seq analysis revealed a LIN28B variant, LIN28B-TST, that is specifically expressed in HCC and many other cancer cell types but not in healthy adult liver tissues. LIN28B-TST is produced by an alternative transcription initiation site due to demethylation of its promoter, and encodes a long protein isoform with additional N-terminal amino acids that is critical for cancer cell proliferation and tumorigenesis. [353]

A novel isoform of anaplastic lymphoma kinase (ALK), ALK^{ATI}, has been reported to be specifically expressed in melanomas and sporadically in other human cancer but not in normal tissues. This transcript is also produced by alternative transcription initiation site associated with chromatin alterations. ALK^{ATI} induces multiple oncogenic signaling pathways and promote tumorigenesis in mouse model. [354]

Since these TSTs are specifically expressed in cancer, they could be used as triggers to control the activity of HIF1α antisense or other oligonucleotide therapeutics against cancer selectively in cancer cells. In addition, because many TSTs involve in tumorigenesis and tumor maintenance, the locking strands may function as the second active drug to down regulate these TSTs, which provide dual anticancer effects.

6.2.2 Selective knockdown of αSyn in Parkinson's disease-associated neurons

Central nervous system disorders have been targeted by oligonucleotide therapeutics, such as Parkinson's disease. Accumulation of α-Synuclein (αSyn) is a hallmark of Parkinson's disease, and a cause of neurodegeneration. [355] siRNAs and ASOs targeting αSyn have been shown to down regulate αSyn expression in neurons and prevent early dysfunctions in a mouse model of Parkinson's disease. [356, 357] However, since αSyn may play a significant role in neurotransmitter release, synaptic function and neuroplasticity, elimination of αSyn may impair brain function. [356]

Differential co-expression analysis of Parkinson's disease brain tissue identified a transcript isoform of αSyn with longer 3'-UTR, termed αSynL, caused by alternative polyadenylation site selection. [358] The ratio of αSynL to shorter αSyn transcript is increased in Parkinson's disease, and this transcript lead to increased protein translation as well as the preferential accumulation of αSyn protein from synaptic terminals and towards mitochondria, which is consistent with the pathology of this disease. [358] Utilizing the alternative 3'-UTR of αSyn as a trigger to control the activity of αSyn targeting ASO may

potentially reduce its side effect by selectively down regulate αSyn expression in neurons expressing high level of Parkinson's disease-related αSynL transcript.

The above-described disease contexts are only two examples where conditional oligonucleotides may provide merits in terms of sparing normal tissues from side effect by selectively activating the therapeutics using disease-associated transcripts. We believe that with the discovery of more disease-related specific transcripts by transcriptomics technologies, conditional oligonucleotide therapeutics can open up new opportunities to address intractable diseases with better controllability and safety.

REFERENCES

1. Santos, R., et al., *A comprehensive map of molecular drug targets*. Nature reviews Drug discovery, 2017. **16**(1): p. 19-34.

2. Warner, K.D., C.E. Hajdin, and K.M. Weeks, *Principles for targeting RNA with drug-like small molecules*. Nature Reviews Drug Discovery, 2018. **17**(8): p. 547-558.

3. Esteller, M., *Non-coding RNAs in human disease*. Nature reviews genetics, 2011. **12**(12): p. 861-874.

4. DiStefano, J.K., *The emerging role of long noncoding RNAs in human disease*, in *Disease Gene Identification*. 2018, Springer. p. 91-110.

5. Wilson, D.N., et al., *The oxazolidinone antibiotics perturb the ribosomal peptidyl-transferase center and effect tRNA positioning*. Proceedings of the National Academy of Sciences, 2008. **105**(36): p. 13339-13344.

6. Poehlsgaard, J. and S. Douthwaite, *The bacterial ribosome as a target for antibiotics*. Nature Reviews Microbiology, 2005. **3**(11): p. 870-881.

7. Mei, H.-Y., et al., *Discovery of selective, small-molecule inhibitors of RNA complexes—1. The tat protein/TAR RNA complexes required for HIV-1 transcription*. Bioorganic & medicinal chemistry, 1997. **5**(6): p. 1173-1184.

8. Todd, P.K. and H.L. Paulson, *RNA-mediated neurodegeneration in repeat expansion disorders*. Annals of neurology, 2010. **67**(3): p. 291-300.

9. Fu, Y., et al., *An unstable triplet repeat in a gene related to myotonic muscular dystrophy*. Science, 1992. **255**(5049): p. 1256-1258.

10. Liquori, C.L., et al., *Myotonic dystrophy type 2 caused by a CCTG expansion in intron 1 of ZNF9*. Science, 2001. **293**(5531): p. 864-867.

11. Ho, T.H., et al., *Colocalization of muscleblind with RNA foci is separable from mis-regulation of alternative splicing in myotonic dystrophy*. Journal of cell science, 2005. **118**(13): p. 2923-2933.

12. Warf, M.B., et al., *Pentamidine reverses the splicing defects associated with myotonic dystrophy*. Proceedings of the National Academy of Sciences, 2009. **106**(44): p. 18551-18556.

13. Lee, M.M., et al., *Controlling the specificity of modularly assembled small molecules for RNA via ligand module spacing: targeting the RNAs that cause myotonic muscular dystrophy*. Journal of the American Chemical Society, 2009. **131**(47): p. 17464-17472.

14. Costales, M.G., et al., *Small molecule inhibition of microRNA-210 reprograms an oncogenic hypoxic circuit*. Journal of the American Chemical Society, 2017. **139**(9): p. 3446-3455.

15. Zhong, Z., et al., *mRNA therapeutics deliver a hopeful message*. Nano today, 2018. **23**: p. 16-39.

16. Brito, L.A., et al., *Self-amplifying mRNA vaccines*, in *Advances in genetics*. 2015, Elsevier. p. 179-233.

17. Sahin, U., K. Karikó, and Ö. Türeci, *mRNA-based therapeutics—developing a new class of drugs*. Nature reviews Drug discovery, 2014. **13**(10): p. 759-780.

18. Weng, Y., et al., *The challenge and prospect of mRNA therapeutics landscape*. Biotechnology Advances, 2020: p. 107534.

19. Gilboa, E. and J. Vieweg, *Cancer immunotherapy with mRNA-transfected dendritic cells*. Immunological reviews, 2004. **199**(1): p. 251-263.

20. Maruggi, G., et al., *mRNA as a transformative technology for vaccine development to control infectious diseases*. Molecular Therapy, 2019. **27**(4): p. 757-772.

21. Jackson, L.A., et al., *An mRNA vaccine against SARS-CoV-2—preliminary report*. New England Journal of Medicine, 2020.

22. Magadum, A., K. Kaur, and L. Zangi, *mRNA-based protein replacement therapy for the heart*. Molecular Therapy, 2019. **27**(4): p. 785-793.

23. Trepotec, Z., et al., *Delivery of mRNA therapeutics for the treatment of hepatic diseases*. Molecular Therapy, 2019. **27**(4): p. 794-802.

24. Warren, L. and C. Lin, *mRNA-based genetic reprogramming*. Molecular Therapy, 2019. **27**(4): p. 729-734.

25. Zhang, H.-X., Y. Zhang, and H. Yin, *Genome editing with mRNA encoding ZFN, TALEN, and Cas9*. Molecular Therapy, 2019. **27**(4): p. 735-746.

26. Xiao, L., et al., *Adoptive transfer of NKG2D CAR mRNA-engineered natural killer cells in colorectal cancer patients*. Molecular Therapy, 2019. **27**(6): p. 1114-1125.

27. Wiesinger, M., et al., *Clinical-scale production of CAR-T cells for the treatment of melanoma patients by mRNA transfection of a CSPG4-Specific CAR under full GMP compliance*. Cancers, 2019. **11**(8): p. 1198.

28. Verbeke, R., et al., *Three decades of messenger RNA vaccine development*. Nano Today, 2019. **28**: p. 100766.

29. de Smet, M.D., C. Meenken, and G.J. van den Horn, *Fomivirsen–a phosphorothioate oligonucleotide for the treatment of CMV retinitis*. Ocular immunology and inflammation, 1999. **7**(3-4): p. 189-198.

30. Raal, F.J., et al., *Mipomersen, an apolipoprotein B synthesis inhibitor, for lowering of LDL cholesterol concentrations in patients with homozygous familial hypercholesterolaemia: a randomised, double-blind, placebo-controlled trial*. The Lancet, 2010. **375**(9719): p. 998-1006.

31. Benson, M.D., et al., *Inotersen treatment for patients with hereditary transthyretin amyloidosis*. New England Journal of Medicine, 2018. **379**(1): p. 22-31.

32. Witztum, J.L., et al., *Volanesorsen and triglyceride levels in familial chylomicronemia syndrome*. New England Journal of Medicine, 2019. **381**(6): p. 531-542.

33. Boiziau, C., et al., *Inhibition of translation initiation by antisense oligonucleotides via an RNase-H independent mechanism*. Nucleic acids research, 1991. **19**(5): p. 1113-1119.

34. Sasaki, S., et al., *Steric inhibition of 5′ UTR regulatory elements results in upregulation of human CFTR*. Molecular Therapy, 2019. **27**(10): p. 1749-1757.

35. Liang, X.-h., et al., *Translation efficiency of mRNAs is increased by antisense oligonucleotides targeting upstream open reading frames*. Nature biotechnology, 2016. **34**(8): p. 875-880.

36. Roberts, T.C., R. Langer, and M.J. Wood, *Advances in oligonucleotide drug delivery*. Nature Reviews Drug Discovery, 2020: p. 1-22.

37. Havens, M.A. and M.L. Hastings, *Splice-switching antisense oligonucleotides as therapeutic drugs*. Nucleic acids research, 2016. **44**(14): p. 6549-6563.

38. Disterer, P., et al., *Development of therapeutic splice-switching oligonucleotides*. Human gene therapy, 2014. **25**(7): p. 587-598.

39. Aartsma-Rus, A., *Antisense-mediated modulation of splicing: therapeutic implications for Duchenne muscular dystrophy*. RNA biology, 2010. **7**(4): p. 453-461.

40. Niks, E.H. and A. Aartsma-Rus, *Exon skipping: a first in class strategy for Duchenne muscular dystrophy*. Expert opinion on biological therapy, 2017. **17**(2): p. 225-236.

41. Wood, M.J., K. Talbot, and M. Bowerman, *Spinal muscular atrophy: antisense oligonucleotide therapy opens the door to an integrated therapeutic landscape*. Human molecular genetics, 2017. **26**(R2): p. R151-R159.

42. Dong, A., et al., *2'-O-methoxyethyl splice-switching oligos correct splicing from IVS2-745 β-thalassemia patient cells restoring HbA production and chain rebalance*. Haematologica, 2020.

43. Yilmaz-Elis, S., et al., *Antisense oligonucleotide mediated exon skipping as a potential strategy for the treatment of a variety of inflammatory diseases such as rheumatoid arthritis*. Annals of the Rheumatic Diseases, 2012. **71**(Suppl 2): p. i75-i77.

44. Mendell, J.R., et al., *Eteplirsen for the treatment of Duchenne muscular dystrophy*. Annals of neurology, 2013. **74**(5): p. 637-647.

45. Frank, D.E., et al., *Increased dystrophin production with golodirsen in patients with Duchenne muscular dystrophy*. Neurology, 2020. **94**(21): p. e2270-e2282.

46. Chiriboga, C.A., *Nusinersen for the treatment of spinal muscular atrophy*. Expert review of neurotherapeutics, 2017. **17**(10): p. 955-962.

47. Kim, J., et al., *Patient-customized oligonucleotide therapy for a rare genetic disease*. New England Journal of Medicine, 2019. **381**(17): p. 1644-1652.

48. Elbashir, S.M., et al., *Duplexes of 21-nucleotide RNAs mediate RNA interference in cultured mammalian cells*. nature, 2001. **411**(6836): p. 494-498.

49. Rand, T.A., et al., *Argonaute2 cleaves the anti-guide strand of siRNA during RISC activation*. Cell, 2005. **123**(4): p. 621-629.

50. Setten, R.L., J.J. Rossi, and S.-p. Han, *The current state and future directions of RNAi-based therapeutics*. Nature Reviews Drug Discovery, 2019. **18**(6): p. 421-446.

51. Khvorova, A. and J.K. Watts, *The chemical evolution of oligonucleotide therapies of clinical utility*. Nature biotechnology, 2017. **35**(3): p. 238.

52. Adams, D., et al., *Patisiran, an RNAi therapeutic, for hereditary transthyretin amyloidosis*. New England Journal of Medicine, 2018. **379**(1): p. 11-21.

53. Balwani, M., et al., *Phase 3 Trial of RNAi Therapeutic Givosiran for Acute Intermittent Porphyria*. New England Journal of Medicine, 2020. **382**(24): p. 2289-2301.

54. Santoro, S.W. and G.F. Joyce, *A general purpose RNA-cleaving DNA enzyme*. Proceedings of the national academy of sciences, 1997. **94**(9): p. 4262-4266.

55. Cieslak, M., et al., *Structural rearrangements of the 10–23 DNAzyme to β3 integrin subunit mRNA induced by cations and their relations to the catalytic activity*. Journal of Biological Chemistry, 2003. **278**(48): p. 47987-47996.

56. Cao, Y., et al., *Therapeutic evaluation of Epstein-Barr virus-encoded latent membrane protein-1 targeted DNAzyme for treating of nasopharyngeal carcinomas*. Molecular Therapy, 2014. **22**(2): p. 371-377.

57. Cho, E.-A., et al., *Safety and tolerability of an intratumorally injected DNAzyme, Dz13, in patients with nodular basal-cell carcinoma: a phase 1 first-in-human trial (DISCOVER)*. The Lancet, 2013. **381**(9880): p. 1835-1843.

58. Sel, S., et al., *Effective prevention and therapy of experimental allergic asthma using a GATA-3–specific DNAzyme*. Journal of Allergy and Clinical Immunology, 2008. **121**(4): p. 910-916. e5.

59. Fürste, J.P., V.A. Erdmann, and J. Kurreck, *Sequence requirements in the catalytic core of the "10-23" DNA enzyme*. Journal of Biological Chemistry, 2002. **277**(43): p. 40617-40622.

60. Robaldo, L., et al., *Activity of Core-Modified 10–23 DNAzymes against HCV*. ChemMedChem, 2014. **9**(9): p. 2172-2177.

61. Robaldo, L., J.M. Montserrat, and A.M. Iribarren, *10-23 DNAzyme modified with (2′ R)-and (2′ S)-2′-deoxy-2′-C-methyluridine in the catalytic core*. Bioorganic & medicinal chemistry letters, 2010. **20**(15): p. 4367-4370.

62. Khachigian, L.M., *Deoxyribozymes as catalytic nanotherapeutic agents*. Cancer research, 2019. **79**(5): p. 879-888.

63. Hanna, J., G.S. Hossain, and J. Kocerha, *The potential for microRNA therapeutics and clinical research*. Frontiers in genetics, 2019. **10**: p. 478.

64. Wang, Z., *miRNA Mimic Technology*, in *MicroRNA Interference Technologies*. 2009, Springer. p. 93-100.

65. Wang, Z., *The guideline of the design and validation of MiRNA mimics*, in *MicroRNA and Cancer*. 2011, Springer. p. 211-223.

66. Weiler, J., J. Hunziker, and J. Hall, *Anti-miRNA oligonucleotides (AMOs): ammunition to target miRNAs implicated in human disease?* Gene therapy, 2006. **13**(6): p. 496-502.

67. Lennox, K. and M. Behlke, *Chemical modification and design of anti-miRNA oligonucleotides*. Gene therapy, 2011. **18**(12): p. 1111-1120.

68. De Santi, C., et al., *Precise targeting of miRNA sites restores CFTR activity in CF bronchial epithelial cells*. Molecular Therapy, 2020.

69. Geary, R.S., *Antisense oligonucleotide pharmacokinetics and metabolism*. Expert opinion on drug metabolism & toxicology, 2009. **5**(4): p. 381-391.

70. Judge, A.D., et al., *Sequence-dependent stimulation of the mammalian innate immune response by synthetic siRNA*. Nature biotechnology, 2005. **23**(4): p. 457-462.

71. Cekaite, L., et al., *Gene expression analysis in blood cells in response to unmodified and 2'-modified siRNAs reveals TLR-dependent and independent effects*. Journal of molecular biology, 2007. **365**(1): p. 90-108.

72. Sioud, M., G. Furset, and L. Cekaite, *Suppression of immunostimulatory siRNA-driven innate immune activation by 2'-modified RNAs*. Biochemical and biophysical research communications, 2007. **361**(1): p. 122-126.

73. Wan, W.B. and P.P. Seth, *The medicinal chemistry of therapeutic oligonucleotides*. Journal of Medicinal Chemistry, 2016. **59**(21): p. 9645-9667.

74. Freier, S.M. and K.-H. Altmann, *The ups and downs of nucleic acid duplex stability: structure-stability studies on chemically-modified DNA: RNA duplexes*. Nucleic acids research, 1997. **25**(22): p. 4429-4443.

75. Brown, D.A., et al., *Effect of phosphorothioate modification of oligodeoxynucleotides on specific protein binding*. Journal of Biological Chemistry, 1994. **269**(43): p. 26801-26805.

76. Liang, X.-h., et al., *Identification and characterization of intracellular proteins that bind oligonucleotides with phosphorothioate linkages*. Nucleic acids research, 2015. **43**(5): p. 2927-2945.

77. Miller, C.M., et al., *Stabilin-1 and Stabilin-2 are specific receptors for the cellular internalization of phosphorothioate-modified antisense oligonucleotides (ASOs) in the liver*. Nucleic acids research, 2016. **44**(6): p. 2782-2794.

78. Yanai, H., et al., *Suppression of immune responses by nonimmunogenic oligodeoxynucleotides with high affinity for high-mobility group box proteins (HMGBs)*. Proceedings of the National Academy of Sciences, 2011. **108**(28): p. 11542-11547.

79. Shen, W., et al., *Chemical modification of PS-ASO therapeutics reduces cellular protein-binding and improves the therapeutic index*. Nature biotechnology, 2019. **37**(6): p. 640-650.

80. Singh, S.K., et al., *LNA (locked nucleic acids): synthesis and high-affinity nucleic acid recognition*. Chemical communications, 1998(4): p. 455-456.

81. Morita, K., et al., *2'-O, 4'-C-ethylene-bridged nucleic acids (ENA): highly nuclease-resistant and thermodynamically stable oligonucleotides for antisense drug*. Bioorganic & Medicinal Chemistry Letters, 2002. **12**(1): p. 73-76.

82. Kang, H., et al., *Inhibition of MDR1 gene expression by chimeric HNA antisense oligonucleotides*. Nucleic Acids Research, 2004. **32**(14): p. 4411-4419.

83. Langkjær, N., A. Pasternak, and J. Wengel, *UNA (unlocked nucleic acid): a flexible RNA mimic that allows engineering of nucleic acid duplex stability*. Bioorganic & medicinal chemistry, 2009. **17**(15): p. 5420-5425.

84. Snead, N.M., et al., *5′ Unlocked nucleic acid modification improves siRNA targeting*. Molecular Therapy-Nucleic Acids, 2013. **2**: p. e103.

85. Takei, Y., et al., *5'-, 3'-inverted thymidine-modified antisense oligodeoxynucleotide targeting midkine its design and application for cancer therapy*. Journal of Biological Chemistry, 2002. **277**(26): p. 23800-23806.

86. Raouane, M., et al., *Lipid conjugated oligonucleotides: a useful strategy for delivery*. Bioconjugate chemistry, 2012. **23**(6): p. 1091-1104.

87. Huang, Y., *Preclinical and clinical advances of GalNAc-decorated nucleic acid therapeutics*. Molecular Therapy-Nucleic Acids, 2017. **6**: p. 116-132.

88. Kulkarni, J.A., P.R. Cullis, and R. Van Der Meel, *Lipid nanoparticles enabling gene therapies: from concepts to clinical utility*. Nucleic acid therapeutics, 2018. **28**(3): p. 146-157.

89. Akinc, A., et al., *Targeted delivery of RNAi therapeutics with endogenous and exogenous ligand-based mechanisms*. Molecular Therapy, 2010. **18**(7): p. 1357-1364.

90. Alvarez-Erviti, L., et al., *Delivery of siRNA to the mouse brain by systemic injection of targeted exosomes*. Nature biotechnology, 2011. **29**(4): p. 341-345.

91. Kamerkar, S., et al., *Exosomes facilitate therapeutic targeting of oncogenic KRAS in pancreatic cancer*. Nature, 2017. **546**(7659): p. 498-503.

92. Ohno, S.-i., et al., *Systemically injected exosomes targeted to EGFR deliver antitumor microRNA to breast cancer cells*. Molecular Therapy, 2013. **21**(1): p. 185-191.

93. Cutler, J.I., E. Auyeung, and C.A. Mirkin, *Spherical nucleic acids*. Journal of the American Chemical Society, 2012. **134**(3): p. 1376-1391.

94. Yehl, K., et al., *Catalytic deoxyribozyme-modified nanoparticles for RNAi-independent gene regulation*. ACS nano, 2012. **6**(10): p. 9150-9157.

95. Yu, B., et al., *Targeted delivery systems for oligonucleotide therapeutics*. The AAPS journal, 2009. **11**(1): p. 195-203.

96. Nair, J.K., et al., *Multivalent N-acetylgalactosamine-conjugated siRNA localizes in hepatocytes and elicits robust RNAi-mediated gene silencing*. Journal of the American Chemical Society, 2014. **136**(49): p. 16958-16961.

97. Prakash, T.P., et al., *Targeted delivery of antisense oligonucleotides to hepatocytes using triantennary N-acetyl galactosamine improves potency 10-fold in mice*. Nucleic acids research, 2014. **42**(13): p. 8796-8807.

98. Sugo, T., et al., *Development of antibody-siRNA conjugate targeted to cardiac and skeletal muscles*. Journal of Controlled Release, 2016. **237**: p. 1-13.

99. Zhang, K., et al., *Antibody-linked spherical nucleic acids for cellular targeting*. Journal of the American Chemical Society, 2012. **134**(40): p. 16488-16491.

100. Kheirolomoom, A., et al., *Multifunctional nanoparticles facilitate molecular targeting and miRNA delivery to inhibit atherosclerosis in ApoE–/–mice*. ACS nano, 2015. **9**(9): p. 8885-8897.

101. Catuogno, S., et al., *Nucleic acids delivering nucleic acids*. Advanced drug delivery reviews, 2018. **134**: p. 79-93.

102. Yan, A.C. and M. Levy, *Aptamer-mediated delivery and cell-targeting aptamers: room for improvement*. nucleic acid therapeutics, 2018. **28**(3): p. 194-199.

103. McNamara, J.O., et al., *Cell type–specific delivery of siRNAs with aptamer-siRNA chimeras*. Nature biotechnology, 2006. **24**(8): p. 1005-1015.

104. Rajagopalan, A., et al., *Aptamer-targeted attenuation of IL-2 signaling in CD8+ T cells enhances antitumor immunity*. Molecular Therapy, 2017. **25**(1): p. 54-61.

105. Wang, Y., et al., *Nucleolin-targeted extracellular vesicles as a versatile platform for biologics delivery to breast cancer*. Theranostics, 2017. **7**(5): p. 1360.

106. Levin, A.A., *Targeting therapeutic oligonucleotides*. New England Journal of Medicine, 2017. **376**(1): p. 86-88.

107. Cheng, Q., et al., *Selective organ targeting (SORT) nanoparticles for tissue-specific mRNA delivery and CRISPR–Cas gene editing*. Nature Nanotechnology, 2020. **15**(4): p. 313-320.

108. Dahlman, J.E., et al., *Barcoded nanoparticles for high throughput in vivo discovery of targeted therapeutics*. Proceedings of the National Academy of Sciences, 2017. **114**(8): p. 2060-2065.

109. Sago, C.D., et al., *High-throughput in vivo screen of functional mRNA delivery identifies nanoparticles for endothelial cell gene editing*. Proceedings of the National Academy of Sciences, 2018. **115**(42): p. E9944-E9952.

110. Lokugamage, M.P., C.D. Sago, and J.E. Dahlman, *Testing thousands of nanoparticles in vivo using DNA barcodes*. Current opinion in biomedical engineering, 2018. **7**: p. 1-8.

111. Khan, O.F., et al., *Endothelial siRNA delivery in nonhuman primates using ionizable low–molecular weight polymeric nanoparticles*. Science advances, 2018. **4**(6): p. eaar8409.

112. Lokugamage, M.P., et al., *Constrained nanoparticles deliver siRNA and sgRNA to T cells in vivo without targeting ligands*. Advanced Materials, 2019. **31**(41): p. 1902251.

113. Gan, Z., et al., *Nanoparticles containing constrained phospholipids deliver mRNA to liver immune cells in vivo without targeting ligands*. Bioengineering & Translational Medicine, 2020: p. e10161.

114. Frens, G., *Controlled nucleation for the regulation of the particle size in monodisperse gold suspensions*. Nature physical science, 1973. **241**(105): p. 20-22.

115. Enustun, B. and J. Turkevich, *Coagulation of colloidal gold*. Journal of the American chemical society, 1963. **85**(21): p. 3317-3328.

116. Perrault, S.D. and W.C. Chan, *Synthesis and surface modification of highly monodispersed, spherical gold nanoparticles of 50– 200 nm*. Journal of the American Chemical Society, 2009. **131**(47): p. 17042-17043.

117. Hill, H.D. and C.A. Mirkin, *The bio-barcode assay for the detection of protein and nucleic acid targets using DTT-induced ligand exchange*. Nature protocols, 2006. **1**(1): p. 324.

118. Halo, T.L., et al., *NanoFlares for the detection, isolation, and culture of live tumor cells from human blood*. Proceedings of the National Academy of Sciences, 2014. **111**(48): p. 17104-17109.

119. Liu, B. and J. Liu, *Freezing directed construction of bio/nano interfaces: reagentless conjugation, denser spherical nucleic acids, and better nanoflares*. Journal of the American Chemical Society, 2017. **139**(28): p. 9471-9474.

120. Liu, B. and J. Liu, *Freezing-driven DNA adsorption on gold nanoparticles: tolerating extremely low salt concentration but requiring high DNA concentration*. Langmuir, 2019. **35**(19): p. 6476-6482.

121. Zhang, X., M.R. Servos, and J. Liu, *Instantaneous and quantitative functionalization of gold nanoparticles with thiolated DNA using a pH-assisted and*

surfactant-free route. Journal of the American Chemical Society, 2012. **134**(17): p. 7266-7269.

122. Hu, M., et al., *Single-step, salt aging-free and thiol-free freezing construction of AuNP-based bioprobes for advancing CRISPR-based diagnostics*. Journal of the American Chemical Society, 2020.

123. Rosi, N.L., et al., *Oligonucleotide-modified gold nanoparticles for intracellular gene regulation*. Science, 2006. **312**(5776): p. 1027-1030.

124. Giljohann, D.A., et al., *Gene regulation with polyvalent siRNA– nanoparticle conjugates*. Journal of the American Chemical Society, 2009. **131**(6): p. 2072-2073.

125. Jensen, S.A., et al., *Spherical nucleic acid nanoparticle conjugates as an RNAi-based therapy for glioblastoma*. Science translational medicine, 2013. **5**(209): p. 209ra152-209ra152.

126. Randeria, P.S., et al., *siRNA-based spherical nucleic acids reverse impaired wound healing in diabetic mice by ganglioside GM3 synthase knockdown*. Proceedings of the National Academy of Sciences, 2015. **112**(18): p. 5573-5578.

127. Somasuntharam, I., et al., *Knockdown of TNF-α by DNAzyme gold nanoparticles as an anti-inflammatory therapy for myocardial infarction*. Biomaterials, 2016. **83**: p. 12-22.

128. Giljohann, D.A., et al., *Oligonucleotide loading determines cellular uptake of DNA-modified gold nanoparticles*. Nano letters, 2007. **7**(12): p. 3818-3821.

129. Choi, C.H.J., et al., *Mechanism for the endocytosis of spherical nucleic acid nanoparticle conjugates*. Proceedings of the National Academy of Sciences, 2013. **110**(19): p. 7625-7630.

130. Patel, P.C., et al., *Scavenger receptors mediate cellular uptake of polyvalent oligonucleotide-functionalized gold nanoparticles*. Bioconjugate chemistry, 2010. **21**(12): p. 2250-2256.

131. Narayan, S.P., et al., *The Sequence-Specific Cellular Uptake of Spherical Nucleic Acid Nanoparticle Conjugates*. Small, 2015. **11**(33): p. 4173-4182.

132. Wu, X.A., et al., *Intracellular fate of spherical nucleic acid nanoparticle conjugates*. Journal of the American Chemical Society, 2014. **136**(21): p. 7726-7733.

133. Yamankurt, G., et al., *The effector mechanism of siRNA spherical nucleic acids*. Proceedings of the National Academy of Sciences, 2020.

134. Linko, V., A. Ora, and M.A. Kostiainen, *DNA nanostructures as smart drug-delivery vehicles and molecular devices*. Trends in biotechnology, 2015. **33**(10): p. 586-594.

135. Gudipati, S., K. Zhang, and J.L. Rouge, *Towards self-transfecting nucleic acid nanostructures for gene regulation*. Trends in biotechnology, 2019.

136. Ashmore-Harris, C. and G.O. Fruhwirth, *The clinical potential of gene editing as a tool to engineer cell-based therapeutics*. Clinical and Translational Medicine, 2020. **9**(1): p. 15.

137. Zhang, X., V. Goel, and G.J. Robbie, *Pharmacokinetics of Patisiran, the First Approved RNA Interference Therapy in Patients With Hereditary Transthyretin-Mediated Amyloidosis*. The Journal of Clinical Pharmacology, 2019.

138. Springer, A.D. and S.F. Dowdy, *GalNAc-siRNA conjugates: leading the way for delivery of RNAi therapeutics*. nucleic acid therapeutics, 2018. **28**(3): p. 109-118.

139. Young, D.D., et al., *Gene silencing in mammalian cells with light-activated antisense agents*. ChemBioChem, 2008. **9**(18): p. 2937-2940.

140. Young, D.D., M.O. Lively, and A. Deiters, *Activation and deactivation of DNAzyme and antisense function with light for the photochemical regulation of gene expression in mammalian cells*. Journal of the American Chemical Society, 2010. **132**(17): p. 6183-6193.

141. Yang, L., et al., *Efficient Synthesis of Light-Triggered Circular Antisense Oligonucleotides Targeting Cellular Protein Expression*. ChemBioChem, 2018. **19**(12): p. 1250-1254.

142. Zheng, G., et al., *Temporal and spatial regulation of microRNA activity with photoactivatable cantimirs*. ACS chemical biology, 2011. **6**(12): p. 1332-1338.

143. Richards, J.L., et al., *Turning the 10–23 DNAzyme on and off with light*. ChemBioChem, 2010. **11**(3): p. 320-324.

144. Govan, J.M., M.O. Lively, and A. Deiters, *Photochemical control of DNA decoy function enables precise regulation of nuclear factor κB activity*. Journal of the American Chemical Society, 2011. **133**(33): p. 13176-13182.

145. Weyel, X.M., M.A. Fichte, and A. Heckel, *A two-photon-photocleavable linker for triggering light-induced strand breaks in oligonucleotides*. ACS chemical biology, 2017. **12**(8): p. 2183-2190.

146. Govan, J.M., et al., *Regulation of transcription through light-activation and light-deactivation of triplex-forming oligonucleotides in mammalian cells*. ACS chemical biology, 2012. **7**(7): p. 1247-1256.

147. Moroz-Omori, E.V., et al., *Photoswitchable gRNAs for Spatiotemporally Controlled CRISPR-Cas-Based Genomic Regulation*. ACS Central Science, 2020.

148. Jain, P.K., et al., *Development of Light-Activated CRISPR Using Guide RNAs with Photocleavable Protectors*. Angewandte Chemie International Edition, 2016. **55**(40): p. 12440-12444.

149. Struntz, N.B. and D.A. Harki, *Catch and release DNA decoys: capture and photochemical dissociation of NF-κB transcription factors*. ACS chemical biology, 2016. **11**(6): p. 1631-1638.

150. Hammill, M.L., C. Isaacs-Trépanier, and J.P. Desaulniers, *siRNAzos: A New Class of Azobenzene-Containing siRNAs that Can Photochemically Regulate Gene Expression*. ChemistrySelect, 2017. **2**(30): p. 9810-9814.

151. Wu, L., Y. He, and X. Tang, *Photoregulating RNA digestion using azobenzene linked dumbbell antisense oligodeoxynucleotides*. Bioconjugate chemistry, 2015. **26**(6): p. 1070-1079.

152. Kamiya, Y., et al., *Development of Visible-Light-Responsive RNA Scissors Based on a 10–23 DNAzyme*. ChemBioChem, 2018. **19**(12): p. 1305-1311.

153. Kohman, R.E., et al., *Light-triggered release of bioactive molecules from DNA nanostructures*. Nano letters, 2016. **16**(4): p. 2781-2785.

154. Kohman, R.E. and X. Han, *Light sensitization of DNA nanostructures via incorporation of photo-cleavable spacers*. Chemical Communications, 2015. **51**(26): p. 5747-5750.

155. Green, A.A., et al., *Toehold switches: de-novo-designed regulators of gene expression*. Cell, 2014. **159**(4): p. 925-939.

156. Dhamodharan, V., et al., *Optochemical control of gene expression by photocaged guanine and riboswitches*. Chemical communications, 2018. **54**(48): p. 6181-6183.

157. Wulffen, B., et al., *Caged glucosamine-6-phosphate for the light-control of riboswitch activity*. Photochemical & Photobiological Sciences, 2012. **11**(3): p. 489-492.

158. Rotstan, K.A., et al., *Regulation of mRNA translation by a photoriboswitch*. Elife, 2020. **9**: p. e51737.

159. Kim, N.Y., et al., *Optogenetic control of mRNA localization and translation in live cells*. Nature Cell Biology, 2020. **22**(3): p. 341-352.

160. Peterson, J.A., et al., *Family of BODIPY photocages cleaved by single photons of visible/near-infrared light*. Journal of the American Chemical Society, 2018. **140**(23): p. 7343-7346.

161. Nani, R.R., et al., *Near-IR light-mediated cleavage of antibody–drug conjugates using cyanine photocages*. Angewandte Chemie International Edition, 2015. **54**(46): p. 13635-13638.

162. Gorka, A.P., et al., *A near-IR uncaging strategy based on cyanine photochemistry*. Journal of the American Chemical Society, 2014. **136**(40): p. 14153-14159.

163. Becker, Y., et al., *A red-shifted two-photon-only caging group for three-dimensional photorelease*. Chemical science, 2018. **9**(10): p. 2797-2802.

164. Wittmann, A. and B. Suess, *Engineered riboswitches: Expanding researchers' toolbox with synthetic RNA regulators*. FEBS letters, 2012. **586**(15): p. 2076-2083.

165. Nomura, Y., et al., *Controlling mammalian gene expression by allosteric hepatitis delta virus ribozymes*. ACS synthetic biology, 2013. **2**(12): p. 684-689.

166. Yen, L., et al., *Exogenous control of mammalian gene expression through modulation of RNA self-cleavage*. Nature, 2004. **431**(7007): p. 471-476.

167. Serganov, A. and E. Nudler, *A decade of riboswitches*. Cell, 2013. **152**(1-2): p. 17-24.

168. Suess, B. and J.E. Weigand, *Engineered riboswitches: overview, problems and trends*. RNA biology, 2008. **5**(1): p. 24-29.

169. Lee, C.H., S.R. Han, and S.-W. Lee, *Therapeutic applications of aptamer-based riboswitches*. nucleic acid therapeutics, 2016. **26**(1): p. 44-51.

170. Wilczynska, A. and M. Bushell, *The complexity of miRNA-mediated repression*. Cell Death & Differentiation, 2015. **22**(1): p. 22-33.

171. Mou, H., et al., *Conditional regulation of gene expression by ligand-induced occlusion of a microRNA target sequence*. Molecular Therapy, 2018. **26**(5): p. 1277-1286.

172. Liu, Y., et al., *Directing cellular information flow via CRISPR signal conductors*. Nature methods, 2016. **13**(11): p. 938.

173. Tang, W., J.H. Hu, and D.R. Liu, *Aptazyme-embedded guide RNAs enable ligand-responsive genome editing and transcriptional activation*. Nature communications, 2017. **8**(1): p. 1-8.

174. Chen, H., et al., *Aptazyme-mediated direct modulation of post-transcriptional sgRNA level for conditional genome editing and gene expression*. Journal of biotechnology, 2018. **288**: p. 23-29.

175. An, C.-I., V.B. Trinh, and Y. Yokobayashi, *Artificial control of gene expression in mammalian cells by modulating RNA interference through aptamer–small molecule interaction*. Rna, 2006. **12**(5): p. 710-716.

176. Beisel, C.L., et al., *Design of small molecule-responsive microRNAs based on structural requirements for Drosha processing*. Nucleic acids research, 2011. **39**(7): p. 2981-2994.

177. Kumar, D., C.-I. An, and Y. Yokobayashi, *Conditional RNA interference mediated by allosteric ribozyme*. Journal of the American Chemical Society, 2009. **131**(39): p. 13906-13907.

178. Lee, C.H., et al., *Hepatitis C virus replication-specific inhibition of microRNA activity with self-cleavable allosteric ribozyme*. Nucleic acid therapeutics, 2012. **22**(1): p. 17-29.

179. Banerjee, A., et al., *Controlled release of encapsulated cargo from a DNA icosahedron using a chemical trigger*. Angewandte Chemie International Edition, 2013. **52**(27): p. 6854-6857.

180. Zlatev, I., et al., *Reversal of siRNA-mediated gene silencing in vivo*. Nature biotechnology, 2018. **36**(6): p. 509-511.

181. Zhang, D.Y. and G. Seelig, *Dynamic DNA nanotechnology using strand-displacement reactions*. Nature chemistry, 2011. **3**(2): p. 103.

182. Mutalik, V.K., et al., *Rationally designed families of orthogonal RNA regulators of translation*. Nature chemical biology, 2012. **8**(5): p. 447.

183. Takahashi, M.K. and J.B. Lucks, *A modular strategy for engineering orthogonal chimeric RNA transcription regulators*. Nucleic acids research, 2013. **41**(15): p. 7577-7588.

184. Callura, J.M., C.R. Cantor, and J.J. Collins, *Genetic switchboard for synthetic biology applications*. Proceedings of the National Academy of Sciences, 2012. **109**(15): p. 5850-5855.

185. Lucks, J.B., et al., *Versatile RNA-sensing transcriptional regulators for engineering genetic networks*. Proceedings of the National Academy of Sciences, 2011. **108**(21): p. 8617-8622.

186. Isaacs, F.J., et al., *Engineered riboregulators enable post-transcriptional control of gene expression*. Nature biotechnology, 2004. **22**(7): p. 841-847.

187. Wang, S., N.J. Emery, and A.P. Liu, *A Novel Synthetic Toehold Switch for MicroRNA Detection in Mammalian Cells*. ACS synthetic biology, 2019. **8**(5): p. 1079-1088.

188. Kim, S.-J., et al., *Modulating responses of toehold switches by an inhibitory hairpin*. ACS synthetic biology, 2019. **8**(3): p. 601-605.

189. Kim, J., et al., *De novo-designed translation-repressing riboregulators for multi-input cellular logic*. Nature chemical biology, 2019. **15**(12): p. 1173-1182.

190. Lee, Y.J., et al., *Programmable control of bacterial gene expression with the combined CRISPR and antisense RNA system*. Nucleic acids research, 2016. **44**(5): p. 2462-2473.

191. Siu, K.-H. and W. Chen, *Riboregulated toehold-gated gRNA for programmable CRISPR–Cas9 function*. Nature chemical biology, 2019. **15**(3): p. 217-220.

192. Li, Y., et al., *RNA strand displacement responsive CRISPR/Cas9 system for mRNA sensing*. Analytical chemistry, 2019. **91**(6): p. 3989-3996.

193. Oesinghaus, L. and F.C. Simmel, *Switching the activity of Cas12a using guide RNA strand displacement circuits*. Nature communications, 2019. **10**(1): p. 1-11.

194. Hanewich-Hollatz, M.H., et al., *Conditional guide RNAs: programmable conditional regulation of CRISPR/Cas function in bacterial and mammalian cells via dynamic RNA nanotechnology*. ACS central science, 2019. **5**(7): p. 1241-1249.

195. Afonin, K.A., et al., *Activation of different split functionalities on re-association of RNA–DNA hybrids*. Nature nanotechnology, 2013. **8**(4): p. 296.

196. Xie, Z., et al., *Logic integration of mRNA signals by an RNAi-based molecular computer*. Nucleic acids research, 2010. **38**(8): p. 2692-2701.

197. Groves, B., et al., *Computing in mammalian cells with nucleic acid strand exchange*. Nature nanotechnology, 2016. **11**(3): p. 287.

198. Ren, K., et al., *In Situ SiRNA Assembly in Living Cells for Gene Therapy with MicroRNA Triggered Cascade Reactions Templated by Nucleic Acids*. ACS nano, 2018. **12**(11): p. 10797-10806.

199. Kahan-Hanum, M., et al., *A library of programmable DNAzymes that operate in a cellular environment*. Scientific reports, 2013. **3**(1): p. 1-6.

200. Nguyen, T.J., et al., *Toehold-Mediated Strand Displacement in a Triplex Forming Nucleic Acid Clamp for Reversible Regulation of Polymerase Activity and Protein Expression*. Chemistry–A European Journal, 2019. **25**(53): p. 12303-12307.

201. Torelli, E., et al., *A DNA origami nanorobot controlled by nucleic acid hybridization*. Small, 2014. **10**(14): p. 2918-2926.

202. Andersen, E.S., et al., *Self-assembly of a nanoscale DNA box with a controllable lid*. Nature, 2009. **459**(7243): p. 73-76.

203. Bujold, K.E., J.C. Hsu, and H.F. Sleiman, *Optimized DNA "nanosuitcases" for encapsulation and conditional release of siRNA*. Journal of the American Chemical Society, 2016. **138**(42): p. 14030-14038.

204. Grossi, G., et al., *Control of enzyme reactions by a reconfigurable DNA nanovault*. Nature communications, 2017. **8**(1): p. 1-8.

205. Jain, R., et al., *MicroRNAs enable mRNA therapeutics to selectively program cancer cells to self-destruct*. Nucleic acid therapeutics, 2018. **28**(5): p. 285-296.

206. Lee, J., et al., *Tissue-restricted genome editing in vivo specified by microRNA-repressible anti-CRISPR proteins*. RNA, 2019. **25**(11): p. 1421-1431.

207. Wang, X.-W., et al., *A microRNA-inducible CRISPR–Cas9 platform serves as a microRNA sensor and cell-type-specific genome regulation tool*. Nature cell biology, 2019. **21**(4): p. 522-530.

208. Ferry, Q.R., R. Lyutova, and T.A. Fulga, *Rational design of inducible CRISPR guide RNAs for de novo assembly of transcriptional programs*. Nature communications, 2017. **8**(1): p. 1-10.

209. Hochrein, L.M., et al., *Conditional Dicer substrate formation via shape and sequence transduction with small conditional RNAs*. Journal of the American Chemical Society, 2013. **135**(46): p. 17322-17330.

210. Masu, H., et al., *An activatable siRNA probe: trigger-RNA-dependent activation of RNAi function*. Angewandte Chemie International Edition, 2009. **48**(50): p. 9481-9483.

211. Kumar, D., S.H. Kim, and Y. Yokobayashi, *Combinatorially inducible RNA interference triggered by chemically modified oligonucleotides*. Journal of the American Chemical Society, 2011. **133**(8): p. 2783-2788.

212. Douglas, S.M., I. Bachelet, and G.M. Church, *A logic-gated nanorobot for targeted transport of molecular payloads*. Science, 2012. **335**(6070): p. 831-834.

213. Li, S., et al., *A DNA nanorobot functions as a cancer therapeutic in response to a molecular trigger in vivo*. Nature biotechnology, 2018. **36**(3): p. 258.

214. Sefah, K., et al., *Development of DNA aptamers using Cell-SELEX*. Nature protocols, 2010. **5**(6): p. 1169.

215. Nutiu, R. and Y. Li, *In vitro selection of structure-switching signaling aptamers*. Angewandte Chemie International Edition, 2005. **44**(7): p. 1061-1065.

216. Ranallo, S., et al., *Antibody-powered nucleic acid release using a DNA-based nanomachine*. Nature communications, 2017. **8**(1): p. 1-9.

217. Zadeh, J.N., et al., *NUPACK: analysis and design of nucleic acid systems*. Journal of computational chemistry, 2011. **32**(1): p. 170-173.

218. To, A.C.-Y., et al., *A comprehensive web tool for toehold switch design*. Bioinformatics, 2018. **34**(16): p. 2862-2864.

219. Wang, S.-R., et al., *Conditional control of RNA-guided nucleic acid cleavage and gene editing*. Nature Communications, 2020. **11**(1): p. 1-10.

220. Ma, V.P.Y. and K. Salaita, *DNA nanotechnology as an emerging tool to study mechanotransduction in living systems*. Small, 2019. **15**(26): p. 1900961.

221. Ruby, J.G., C.H. Jan, and D.P. Bartel, *Intronic microRNA precursors that bypass Drosha processing*. Nature, 2007. **448**(7149): p. 83-86.

222. Chong, M.M., et al., *Canonical and alternate functions of the microRNA biogenesis machinery*. Genes & development, 2010. **24**(17): p. 1951-1960.

223. Cifuentes, D., et al., *A novel miRNA processing pathway independent of Dicer requires Argonaute2 catalytic activity*. Science, 2010. **328**(5986): p. 1694-1698.

224. Yang, J.-S., et al., *Conserved vertebrate mir-451 provides a platform for Dicer-independent, Ago2-mediated microRNA biogenesis*. Proceedings of the National Academy of Sciences, 2010. **107**(34): p. 15163-15168.

225. O'Brien, J., et al., *Overview of microRNA biogenesis, mechanisms of actions, and circulation*. Frontiers in endocrinology, 2018. **9**: p. 402.

226. Lagos-Quintana, M., et al., *Identification of tissue-specific microRNAs from mouse*. Current biology, 2002. **12**(9): p. 735-739.

227. Chen, C.-Z., et al., *MicroRNAs modulate hematopoietic lineage differentiation*. science, 2004. **303**(5654): p. 83-86.

228. Ramkissoon, S.H., et al., *Hematopoietic-specific microRNA expression in human cells*. Leukemia research, 2006. **30**(5): p. 643-647.

229. Kloosterman, W.P., et al., *In situ detection of miRNAs in animal embryos using LNA-modified oligonucleotide probes*. Nature methods, 2006. **3**(1): p. 27-29.

230. Wienholds, E., et al., *MicroRNA expression in zebrafish embryonic development*. Science, 2005. **309**(5732): p. 310-311.

231. Nelson, P.T., et al., *RAKE and LNA-ISH reveal microRNA expression and localization in archival human brain*. Rna, 2006. **12**(2): p. 187-191.

232. Landgraf, P., et al., *A mammalian microRNA expression atlas based on small RNA library sequencing*. Cell, 2007. **129**(7): p. 1401-1414.

233. Sood, P., et al., *Cell-type-specific signatures of microRNAs on target mRNA expression*. Proceedings of the National Academy of Sciences, 2006. **103**(8): p. 2746-2751.

234. Jopling, C., *Liver-specific microRNA-122: Biogenesis and function*. RNA biology, 2012. **9**(2): p. 137-142.

235. Chang, J., et al., *miR-122, a mammalian liver-specific microRNA, is processed from hcr mRNA and maydownregulate the high affinity cationic amino acid transporter CAT-1*. RNA biology, 2004. **1**(2): p. 106-113.

236. Esau, C., et al., *miR-122 regulation of lipid metabolism revealed by in vivo antisense targeting*. Cell metabolism, 2006. **3**(2): p. 87-98.

237. Castoldi, M., et al., *The liver-specific microRNA miR-122 controls systemic iron homeostasis in mice*. The Journal of clinical investigation, 2011. **121**(4): p. 1386-1396.

238. Tsai, W.C., et al., *MicroRNA-122, a tumor suppressor microRNA that regulates intrahepatic metastasis of hepatocellular carcinoma*. Hepatology, 2009. **49**(5): p. 1571-1582.

239. Kutay, H., et al., *Downregulation of miR-122 in the rodent and human hepatocellular carcinomas*. Journal of cellular biochemistry, 2006. **99**(3): p. 671-678.

240. Coulouarn, C., et al., *Loss of miR-122 expression in liver cancer correlates with suppression of the hepatic phenotype and gain of metastatic properties*. Oncogene, 2009. **28**(40): p. 3526-3536.

241. Jopling, C.L., et al., *Modulation of hepatitis C virus RNA abundance by a liver-specific MicroRNA*. science, 2005. **309**(5740): p. 1577-1581.

242. Jopling, C.L., S. Schütz, and P. Sarnow, *Position-dependent function for a tandem microRNA miR-122-binding site located in the hepatitis C virus RNA genome*. Cell host & microbe, 2008. **4**(1): p. 77-85.

243. Iorio, M.V. and C.M. Croce, *MicroRNA dysregulation in cancer: diagnostics, monitoring and therapeutics. A comprehensive review*. EMBO molecular medicine, 2012. **4**(3): p. 143-159.

244. Cimmino, A., et al., *miR-15 and miR-16 induce apoptosis by targeting BCL2*. Proceedings of the National Academy of Sciences, 2005. **102**(39): p. 13944-13949.

245. Johnson, S.M., et al., *RAS is regulated by the let-7 microRNA family*. Cell, 2005. **120**(5): p. 635-647.

246. Mott, J.L., et al., *mir-29 regulates Mcl-1 protein expression and apoptosis*. Oncogene, 2007. **26**(42): p. 6133-6140.

247. Sampson, V.B., et al., *MicroRNA let-7a down-regulates MYC and reverts MYC-induced growth in Burkitt lymphoma cells*. Cancer research, 2007. **67**(20): p. 9762-9770.

248. Meng, F., et al., *MicroRNA-21 regulates expression of the PTEN tumor suppressor gene in human hepatocellular cancer*. Gastroenterology, 2007. **133**(2): p. 647-658.

249. Frankel, L.B., et al., *Programmed cell death 4 (PDCD4) is an important functional target of the microRNA miR-21 in breast cancer cells*. Journal of Biological Chemistry, 2008. **283**(2): p. 1026-1033.

250. Wojciechowska, A., A. Braniewska, and K. Kozar-Kamińska, *MicroRNA in cardiovascular biology and disease*. Advances in clinical and experimental medicine: official organ Wroclaw Medical University, 2017. **26**(5): p. 865-874.

251. Kumar, S., et al., *Role of flow-sensitive microRNAs and long noncoding RNAs in vascular dysfunction and atherosclerosis*. Vascular pharmacology, 2019. **114**: p. 76-92.

252. Son, D.J., et al., *The atypical mechanosensitive microRNA-712 derived from pre-ribosomal RNA induces endothelial inflammation and atherosclerosis*. Nature communications, 2013. **4**: p. 3000.

253. Kim, C.W., et al., *Prevention of abdominal aortic aneurysm by Anti–MicroRNA-712 or Anti–MicroRNA-205 in angiotensin II–infused mice*. Arteriosclerosis, thrombosis, and vascular biology, 2014. **34**(7): p. 1412-1421.

254. Rayner, K.J., et al., *MiR-33 contributes to the regulation of cholesterol homeostasis*. science, 2010. **328**(5985): p. 1570-1573.

255. Rayner, K.J., et al., *Antagonism of miR-33 in mice promotes reverse cholesterol transport and regression of atherosclerosis*. The Journal of clinical investigation, 2011. **121**(7): p. 2921-2931.

256. Ouimet, M., et al., *MicroRNA-33–dependent regulation of macrophage metabolism directs immune cell polarization in atherosclerosis*. The Journal of clinical investigation, 2015. **125**(12): p. 4334-4348.

257. Lai, L., et al., *MicroRNA-33 regulates the innate immune response via ATP binding cassette transporter-mediated remodeling of membrane microdomains*. Journal of Biological Chemistry, 2016. **291**(37): p. 19651-19660.

258. Palladino, M.A., et al., *Anti-TNF-α therapies: the next generation*. Nature reviews Drug discovery, 2003. **2**(9): p. 736-746.

259. Monaco, C., et al., *Anti-TNF therapy: past, present and future*. International immunology, 2015. **27**(1): p. 55-62.

260. Feldmann, M. and R.N. Maini, *TNF defined as a therapeutic target for rheumatoid arthritis and other autoimmune diseases*. Nature medicine, 2003. **9**(10): p. 1245-1250.

261. van Heel, D.A., et al., *Inflammatory bowel disease is associated with a TNF polymorphism that affects an interaction between the OCT1 and NF-κB transcription factors*. Human molecular genetics, 2002. **11**(11): p. 1281-1289.

262. Levine, B., et al., *Elevated circulating levels of tumor necrosis factor in severe chronic heart failure*. New England Journal of Medicine, 1990. **323**(4): p. 236-241.

263. Sewell, K.L., et al., *Phase I trial of ISIS 104838, a 2'-methoxyethyl modified antisense oligonucleotide targeting tumor necrosis factor-α*. Journal of Pharmacology and Experimental Therapeutics, 2002. **303**(3): p. 1334-1343.

264. Iversen, P.O., G. Nicolaysen, and M. Sioud, *DNA enzyme targeting TNF-α mRNA improves hemodynamic performance in rats with postinfarction heart failure*. American Journal of Physiology-Heart and Circulatory Physiology, 2001. **281**(5): p. H2211-H2217.

265. Wang, G.L., et al., *Hypoxia-inducible factor 1 is a basic-helix-loop-helix-PAS heterodimer regulated by cellular O2 tension*. Proceedings of the national academy of sciences, 1995. **92**(12): p. 5510-5514.

266. Wang, V., et al., *Differential gene up-regulation by hypoxia-inducible factor-1α and hypoxia-inducible factor-2α in HEK293T cells*. Cancer research, 2005. **65**(8): p. 3299-3306.

267. Makino, Y., et al., *Inhibitory PAS domain protein (IPAS) is a hypoxia-inducible splicing variant of the hypoxia-inducible factor-3α locus*. Journal of Biological Chemistry, 2002. **277**(36): p. 32405-32408.

268. Heikkilä, M., et al., *Roles of the human hypoxia-inducible factor (HIF)-3α variants in the hypoxia response*. Cellular and molecular life sciences, 2011. **68**(23): p. 3885-3901.

269. Demidenko, Z.N. and M.V. Blagosklonny, *The purpose of the HIF-1/PHD feedback loop: to limit mTOR-induced HIF-1α*. Cell cycle, 2011. **10**(10): p. 1557-1562.

270. Maxwell, P.H., et al., *The tumour suppressor protein VHL targets hypoxia-inducible factors for oxygen-dependent proteolysis*. Nature, 1999. **399**(6733): p. 271-275.

271. Mahon, P.C., K. Hirota, and G.L. Semenza, *FIH-1: a novel protein that interacts with HIF-1α and VHL to mediate repression of HIF-1 transcriptional activity*. Genes & development, 2001. **15**(20): p. 2675-2686.

272. Jiang, B.-H., et al., *Dimerization, DNA binding, and transactivation properties of hypoxia-inducible factor 1*. Journal of Biological Chemistry, 1996. **271**(30): p. 17771-17778.

273. He, Q., et al., *Regulation of HIF-1α activity in adipose tissue by obesity-associated factors: adipogenesis, insulin, and hypoxia*. American Journal of Physiology-Endocrinology and Metabolism, 2011. **300**(5): p. E877-E885.

274. Stasinopoulos, I., D.R. O'Brien, and Z.M. Bhujwalla, *Inflammation, but not hypoxia, mediated HIF-1α activation depends on COX-2*. Cancer biology & therapy, 2009. **8**(1): p. 31-35.

275. Liu, M., D. Wang, and N. Li, *MicroRNA-20b downregulates HIF-1α and Inhibits the proliferation and invasion of osteosarcoma cells*. Oncology Research Featuring Preclinical and Clinical Cancer Therapeutics, 2016. **23**(5): p. 257-266.

276. Feng, S., et al., *Mechanical activation of hypoxia-inducible factor 1α drives endothelial dysfunction at atheroprone sites*. Arteriosclerosis, thrombosis, and vascular biology, 2017. **37**(11): p. 2087-2101.

277. Fernandez Esmerats, J., et al., *Disturbed Flow Increases UBE2C (Ubiquitin E2 Ligase C) via Loss of miR-483-3p, Inducing Aortic Valve Calcification by the pVHL (von Hippel-Lindau Protein) and HIF-1α (Hypoxia-Inducible Factor-1α) Pathway in Endothelial Cells*. Arteriosclerosis, thrombosis, and vascular biology, 2019. **39**(3): p. 467-481.

278. Jun, J.C., et al., *Hypoxia-inducible factors and cancer*. Current sleep medicine reports, 2017. **3**(1): p. 1-10.

279. Masoud, G.N. and W. Li, *HIF-1α pathway: role, regulation and intervention for cancer therapy*. Acta Pharmaceutica Sinica B, 2015. **5**(5): p. 378-389.

280. Greenberger, L.M., et al., *A RNA antagonist of hypoxia-inducible factor-1α, EZN-2968, inhibits tumor cell growth*. Molecular cancer therapeutics, 2008. **7**(11): p. 3598-3608.

281. Jeong, W., et al., *Pilot trial of EZN-2968, an antisense oligonucleotide inhibitor of hypoxia-inducible factor-1 alpha (HIF-1α), in patients with refractory solid tumors*. Cancer chemotherapy and pharmacology, 2014. **73**(2): p. 343-348.

282. Debacker, A.J., et al., *Delivery of Oligonucleotides to the liver with GalNAc–from research to registered therapeutic drug*. Molecular Therapy, 2020.

283. Kulkarni, J.A., et al., *Lipid nanoparticle technology for clinical translation of siRNA therapeutics*. Accounts of chemical research, 2019. **52**(9): p. 2435-2444.

284. Corey, D.R., *Nusinersen, an antisense oligonucleotide drug for spinal muscular atrophy*. Nature neuroscience, 2017. **20**(4): p. 497-499.

285. Tabrizi, S., et al., *Effects of IONIS-HTTRx in patients with early Huntington's disease, results of the first HTT-lowering drug trial (CT. 002)*. 2018, AAN Enterprises.

286. Wang, Z., M. Gerstein, and M. Snyder, *RNA-Seq: a revolutionary tool for transcriptomics*. Nature reviews genetics, 2009. **10**(1): p. 57-63.

287. Saliba, A.-E., et al., *Single-cell RNA-seq: advances and future challenges*. Nucleic acids research, 2014. **42**(14): p. 8845-8860.

288. Casamassimi, A., et al., *Transcriptome profiling in human diseases: new advances and perspectives*. International journal of molecular sciences, 2017. **18**(8): p. 1652.

289. Padang, R., et al., *Comparative transcriptome profiling in human bicuspid aortic valve disease using RNA sequencing*. Physiological genomics, 2015. **47**(3): p. 75-87.

290. Zhu, J., et al., *Identification of tissue-specific protein-coding and noncoding transcripts across 14 human tissues using RNA-seq*. Scientific reports, 2016. **6**(1): p. 1-11.

291. Fagerberg, L., et al., *Analysis of the human tissue-specific expression by genome-wide integration of transcriptomics and antibody-based proteomics*. Molecular & Cellular Proteomics, 2014. **13**(2): p. 397-406.

292. Helgeland, H., et al., *Transcriptome profiling of human thymic CD4+ and CD8+ T cells compared to primary peripheral T cells*. BMC genomics, 2020. **21**: p. 1-15.

293. Bongartz, T., et al., *Anti-TNF antibody therapy in rheumatoid arthritis and the risk of serious infections and malignancies: systematic review and meta-analysis of rare harmful effects in randomized controlled trials*. Jama, 2006. **295**(19): p. 2275-2285.

294. Mariette, X., et al., *Malignancies associated with tumour necrosis factor inhibitors in registries and prospective observational studies: a systematic review and meta-analysis*. Annals of the rheumatic diseases, 2011. **70**(11): p. 1895-1904.

295. Gilkes, D.M., et al., *Hypoxia-inducible factor 1 (HIF-1) promotes extracellular matrix remodeling under hypoxic conditions by inducing P4HA1, P4HA2, and PLOD2 expression in fibroblasts*. Journal of Biological Chemistry, 2013. **288**(15): p. 10819-10829.

296. Darby, I.A. and T.D. Hewitson, *Hypoxia in tissue repair and fibrosis*. Cell and tissue research, 2016. **365**(3): p. 553-562.

297. Xiong, A. and Y. Liu, *Targeting hypoxia inducible factors-1α as a novel therapy in fibrosis*. Frontiers in Pharmacology, 2017. **8**: p. 326.

298. Zhang, D.Y. and G. Seelig, *Dynamic DNA nanotechnology using strand-displacement reactions*. Nature chemistry, 2011. **3**(2): p. 103-113.

299. Szulc, J., et al., *A versatile tool for conditional gene expression and knockdown*. Nature methods, 2006. **3**(2): p. 109-116.

300. Tiscornia, G., et al., *CRE recombinase-inducible RNA interference mediated by lentiviral vectors*. Proceedings of the National Academy of Sciences, 2004. **101**(19): p. 7347-7351.

301. Liu, Y., et al., *Directing cellular information flow via CRISPR signal conductors*. Nature methods, 2016. **13**(11): p. 938-994.

302. Jin, M., et al., *Programmable CRISPR-Cas Repression, Activation, and Computation with Sequence-Independent Targets and Triggers*. ACS synthetic biology, 2019. **8**(7): p. 1583-1589.

303. Hemphill, J., et al., *Conditional control of alternative splicing through light-triggered splice-switching oligonucleotides*. Journal of the American Chemical Society, 2015. **137**(10): p. 3656-3662.

304. Zheng, D., et al., *Topical delivery of siRNA-based spherical nucleic acid nanoparticle conjugates for gene regulation*. Proceedings of the National Academy of Sciences, 2012. **109**(30): p. 11975-11980.

305. Kumar, S., et al., *Role of flow-sensitive microRNAs in endothelial dysfunction and atherosclerosis: mechanosensitive athero-miRs*. Arteriosclerosis, thrombosis, and vascular biology, 2014. **34**(10): p. 2206-2216.

306. Kumar, S., et al., *Role of Noncoding RNAs in the Pathogenesis of Abdominal Aortic Aneurysm: Possible Therapeutic Targets?* Circulation research, 2019. **124**(4): p. 619-630.

307. Hartmann, A.K., et al., *Enzymatically Ligated DNA–Surfactants: Unmasking Hydrophobically Modified DNA for Intracellular Gene Regulation*. ChemBioChem, 2018. **19**(16): p. 1734-1739.

308. Ouimet, M., et al., *microRNA-33 regulates macrophage autophagy in atherosclerosis*. Arteriosclerosis, thrombosis, and vascular biology, 2017. **37**(6): p. 1058-1067.

309. Moore, K.J., F.J. Sheedy, and E.A. Fisher, *Macrophages in atherosclerosis: a dynamic balance*. Nature Reviews Immunology, 2013. **13**(10): p. 709-721.

310. Branen, L., et al., *Inhibition of tumor necrosis factor-α reduces atherosclerosis in apolipoprotein E knockout mice*. Arteriosclerosis, thrombosis, and vascular biology, 2004. **24**(11): p. 2137-2142.

311. Bartelds, G.M., et al., *Development of antidrug antibodies against adalimumab and association with disease activity and treatment failure during long-term follow-up*. Jama, 2011. **305**(14): p. 1460-1468.

312. Scheinfeld, N., *A comprehensive review and evaluation of the side effects of the tumor necrosis factor alpha blockers etanercept, infliximab and adalimumab*. Journal of dermatological treatment, 2004. **15**(5): p. 280-294.

313. Zhang, L., et al., *Promoting the delivery of nanoparticles to atherosclerotic plaques by DNA coating*. ACS applied materials & interfaces, 2018. **11**(15): p. 13888-13904.

314. Genot, A.J., et al., *Remote toehold: a mechanism for flexible control of DNA hybridization kinetics*. Journal of the American Chemical Society, 2011. **133**(7): p. 2177-2182.

315. Schubert, S., et al., *RNA cleaving '10-23'DNAzymes with enhanced stability and activity*. Nucleic acids research, 2003. **31**(20): p. 5982-5992.

316. Lin, A.Y., et al., *Gold nanoparticle delivery of modified CpG stimulates macrophages and inhibits tumor growth for enhanced immunotherapy*. PloS one, 2013. **8**(5): p. e63550.

317. Sester, D.P., et al., *CpG DNA activates survival in murine macrophages through TLR9 and the phosphatidylinositol 3-kinase-Akt pathway*. The Journal of Immunology, 2006. **177**(7): p. 4473-4480.

318. Hill, H.D. and C.A. Mirkin, *The bio-barcode assay for the detection of protein and nucleic acid targets using DTT-induced ligand exchange*. Nature protocols, 2006. **1**(1): p. 324-336.

319. Deng, R., et al., *Targeting epigenetic pathway with gold nanoparticles for acute myeloid leukemia therapy*. Biomaterials, 2018. **167**: p. 80-90.

320. Chinen, A.B., et al., *The impact of protein corona formation on the macrophage cellular uptake and biodistribution of spherical nucleic acids*. Small, 2017. **13**(16): p. 1603847.

321. Zhang, W., B. Meckes, and C.A. Mirkin, *Spherical Nucleic Acids with Tailored and Active Protein Coronae*. ACS central science, 2019. **5**(12): p. 1983-1990.

322. Fleischer, C.C. and C.K. Payne, *Nanoparticle–cell interactions: molecular structure of the protein corona and cellular outcomes*. Accounts of chemical research, 2014. **47**(8): p. 2651-2659.

323. Zhang, X., R. Goncalves, and D.M. Mosser, *The isolation and characterization of murine macrophages*. Current protocols in immunology, 2008. **83**(1): p. 14.1. 1-14.1. 14.

324. Liu, M., et al., *Real-time visualization of clustering and intracellular transport of gold nanoparticles by correlative imaging*. Nature communications, 2017. **8**(1): p. 1-10.

325. Carnevale, K.J., R.A. Riskowski, and G.F. Strouse, *A gold nanoparticle bio-optical transponder to dynamically monitor intracellular pH*. ACS nano, 2018. **12**(6): p. 5956-5968.

326. Becker, W., et al., *Fluorescence lifetime imaging by time-correlated single-photon counting*. Microscopy research and technique, 2004. **63**(1): p. 58-66.

327. Borst, J.W. and A.J. Visser, *Fluorescence lifetime imaging microscopy in life sciences*. Measurement Science and Technology, 2010. **21**(10): p. 102002.

328. Becker, W., *Fluorescence lifetime imaging–techniques and applications*. Journal of microscopy, 2012. **247**(2): p. 119-136.

329. Li, F., et al., *Thermal stability of DNA functionalized gold nanoparticles*. Bioconjugate chemistry, 2013. **24**(11): p. 1790-1797.

330. Erazo-Oliveras, A., et al., *Improving the endosomal escape of cell-penetrating peptides and their cargos: strategies and challenges*. Pharmaceuticals, 2012. **5**(11): p. 1177-1209.

331. Smith, S.A., et al., *The endosomal escape of nanoparticles: Toward more efficient cellular delivery*. Bioconjugate chemistry, 2018. **30**(2): p. 263-272.

332. Walder, R.Y. and J.A. Walder, *Role of RNase H in hybrid-arrested translation by antisense oligonucleotides*. Proceedings of the National Academy of Sciences, 1988. **85**(14): p. 5011-5015.

333. Bennett, C.F., *Therapeutic antisense oligonucleotides are coming of age*. Annual review of medicine, 2019. **70**: p. 307-321.

334. Bennett, C.F., et al., *Pharmacology of antisense drugs*. Annual review of pharmacology and toxicology, 2017. **57**: p. 81-105.

335. Craig, K., M. Abrams, and M. Amiji, *Recent preclinical and clinical advances in oligonucleotide conjugates*. Expert opinion on drug delivery, 2018. **15**(6): p. 629-640.

336. Deiters, A., et al., *Photocaged morpholino oligomers for the light-regulation of gene function in zebrafish and Xenopus embryos*. Journal of the American Chemical Society, 2010. **132**(44): p. 15644-15650.

337. Miao, L., et al., *Delivery of mRNA vaccines with heterocyclic lipids increases anti-tumor efficacy by STING-mediated immune cell activation*. Nature biotechnology, 2019. **37**(10): p. 1174-1185.

338. Hanna, J., G.S. Hossain, and J. Kocerha, *The potential for microRNAs in clinical research*. Frontiers in genetics, 2019. **10**: p. 478.

339. Barkau, C.L., et al., *Rationally designed anti-CRISPR nucleic acid inhibitors of CRISPR-Cas9*. Nucleic acid therapeutics, 2019. **29**(3): p. 136-147.

340. Lewis, A.P. and C.L. Jopling, *Regulation and biological function of the liver-specific miR-122*. Biochemical Society Transactions, 2010. **38**(6): p. 1553-1557.

341. Bandiera, S., et al., *miR-122–a key factor and therapeutic target in liver disease*. Journal of hepatology, 2015. **62**(2): p. 448-457.

342. Semenza, G.L., *Targeting HIF-1 for cancer therapy*. Nature reviews cancer, 2003. **3**(10): p. 721-732.

343. Semenza, G.L., *HIF-1: upstream and downstream of cancer metabolism*. Current opinion in genetics & development, 2010. **20**(1): p. 51-56.

344. Semenza, G.L., *Hypoxia-inducible factor 1 and cardiovascular disease*. Annual review of physiology, 2014. **76**: p. 39-56.

345. Tan, C., et al., *Sulfonamides as a new scaffold for hypoxia inducible factor pathway inhibitors*. Bioorganic & medicinal chemistry letters, 2011. **21**(18): p. 5528-5532.

346. Chan, M.C., et al., *Potent and selective triazole-based inhibitors of the hypoxia-inducible factor prolyl-hydroxylases with activity in the murine brain*. PLoS One, 2015. **10**(7).

347. Zheng, Q., et al., *Tumor-Specific Transcripts Are Frequently Expressed in Hepatocellular Carcinoma With Clinical Implication and Potential Function*. Hepatology, 2020. **71**(1): p. 259-274.

348. Amatschek, S., et al., *Tissue-wide expression profiling using cDNA subtraction and microarrays to identify tumor-specific genes*. Cancer research, 2004. **64**(3): p. 844-856.

349. Chen, H., et al., *Long-read RNA sequencing identifies alternative splice variants in hepatocellular carcinoma and tumor-specific isoforms*. Hepatology, 2019. **70**(3): p. 1011-1025.

350. Shyh-Chang, N. and G.Q. Daley, *Lin28: primal regulator of growth and metabolism in stem cells*. Cell stem cell, 2013. **12**(4): p. 395-406.

351. Viswanathan, S.R., et al., *Lin28 promotes transformation and is associated with advanced human malignancies*. Nature genetics, 2009. **41**(7): p. 843.

352. Nguyen, L.H., et al., *Lin28b is sufficient to drive liver cancer and necessary for its maintenance in murine models*. Cancer cell, 2014. **26**(2): p. 248-261.

353. Guo, W., et al., *A LIN28B tumor-specific transcript in cancer*. Cell reports, 2018. **22**(8): p. 2016-2025.

354. Wiesner, T., et al., *Alternative transcription initiation leads to expression of a novel ALK isoform in cancer*. Nature, 2015. **526**(7573): p. 453-457.

355. Stefanis, L., *α-Synuclein in Parkinson's disease*. Cold Spring Harbor perspectives in medicine, 2012. **2**(2): p. a009399.

356. Alarcón-Arís, D., et al., *Selective α-synuclein knockdown in monoamine neurons by intranasal oligonucleotide delivery: potential therapy for Parkinson's disease*. Molecular Therapy, 2018. **26**(2): p. 550-567.

357. Alarcón-Arís, D., et al., *Antisense oligonucleotide reduction of human alpha-synuclein accumulation in dopamine and serotonin neurons prevents early dysfunctions in a mouse model of Parkinson's disease*. 2016.

358. Rhinn, H., et al., *Alternative α-synuclein transcript usage as a convergent mechanism in Parkinson's disease pathology*. Nature communications, 2012. **3**(1): p. 1-11.